Rendering Titanium Superhydrophobic

A thesis
submitted in partial fulfilment
of the requirements for the degree
of

Master of Science in Chemistry
at
The University of Waikato

by
Sam Rewi Pachal

The University of Waikato
2012

Abstract

Two methods are reported herein to render titanium metal superhydrophobic. A superhydrophobic surface by definition is one that shows a water contact angle of equal to or greater than 150˚,[1] while in contrast bare titanium metal is hydrophilic and exhibits a water contact angle of 73±3˚.[2] Titanium metal is extremely reactive in air and rapidly forms a self-repairing oxide layer, which makes the necessary surface modification of the material to render it superhydrophobic challenging.

The first method employed in this work consists of a cold compression procedure whereby copper powder that has been previously rendered superhydrophobic by galvanic deposition of silver followed by treatment with 1-dodecanethiol is compressed onto titanium powder. The resulting compact consists of a superhydrophobic copper layer on a titanium substrate. The superhydrophobic copper layer is robust in that if it is damaged, the damaged layer can be abraded away to expose a new, fresh superhydrophobic copper layer beneath. Each successive layer exposed after abrasion throughout the superhydrophobic copper portion of the material is shown to exhibit the same wetting characteristics with regards to water roll-off angle.

The superhydrophobic titanium material prepared by this method exhibited a static water contact angle of 157±1º and water roll-off angles of 3.8±0.9º. The method was also successfully applied to aluminium powder, which showed a water roll-off angle of 4.2±0.4˚.

An additional superhydrophobic titanium material was prepared using this method which had a polyfluoroalkylthiol surface modifier, 1H,1H,2H,2H-perfluorodecanethiol, used in place of the 1-dodecanethiol. This material showed no statistically significant difference in wetting behaviour from its alkylthiol treated counterpart, with a water roll-off angle of 3.4±0.5˚ and a static water contact angle of 159±3˚.

The second method employed in this work was applicable to a foil form of titanium. It involves the deposition of copper onto a titanium foil, followed by galvanic reduction of silver onto the copper plate and adsorption of 1H,1H,2H,2H-perfluorodecanethiol in a self-assembled monolayer. Difficulty was encountered in getting a reproducibly adherent copper plate onto the titanium foil, and two methods were experimented with to find optimum conditions for an adherent copper deposit.

The first strategy used to deposit copper onto titanium involved a high voltage capacitor discharge across a titanium electrode in an acidic copper sulfate solution to destroy the native oxide layer present on titanium. A copper electroplate immediately followed this step, though unfortunately none of the deposits prepared in this manner passed adherence tests. The second method involved an anodic etching step before deposition of copper and showed much improved adherence over the first method, but was inconsistent and the copper coatings were non-uniform.

The superhydrophobic titanium materials prepared on titanium foils using both methods of copper deposition showed the same roll-off angles for an applied glycerol droplet as a purely superhydrophobic copper foil. A previous publication[1] has quoted superhydrophobic copper foil prepared by the same method as having a water contact angle of 173±1˚ and a water roll-off angle of 0.64±0.04˚. Extrapolating from the materials sharing the same glycerol roll-off angles gives some confirmation that a superhydrophobic surface has successfully been applied to titanium foil in this work.

Acknowledgements

None of this work would have been able to have been done without the help of many talented and enthusiastic staff throughout the Faculty of Science and Engineering at the University of Waikato. First and foremost I must say it has been a pleasure to work under my project supervisor, Dr Graham Saunders. His patience and guidance throughout this project, as well as sharing his thoughts on the outcomes of the 2011 Rugby World Cup games and other sporting events have made the work most enjoyable indeed.

I would also like to thank Helen Turner for her tuition in using the SEM facility, Brett Nichol for help with using the Materials Tester, Professor Jonathon Scott for his help in procuring and assembling electrical equipment, Dr Michael Mucalo for assistance with recording infrared spectra and Dr Joseph Lane for his help with computational work. Special mention goes to the laboratory technicians Pat Gread and Wendy Jackson whom I can’t remember declining a request for a favour or laboratory equipment over the years. Dr Duncan McGillivray from The University of Auckland is also to be thanked for his acquiring of contact angle data. To thank everyone who was involved and helped in the project would have my thesis begin to resemble a phonebook, so to anybody that I have missed out I am truly sorry!

Acknowledgement and thanks must also go to the Ministry of Science and Innovation for their generous funding of the project through my Ti Tipu Putaiaio Fellowship and to Pania Melbourne for her mentoring throughout the process. I am also grateful to The University of Waikato for their Masters Research Scholarship and Maori Postgraduate Excellence Award.

Finally I would like to thank all of the friends I have made in the Chemistry Department over my time at The University of Waikato. You have all been great company, and I thoroughly appreciate you putting up with two years of pranks and general mindless banter from me. Wherever you find yourselves headed in the future I wish you all the very best, it has been an absolute pleasure and a time in my life I will look fondly on for years to come.

Table of Contents

List of Figures

List of Tables

List of Equations

List of Abbreviations

%: Percent

˚: Degree

˚C: Degree Celsius

€: Euro

µF: Microfarad

µm: Micrometre

ca: Circa

cm^{-1}: Wavenumber

CVD: Chemical vapour deposition

DC: Direct current

f_i: Fraction of water in contact with surface i

g: Gram

GA: Gas atomised

gcm^{-3}: Gram per cubic centimetre

HDFT: 1H,1H,2H,2H-perfluorodecanethiol

HDH: Hydrogenation-dehydrogenation

HV: High voltage

IR: Infrared

kV: Kilovolt

M: Molar

mA: Milliamp

mL: Millilitre

mm: Millimetre

mNm^{-1}: Millinewtons per metre

MPa: Megapascal

nm: Nanometre

PDMS: Poly(dimethylsiloxane)

PET: Poly(ethyleneterephthalate)

PTFE: Poly(tetrafluoroethylene)

SAM: Self-assembled monolayer

SEM: Scanning electron microscope

V: Volt

vs: Versus

WCA: Water contact angle

γ_{xy}: Surface tension between phases x and y

θ_a: Advancing contact angle

θ_{CB}: Cassie-Baxter contact angle

θ_r: Receding contact angle

θ_{ro}: Roll-off angle

θ_{Wenzel}: Wenzel contact angle

θ_{Young}: Young contact angle

ν: Stretching frequency

ν_a: Asymmetric stretching frequency

ν_s: Symmetric stretching frequency

1 Introduction

Superhydrophobic surfaces are notable for their extreme water repellency, and are defined as showing a water contact angle of greater than 150^{0}[1] (Figure 1). The past ten years have seen the field of preparation of these superhydrophobic surfaces enjoy remarkable growth.[3] The growth in research in this area is due to the many interesting and exciting potential applications including, but by no means limited to, self-cleaning textiles,[4] corrosion resistance of metal components, anti-fouling for marine vehicles[5] and drag reduction.[6]

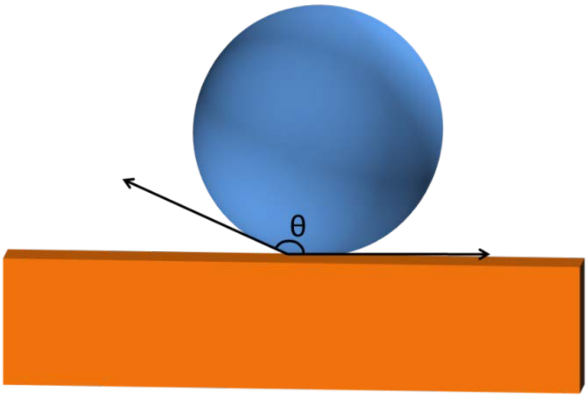

Figure 1: A superhydrophobic surface showing contact angle, θ, greater than 150^{0}

A water droplet will adhere to a solid surface if its surface interfacial free energy is reduced. When water is in contact with the surface, an angle is formed between the tangent to the liquid-vapour interface and the surface (Figure 2). The angle made on the liquid side of this is the water contact angle (WCA), and is a characteristic of a given solid-liquid-vapour system.[7] Water can spread onto the surface to give an angle of less than 90^{0} which defines the surface as hydrophilic,[8] or it will not spread and minimise its contact with the surface which gives a contact angle of greater than 90^{0} (Figure 2). This surface is defined as being hydrophobic.

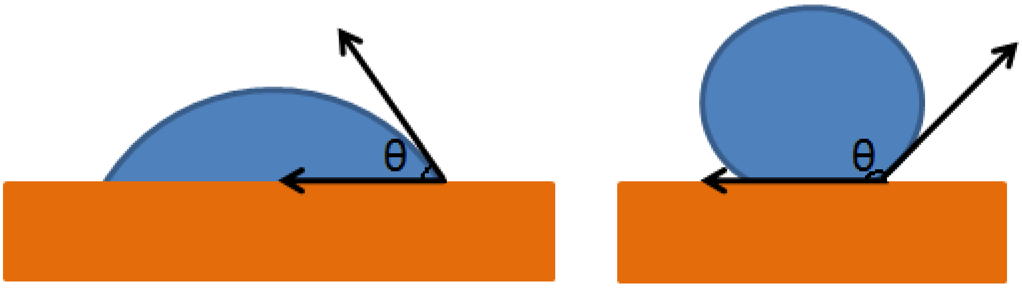

Figure 2: Surfaces showing hydrophilic (left) contact angle and hydrophobic (right) contact angle.

1.1 Examples in Nature

While the rapid growth in research in the area is relatively recent, Nature has been utilising superhydrophobic surfaces for some time. It seems Nature understands the principles of wetting well; many syntheses for superhydrophobic structures are inspired by Nature's designs with the Lotus leaf, *Nelumbo nucifera*,[1,9] being the most prominent example. In fact, the Lotus leaf is so commonly associated with superhydrophobicity that the property is commonly referred to as the "Lotus Effect".[9]

Neinhuis and Barthlott's 1996 publication[9] examined the morphology and wettability of the Lotus leaf amongst a selection of over 300 other leaves. The study found that the Lotus leaf exhibits a hierarchical dual-scale roughness on its surface. The base layer roughness consists of papillose epidermal cells, each of which is approximately ten micrometres in width. Superimposed on top of these micrometre scale structures is a waxy coating in the form of epicuticular wax crystalloids which are of the nanometre size domain (Figure 3).

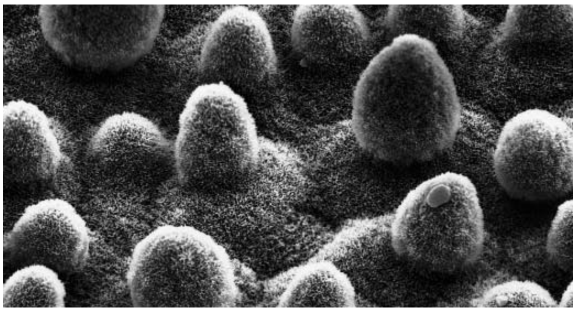

Figure 3: Lotus leaf surface[9]

All of the leaves examined that had similar hierarchical, dual-scale structures to the Lotus leaf showed water contact angles of greater than 150^o, while the leaves that were easily wetted showed very little in the way of surface texturing. Also of interest was the observation that the leaves which had this dual-scale roughness on them showed self-cleaning properties; none needed cleaning prior to examination by scanning electron microscope (SEM). The smooth leaves looked at in the study, however, needed to be cleaned of debris before examination. Other common examples of leaves that show superhydrophobicity include the cabbage family, (*brassica*), taro, (*Colocasia esculenta*) and Lupin (*Lupinus*).[10]

Superhydrophobic surfaces found in nature are not limited to plants; there are many other examples of superhydrophobic surfaces found in the bird and insect realms. For example, on close inspection the water strider's legs show a dual-scale roughness with setae in the micrometre scale domain, on which sit nanometre scale grooves at the surface. These grooves are coated with a hydrophobic wax which renders their legs superhydrophobic. Each of the water strider's legs is able to support approximately 15 times the total weight of the water strider before piercing the water surface,[11] which enables the water strider to effortlessly and elegantly walk on the surface of water.

Perhaps counter-intuitively the Namibian desert beetle utilises a superhydrophobic surface to harvest water in what is a particularly dry, hostile environment. On the macroscopic scale the surface of the beetle is randomly covered by smooth bumps. The profile at the top of these bumps is smooth at the microscopic level as well, but in the sloping areas and troughs between the peaks is a wax covered microstructure. The Namibian desert fog condenses on the smooth peaks of these bumps, which are hydrophilic, while the wax coated microstructures surrounding these bumps behave as superhydrophobic tracks. When a water drop that condenses at the top of one of these peaks grows to be large enough to overcome the work of adhesion between the water and the surface, it dislodges from the hydrophilic spot and is guided down the superhydrophobic tracks and into the beetle's mouth.[12]

In 2007 Bormashenko *et al*[13] studied the wetting characteristics of pigeon feathers. Before the study was carried out it was widely believed that the water repellency shown by the outer feathers, or pennae, of pigeons was due to preen oil left behind after the bird's grooming routine. In this study the feathers tested were thoroughly washed in ethanol then water to remove any contaminants and preen wax in order to investigate the effect of the feather morphology on wetting. The wetting characteristics of the cleaned feathers were then measured and SEM images of the feathers recorded.

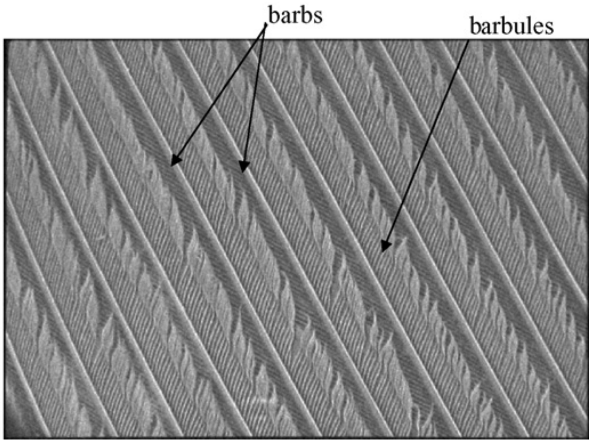

Figure 4: SEM image of a pigeon feather[13]

The SEM images showed the feathers (Figure 4) were composed of barbs coming off a central rachis at 200µm intervals. Barbules protrude from these barbs at 10µm intervals to give a highly textured surface. It was shown in the study that the biological material making up the structure of the feather was hydrophilic, but when organised into the hierarchical structure of a feather the surface was hydrophobic. While contact angles in most spots of the cleaned feathers were below the criterion for the surface to be defined as superhydrophobic, there were some areas where the contact angle was greater than 150˚. From this it can clearly be concluded that the small-scale structures of surfaces are of great importance to their wetting characteristics.

The recurring theme in these examples of superhydrophobic surfaces shown by Nature is the combination of a hierarchical dual-scale roughness which is coated with a hydrophobic wax. Nature has been experimenting with and evolving these surfaces for its various purposes over millions of years, so its examples and ideas serve as an excellent starting point for the preparation of man-made examples.

1.2 Concepts Behind Superhydrophobicity

1.2.1 Surface Tension

A molecule of water in the bulk phase of a water droplet experiences an attraction to neighbouring water molecules[14] in all directions, such that these forces cancel out and a net zero force acts on that molecule (Figure 5). This is not the case for water molecules that find themselves at the liquid-vapour interface at the edge of the water droplet. The forces exerted on these molecules from neighbouring water molecules are not balanced by attractions to the air outside of the water droplet, so these molecules are subject to a net inwards force (Figure 5).[15]

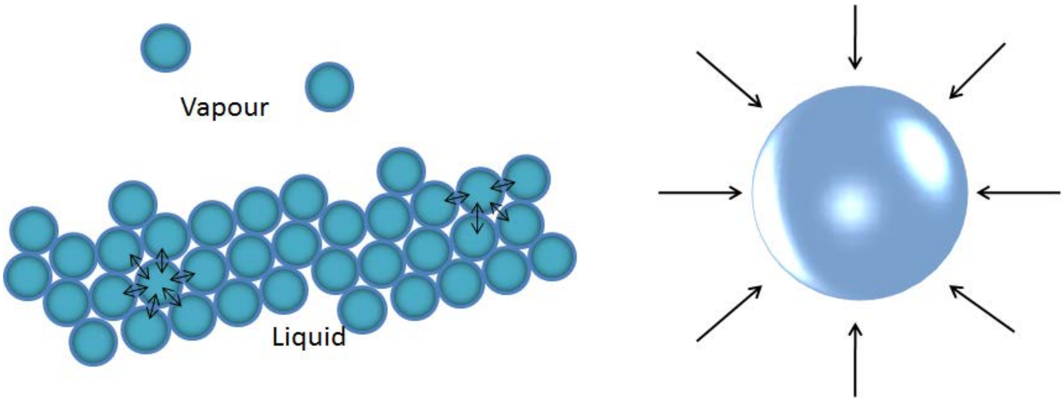

Figure 5: A schematic of the liquid-vapour interface (left); a spherical droplet showing the inwards force vectors as a result of surface tension (right).

This gives rise to a surface tension, γ, which has the units of force per unit length. This property is often referred to as surface energy, which has units of work per unit area; both surface tension and surface energy are dimensionally equivalent. A precise, mathematical definition of surface tension is given as:[14]

$$\left.\frac{\partial G}{\partial A}\right|_{T,P,N_i} \equiv \gamma \ldots\ldots\ldots (1)$$

The surface tension (γ) of a substance i is the increase in Gibbs free energy (G) per increase in surface area (A) at constant temperature (T), pressure (P) and number of moles(N_i) of substance i.[14] A simple way of conceptualising the property is to treat it as the amount of work required to move molecules from the bulk phase of a liquid to the liquid-vapour interface.

A water droplet, being fluid, can distort in shape to minimise its surface free energy.[10] In the absence of gravity a water droplet will adopt a spherical form as this arrangement has the maximum number of molecules surrounded by other molecules, which in turn maximises attractive molecule-molecule interactions.[15]

In practice most water droplets seen in everyday life are not spherical in shape due to the influence of gravity. However, as the size of a system is reduced the effect of gravity begins to lessen relative to the effect of surface tension. This is because gravity acts on the mass of the drop, which is proportional to the third power of the radius of the drop, while surface tension forces are directly proportional to the radius of the drop.[10] At large drop sizes gravity has a large effect, but smaller drop sizes see it have negligible effect on drop shape as surface tension forces begin to become more important. This is why large spherical drops are not seen, and smaller water droplets generally give a closer approximation to a spherical form.

The point at which the two effects exert the same influence is the capillary length of water, which is 2.73mm. For length scales much smaller than this, surface tension forces dominate over gravity.[10] This goes some way to explaining some of the striking phenomena shown by small insects in nature such as the ease at which the water strider walks across water, as many species are of this size range or have appendages in this size range.

For the humble water strider, water must seem to behave as a totally different substance to how, for example, an elephant would perceive water. So too as modern equipment gets miniaturised and nanotechnology becomes an increasingly important area of research in this day and age, these surface tension forces become increasingly important and cannot be ignored.

1.2.2 Models of Wetting Systems

Three models are most commonly used to describe and predict the interaction of water with solid surfaces, and to promote an understanding of the requirements for the preparation of superhydrophobic surfaces.[16]

1.2.2.1 Young Model

Over 200 years ago in his 1805 *Essay on the Cohesion of Fluids*,[17] Young gave a mathematical treatment to describe the "appropriate angle of contact" for a water droplet in contact with a flat, chemically homogeneous solid surface. The surface tensions between the surface and the liquid (γ_{SL}), surface and the vapour (γ_{SV}) and the liquid and vapour (γ_{LV}) all balance to give an equilibrium contact angle to minimise the surface free energy of the water droplet (Figure 6). Using simple trigonometry, the Young contact angle can be calculated using the Young Equation:

$$cos\theta_{Young} = \frac{\gamma_{SV} - \gamma_{SL}}{\gamma_{LV}} \dots\dots\dots (2)$$

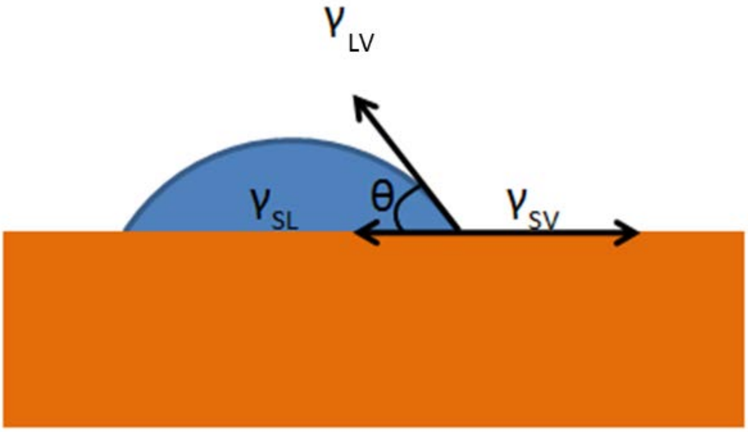

Figure 6: Young's model of a water droplet interacting with an ideal surface

If γ_{SV} is greater than γ_{SL}, then $0^0<\theta<90^0$ i.e. the surface is hydrophilic. The converse also applies; if γ_{SV} is less than γ_{SL}, then the surface will be hydrophobic. If $\gamma_{SV}= \gamma_{SL}$ the contact angle is 90° and there is no change in energy on wetting.[10]

What is clear from the Young Equation is that surface energy directly affects the wetting characteristics of a solid.[8] The highest contact angles exhibited on flat solids are seen on fluorinated materials which have extremely low surface energies in the region of 5.6 mNm^{-1}.[18] In contrast, the surface tension of water at 20°C is 73 mNm^{-1}.[19]

However, the property of a low surface energy on its own is not sufficient to produce a superhydrophobic material. A flat, low energy fluorinated surface only exhibits contact angles in the region of 120^0,[16,18] which is the limit of a purely chemical hydrophobicity. This is far below the required 150^0 contact angle for a surface to be deemed superhydrophobic, so clearly some other factor or factors must be taken into account to describe the interaction of water with superhydrophobic surfaces.

1.2.2.2 Wenzel Model

Wenzel in his 1936 paper[20] began to move away from Young's ideal surface and recognised the importance of the topology of a solid surface when considering its interaction with water. In his model of wetting, water is in contact with the surface in a similar fashion to Young's model, but it takes into account a surface that is not ideally flat (Figure 7). Wenzel noted that for a roughened surface there is a "greater intensity of surface energy" than for a planar surface of the same substrate, and introduced a roughness factor, r:

$$r = \frac{Actual\ Surface\ Area}{Projected\ Surface\ Area} \dots\dots\dots (3)$$

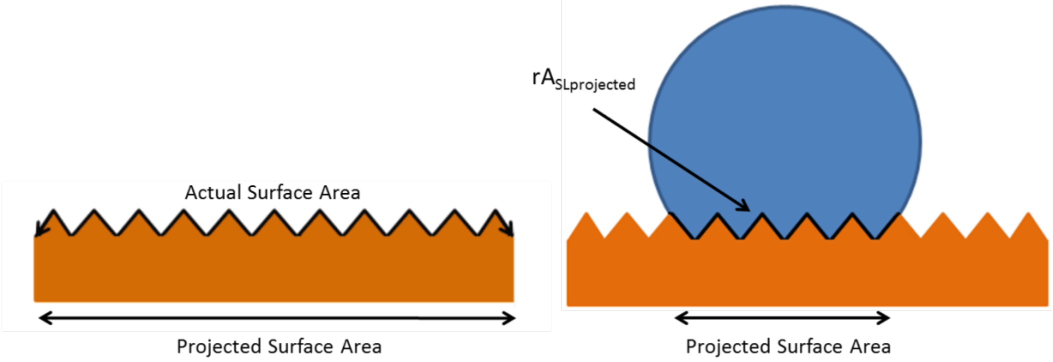

Figure 7: Wenzel's roughness factor parameters (left); water interacting with a roughened surface under the Wenzel regime (right)

On a roughened surface the solid-liquid interfacial area can now be expressed as:

$$A_{SLrough} = rA_{SLprojected} \dots\dots\dots (4)$$

Since $r > 1$ for a roughened surface, $A_{SLprojected}$ will always be smaller than that for a smooth surface if the same solid-liquid interfacial area is to be maintained. For an initially hydrophobic surface, this roughening will make water droplets adopt a more spherical form,[20] consequently increasing the contact angle made with the same surface but of smooth topography.

The opposite applies for an initially hydrophilic surface; under Wenzel's model the surface roughness "magnifies the wetting properties of a solid"[20] (Figure 8). The introduction of the roughness term modifies Young's equation to yield the Wenzel Equation (Equation 5).

$$cos\theta_{Wenzel} = r\left(\frac{\gamma_{SV} - \gamma_{SL}}{\gamma_{LV}}\right) = rcos\theta_{Young} \ldots\ldots\ldots (5)$$

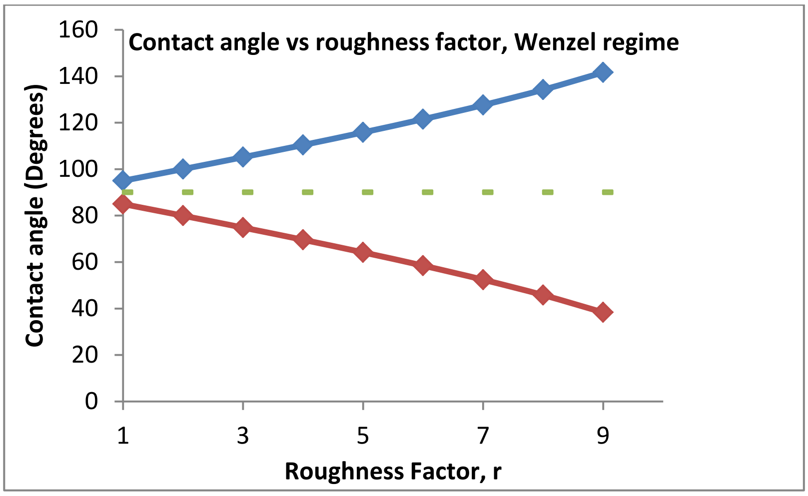

Figure 8: Variation of contact angle with roughness as predicted by the Wenzel Equation for an initially hydrophobic surface (blue line) and an initially hydrophilic surface (red line)

1.2.2.3 Cassie-Baxter Model

A third model of wetting was proposed by Cassie and Baxter in 1944,[21] which describes a liquid drop suspended on top of randomly distributed pillars each characterised by their own surface tensions $\gamma_{i,SV}$ and $\gamma_{i,SL}$. Each pillar takes up a fraction of the surface f_i such that $f_1 + f_2 + \cdots f_n = 1$. For the total system,

$$\gamma_{SV} = \sum_{i}^{n} \gamma_{i,SV} f_i \ldots\ldots\ldots (6)$$

And

$$\gamma_{SL} = \sum_{i}^{n} \gamma_{i,SL} f_i \ldots\ldots\ldots (7)$$

Substituting Equations 6 and 7 into Young's Equation (Equation 2) gives the equation:

$$cos\theta_{CB} = \sum_{i}^{n} f_i \frac{\gamma_{i,SV} - \gamma_{i,SL}}{\gamma_{LV}} = \sum_{i}^{n} f_i cos\theta_{i,Young} \dots\dots\dots (8)$$

Where θ_{CB} is the Cassie-Baxter contact angle. The above equation is of little practical use as written, however it can be simplified. On extremely rough surfaces the water droplet does not conform to the topology of the surface, instead the water droplet is suspended on top of solid pillars with pockets of air interspersed between[16] (Figure 9).

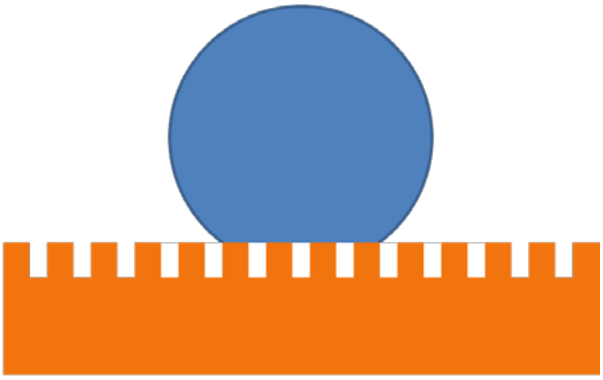

Figure 9: A water droplet interacting with a surface under the Cassie-Baxter regime

By treating the surface as a two component material with the water droplet having a fraction in contact with a solid, f_s, and a fraction in contact with air, f_a, the equation simplifies to:

$$cos\theta_{CB} = f_s cos\theta_{Young} + f_a cos\theta_a \dots\dots\dots (9)$$

Where θ_a is the contact angle water makes with air, which is 180°.[16] Putting this value into Equation 9 gives the Cassie-Baxter Equation:

$$cos\theta_{CB} = f_s cos\theta_{Young} - f_a \dots\dots\dots (10)$$

The Cassie-Baxter equation does not explicitly have a roughness factor as seen in the Wenzel Equation (Equation 5), but it can easily be imagined that as roughness increases so too will f_a, the fraction of air present underneath the water drop.[22] The Wenzel equation predicts that with increased roughness initially hydrophobic surfaces become more hydrophobic, and initially hydrophilic surfaces become more hydrophilic; this is not what the Cassie-Baxter equation predicts.

If water is interacting with a roughened surface according to the Cassie-Baxter model, increased roughness, and in turn an increase in f_a, still increases the contact angle of an initially hydrophobic surface. Where it differs from the Wenzel Equation prediction is that it also predicts an increase in the contact angle of initially hydrophilic surfaces with increased roughness and an increase in f_a (Figure 10). This explains the wetting behaviour seen from the pigeon feathers seen in Bormashenko's study,[13] which showed hydrophobic contact angles on a microstructured surface composed of hydrophilic biological materials.

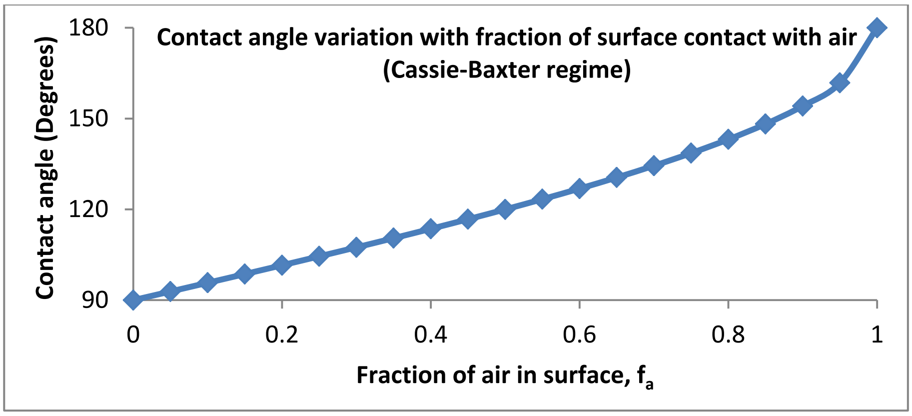

Figure 10: Variation of contact angle with fraction of air present under water droplet

1.2.2.4 Which Model to Use?

A given surface is not limited to only behaving under one of the Cassie-Baxter or Wenzel wetting regimes. Water condensed onto superhydrophobic surfaces often deposits in the Wenzel state, following the contours of the surface, but a water droplet deposited carefully onto the same surface is able to exist in the Cassie-Baxter state.[18,23] If this droplet is disturbed by vibration, or a force is applied to it or it is dropped from a height a transition to the Wenzel state can be induced.[18,23]

In cases such as this the two states are thought of as different energy minima with an energy barrier between them. The energy supplied by disturbing the droplet is enough to overcome the barrier between the metastable (Cassie-Baxter) state and the stable (Wenzel) state in the above example.[18,23]

Further complicating matters is the issue that for complex topographies a composite of both Wenzel and Cassie-Baxter states can exist[10] (Figure 11).

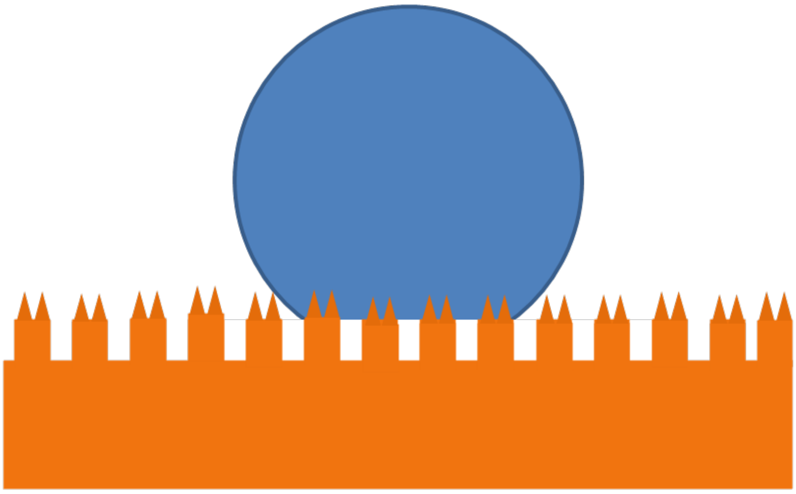

Figure 11: Water droplet on composite Cassie-Baxter and Wenzel surface

The two states behave quite differently; superhydrophobic surfaces with very high contact angles are typically found to be in the Cassie-Baxter state,[24] and Cassie-Baxter state surfaces tend to allow drops of water to roll off far more easily than Wenzel surfaces.[23] Tilting a material which is following the Cassie-Baxter regime past the critical angle for reflection at an air-water interface imparts a silver mirror like finish to the submerged material.[1] This is indicative of a layer of air between the water and the surface and is a simple way to confirm which regime the surface is following.

1.2.2.5 Controversy over Wenzel and Cassie-Baxter Models

The validity of the Cassie-Baxter and Wenzel models has been challenged by Gao and McCarthy,[25] in their provocatively titled 2007 paper "*How Wenzel and Cassie Were Wrong*" where they produced results that contradicted the what the Cassie-Baxter and Wenzel models would predict. They surmised that the nature of the three-phase contact line formed at the solid-liquid-vapour junction is what influences the contact angle, rather than contact areas under a drop, which is an idea both the Wenzel and Cassie-Baxter models are based on.

Marmur[7] and McHale[26] came to defend the Cassie-Baxter and Wenzel models in subsequent papers. Marmur's argument for the anomalous results found by Gao and McCarthy centre around the small drop sizes used in their experiments. Gao and McCarthy used drop sizes of only up to two and a half times the size of surface heterogeneities in their experiments which gave results that were inconsistent with the Wenzel and Cassie-Baxter models' predictions. Marmur notes that as a water drop gets larger relative to the scale of roughness of the surface the Wenzel and Cassie-Baxter models give better and better approximations of contact angle and a water droplet ratio of two or three orders of magnitude larger than surface heterogeneities is required for good agreement between predicted and experimental data.

McHale[26] points out that "In the case that a surface is everywhere similar and isotropic the roughness and Cassie-Baxter fractions...become global constants." This supports Marmur's assertion that as drop size increases the Wenzel and Cassie-Baxter models begin to fit experimental more closely. As drop size gets larger, it will cover many small topographical and chemical imperfections such that eventually the Wenzel roughness factor or Cassie-Baxter fraction average out to become a "global constant". Small drops placed on areas where there is a single defect (which were engineered by Gao and McCarthy) are not described by a "global constant" for the Wenzel roughness factor or Cassie-Baxter fractions, and McHale argues that instead local values should be used in these cases.

Whether the models do quantitatively predict contact angles for various surface topologies is one issue, but the main value obtained from these models for the materials scientist interested in the fabrication of superhydrophobic surfaces comes from the combination of the basic ideas of the Young, Cassie-Baxter and Wenzel models. Even the biggest sceptics, Gao and McCarthy, in a separate (later) paper from the challenge to the Cassie-Baxter and Wenzel models acknowledge the respective authors' contributions as "insightful, profound and demonstrably abundantly useful".[27] These models emphasise to the materials scientist that for a surface to be superhydrophobic there are clearly two main requirements: low surface energy and high surface roughness.[22]

Over 200 years on from Young's Essay, debate still continues over the interaction of water with solid surfaces, which is sobering to note in that it is something that is observed so often in everyday life but is still not yet fully understood.

1.2.3 Contact Angle Measurement

WCA measurements are obtained using a contact angle goniometer. Modern contact angle goniometer systems record on camera an image of a water droplet placed on a surface. The resulting image is then able to be processed by computer software to give a calculated WCA. This technique is dependent upon excellent image resolution of the baseline of the surface and three phase contact line for the droplet on the surface.[28] This can be very difficult to achieve at high contact angles, particularly if there is any macroscopic roughness on the surface and contact angles venture into the range of superhydrophobicity.

While the reporting of a WCA value may seem to be a simple way of quantifying the hydrophobicity of a surface at first, care must be taken in the interpretation of contact angle data. Without due consideration, there are many pitfalls that can lead one to make incorrect conclusions about the wetting characteristics of a surface. Marmur, in 2006,[29] reviewed of some of the considerations that need to be taken in the field. These are summarised below.

1.2.3.1 The Apparent Contact Angle

When the WCA of a roughened surface is being measured, the quantity that is being assessed is known as the “apparent contact angle”, which is a different quantity to the actual contact angle that water makes at the three phase contact line. Figure 12 shows the distinction between the two quantities. The actual contact angle is the contact angle water makes at a localised portion of the roughened surface. This quantity is often experimentally inaccessible to measure, so the quantity that is seen is the apparent contact angle, the angle that a water droplet makes with a surface on the macroscopic scale. Not surprisingly, the two values can often have a large difference.[29]

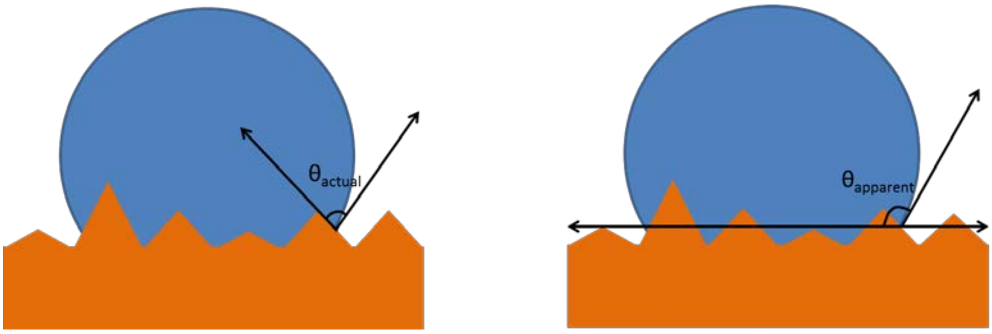

Figure 12: Actual contact angle (left); apparent contact angle (right)

Surface heterogeneities have large implications for calculating and reporting the apparent contact angle. The seemingly small change of varying the position of the three phase contact line by as little as one pixel in computer software that accompanies a modern contact angle goniometer can change the calculated apparent water contact angle by almost 5°.[28]

In fact, subtle changes in experimental conditions such as lighting effects and focus of the camera also can have large effects on contact angle values calculated for a given water droplet. Changing the lighting on a given droplet can vary a calculated water contact angle by almost 2°, while changing the focus can vary the calculated apparent contact angle by almost 5°.[28]

1.2.3.2 Contact Angle Hysteresis

The measurement of a single contact angle that water makes with a solid surface is not as informative as the Young, Wenzel and Cassie-Baxter models outlined in Section 1.2.2 might imply. More often than not there is a difference between the contact angle a drop of water makes with a surface as the drop volume increases (a large contact angle is seen) and the contact angle made as the drop volume is decreased (a smaller contact angle is seen).[22,23] A similar behaviour is observed when a surface with a water drop on it is tilted until the drop moves (Figure 13).

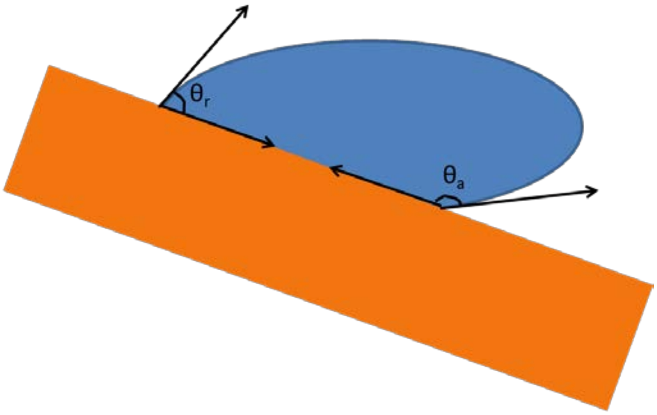

Figure 13: Contact angle hysteresis

In order for the drop to move, one side of the drop has to advance and the other side of the drop has to recede. The contact angle made on the advancing side, θ_a, is seldom the same as that on the receding side, θ_r, and the difference in the two values when the drop starts to move is known as contact angle hysteresis.[27] The angle at which the drop begins to move is referred to as the roll-off angle, θ_{ro}.[30]

Superhydrophobic surfaces show a very low contact angle hysteresis,[6] which together with a large contact angle allows water to roll off the surface at the slightest of perturbations. This gives low water droplet roll-off angles. Water is more likely to roll across a superhydrophobic surface rather than slide,[6] which is of great importance to the self-cleaning mechanisms associated with the *Lotus Effect* of these surfaces, as the drops pick up debris from the surface as they travel along and roll off it.[9]

Surfaces that exist in the Wenzel state generally show a higher contact angle hysteresis than those in the Cassie-Baxter state. The water that conforms to the surface topology at the receding side of the drop can drastically decrease the receding contact angle thereby increase the value of contact angle hysteresis. This trapping of the liquid does not occur on Cassie-Baxter surfaces, so larger receding contact angles are seen along with lower roll-off angles.[22]

A common method of quantifying the superhydrophobicity of a surface is to report both the advancing and receding contact angles of a water droplet. This task is not without its practical difficulties, however. For a real surface there may be number of metastable WCAs that lie between advancing and receding contact angles, each with an energy barrier between them (Figure 14).

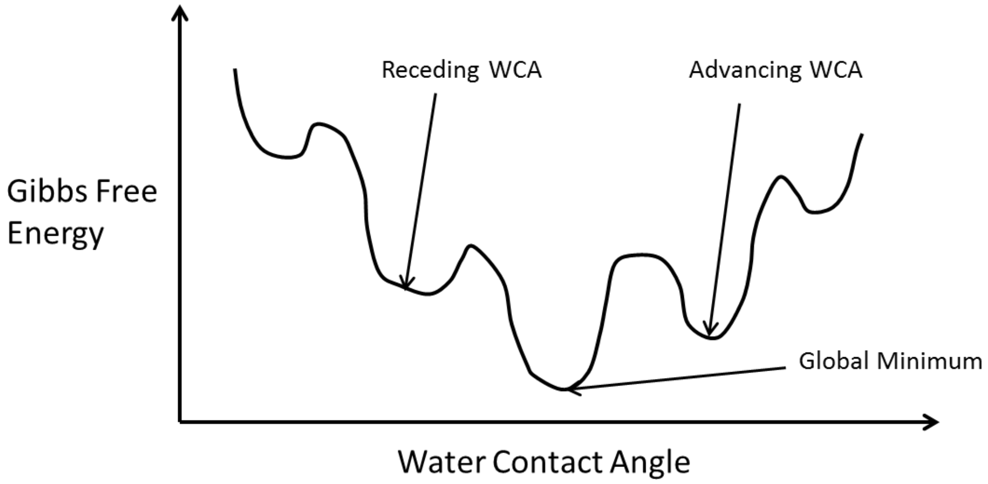

Figure 14: Energetics of contact angle hysteresis

This leads to the three phase contact line getting pinned as the water droplet is increased or decreased in size, and once the energy barrier between one state and another is overcome the three phase contact line surges in what is sometimes known as “stick-slip” motion.[29] Additionally there is an uncertainty as to which advancing or receding contact angle is being measured and reported.

1.2.3.3 Roll-off Angle

When a water droplet is on a surface which is tilted, gravity acts upon the droplet, trying to pull the droplet along the surface. Competing against this force is the surface tension force which is caused by the contact angle holding it from sliding.[22] Just before the droplet starts to move, the two quantities are equal:

$$\gamma_{LV}(cos\theta_r - cos\theta_a) = \frac{mg}{w} sin\theta_{ro} \ldots\ldots\ldots (11)$$

Where m is the mass of the droplet, g is acceleration due to gravity, w the width of the drop and θ_{ro}, the incline of the surface. The equation predicts that a small contact angle hysteresis will give a small roll-off angle. Superhydrophobic surfaces can show a low roll-off angle even with a contact angle hysteresis of greater than 5° due to their having a small width of water droplet in contact with the surface, w.[22] A roll-off angle gives some indication of contact angle hysteresis range and the width of an applied water droplet interacting with a surface; both quantities are desired to be minimised in superhydrophobic surface preparation to give low roll-off angles. A surface’s roll-off angle is therefore a reasonable way to quantify superhydrophobicity, provided the water droplet applied is of consistent size. This quantity is readily and easily measured, and will be used to assess and compare the superhydrophobic surfaces prepared in this work.

1.3 Synthetic Superhydrophobic Surfaces

With the lessons gleaned from Nature, the insights offered by Young, Wenzel, Cassie and Baxter and with the maturation of micropatterning technologies[30] many synthetic procedures for preparing superhydrophobic surfaces have been reported. In spite of the wealth of reported synthetic procedures, relatively few of them involve applying a superhydrophobic surface to metals, which is the predominant focus of this work. Kim, in his 2008 review,[22] generalised synthetic procedures into three categories which are summarised with examples (with an emphasis on metals where possible) below.

1.3.1 Roughening Hydrophobic Surfaces

This synthetic strategy involves roughening an originally hydrophobic surface to give it the necessary morphology or roughness to induce superhydrophobicity. Unfortunately it is limited in the materials one can start with since the initial material generally needs to be hydrophobic which limits the strategy's application to metals.

In a very early example in 1953 Bartell and Shepard[31] poured paraffin wax into an aluminium mould which left regular pyramidal structures on the resulting wax structure. Several moulds were used and the height, width and angle of inclination of the pyramids were varied and both the advancing and receding contact angles recorded. Several of the more roughened samples had advancing contact angles of greater than 150˚; the conclusion of the paper entertains the thought of a very finely divided surface of wax pillars interacting with water, where they expect an apparent contact angle of close to 180˚. Unfortunately there is a limit to the scale of roughness that can be achieved with the methods and technology employed in the study so their hypothesis wasn't tested.

In recent times much more exotic methods have become available to researchers for tailoring a surface to a desired topography. Since fluorocarbons give the highest known Young contact angles they make the ideal starting material for this strategy of roughening an already hydrophobic surface. Morra *et al* in 1989[32] investigated contact angle hysteresis on poly(tetrafluoroethylene) (PTFE) that had been etched in an oxygen plasma. Flat PTFE showed a contact angle of 108˚ while the same material, roughened via plasma-etching, and exhibited an advancing contact angle of 170˚ and receding angle of approximately 145˚.

An elegantly simple method of rendering PTFE superhydrophobic was achieved by stretching Teflon tape.[33] After stretching to 140% of its original length, a WCA of 165±4˚ was seen on the tape. This was attributed to the formation of air gaps in between fibrous PTFE crystals formed on stretching. The stretching process was not harsh enough to disturb the strong chemical bonds along the PTFE chains, but was enough to overcome the weak van der Waals forces between chains. As an air fraction gets introduced between the PTFE crystals a Cassie-Baxter type superhydrophobic surface results.

Phase separation of a multi-component mixture is also able to produce the required roughness for a superhydrophobic surface.[23] A multi component, homogeneous mixture can become immiscible with a change in conditions, for example a change in temperature or pressure. At the interface between the components a bicontinuous structure can occur, and if one component solidifies a porous, bicontinuous structure is obtained. Shirtcliffe *et al*[34] produced a switchable wetting material from the condensation of organotriethoxysilanes in an organic solvent and water. The polymerisation of the silanol groups lowered the dipole moment of the molecules which reduces their solubility, resulting in a porous, hydrophobic polymer that separated from the liquid phase. The porous structure remained after the removal of the solvent, and showed a water contact angle of 155±2˚. After heating to 400˚C the foams were easily wetted, but if only heated to 390˚C superhydrophobicity was maintained. This demonstrates a narrow range over which decomposition of the material occurs. The approach is not limited to the polymerisation of alkoxysilanes, as methods using polyvinyl chloride, polycarbonate and polystyrenes have also been reported.[23]

In 2005, Sun *et al*[35] used a nanocasting method to produce a superhydrophobic surface using poly(dimethylsiloxane) (PDMS). A Lotus leaf was used as a template from which both positive and negative moulds were made using PDMS. The positive PDMS template was remarkably similar in morphology to the actual Lotus leaf and exhibited a WCA of 160˚, while interestingly the negative template only showed a WCA of 110˚. By comparison, a flat surface of PDMS has a WCA of 105˚. These results show clearly that the orientation of surface roughness is also an important factor to consider when preparing superhydrophobic surfaces.

Superhydrophobic surfaces consisting of inorganic material have also been prepared. In 2005 Feng, Zhai and Jiang reported the synthesis of a superhydrophobic TiO_2 coating on a glass substrate.[36] TiO_2 nanorods were deposited on a glass substrate by immersing in an aqueous $TiCl_3$ solution supersaturated with NaCl, and storing in the dark. A WCA of 154±1˚ was seen on the finished material, but what was also striking about the material is that after irradiation with ultraviolet light the material wetted. Storing in the dark once again for a time restored the superhydrophobic nature of the material. Also of interest to note is that flat TiO_2 is hydrophilic, so here a superhydrophobic surface has been prepared with an initially hydrophilic material. A surface composed of zinc oxide nanorods was also reported in 2003[37] which showed very similar properties to the TiO_2 example above with regards to switchable wetting.

1.3.2 Lowering Surface Energy of Roughened Substrates

This synthetic strategy involves chemical modification of a roughened surface to lower its surface energy. The approach has the advantage of allowing the superhydrophobic surface to be applied to a bulk substrate of the desired characteristics.[38] Superhydrophobic surfaces on metal substrates tend to fall under this category, since the metals themselves are not hydrophobic. Alkyl or polyfluoroalkyl chain silanes, thiols and carboxylic acids are commonly used to lower the surface energy in this synthetic strategy since they are able to readily form a self-assembled monolayer (SAM) on a variety of substrates.

There are a number of methods available to produce the desired topology for a superhydrophobic surface. The plasma etching process which was relevant to rendering initially hydrophobic surfaces superhydrophobic in Morra *et al*'s PTFE example[32] can also be applied to a variety of other substrates to impart a rough surface texture. Poly(ethylene terephthalate) (PET) can be etched in an oxygen plasma, followed by chemical vapour deposition (CVD) of a tri-methoxy fluoroalkylsilane to generate a transparent surface with a water contact angle of over 150˚.[39] The diversity of materials over which the plasma etch can be effective in preparing superhydrophobic surfaces is exemplified by Breedveld *et al*'s 2008 publication[40] where paper showed a WCA of 167±1˚ after being subjected to a low temperature plasma etch and plasma enhanced CVD of pentafluoroethane.

Lithographic techniques give researchers great control over the roughness, regularity and the geometry of surface features to create superhydrophobic surfaces to study and better understand the fundamentals of wetting.[22,41,42] The technique of lithography is analogous to a stamp in that it involves transferring a design from a master surface onto a substrate surface[23] and the master surface is then able to be re-used to generate more copies. The surface is now able to be used as a substrate for deposition of a low surface energy material,[23] or as in the case of Sun *et al*'s PDMS Lotus leaf,[35] it can already be superhydrophobic straight out of the mould.

Photolithography utilises a photoactive polymer layer which is exposed to light through a photomask, after which the polymer is removed leaving an image of the mask on the surface. A 2006 study[18] systematically investigated the effects of surface topography on WCAs. Photolithographically structured silicon surfaces comprised of flat-topped pillars were prepared, and the technique allowed for parameters such as pillar height, diameter, top perimeter and disposition to be carefully changed and controlled. Once the surface had been prepared to the desired texture, it was treated with polyfluoroalkylsilane to lower the surface energy. Several of the surfaces prepared in the study exhibited WCAs of greater than 160˚.

1.3.2.1 Superhydrophobic Metal Surfaces

In an early example in 1998 the Kao corporation reported that anodically etched aluminium foils treated with 1H,1H,2H,2H-perfluorooctyltrichlorosilane showed WCAs in the order of 160˚.[43] The anodisation process left a fractal surface on the metal which combined with the dense packing of the fluoroalkyl groups on this topology rendered the surface superhydrophobic. The surfaces also showed good oil repellency characteristics.

Dislocation defects in a crystalline metal surface are high energy sites which are attacked by etchants and dissolve before other areas of the metal. Qian and Shen[44] used chemical etching as a means of roughening the surface of copper, zinc and aluminium, followed by treatment with a polyfluorotriethoxysilane to lower the surface energy of the now roughened metal surface. WCAs of over 150˚ were achieved on all three of the metals after varying etching times to optimise surface roughness.

Liu *et al*[45] investigated the corrosion behaviour of copper wafer which had been etched in nitric acid and subsequently left for ten days in an ethanol solution of tetradecanoic acid. The resulting material showed small flower-like structures on the surface and a WCA of 159° as the carboxylic acid formed a SAM on the native oxide coating of the copper. In 2010, a very similar strategy was employed to render magnesium superhydrophobic after etching in sulfuric acid and hydrogen peroxide solutions followed by immersion in stearic acid.[46]

In 2007, Larmour *et al* reported a simple method of synthesising a superhydrophobic surface on copper and zinc substrates.[1] Silver was galvanically reduced onto the chosen substrate metal and deposited as a very rough layer. The surface energy of the material was then lowered by adsorption of 1H,1H,2H,2H-perfluorodecanethiol onto the now roughened surface. The resulting foil had a WCA of 173±1° and a roll-off angle of 0.64±0.04° for a 20µL water droplet. The synthesis is particularly appealing in two aspects in that no specialised equipment is required, and the wetting properties of the resulting surface can be tailored by careful choice of thiol adsorbed.

Another example of galvanic reduction of a metal followed by chemical surface modification has been used to render stainless steel superhydrophobic. In 2008, Fu and He deposited nickel as micro and nanoscale structures onto stainless steel. Subsequent treatment with 1H,1H,2H,2H-perfluorodecyltrimethoxysilane gave a superhydrophobic surface on a stainless steel substrate.[47]

In 2009, Nieto *et al*[48] used porous alumina as a template to grow nickel and platinum nanowires which were chemically modified with stearic acid. A conductive backing was applied to the alumina, which acted as a cathode onto which nickel or platinum was reduced which deposited down the pores of the alumina structure. The alumina was dissolved away in sodium hydroxide to leave behind a nickel or platinum "nanocarpet" consisting of the metal nanowires, each wire was approximately 200nm wide. The nanocarpets were treated with a solution of stearic acid to form an SAM over the rough surface and lower the surface energy. The nickel surface showed a static WCA of 154±2° while the platinum surface showed a WCA of 167±2°.

1.3.3 Depositing Hydrophobic Surfaces with Rough Textures

This method is very similar to the ideas outlined in Section 1.3.1, so faces the same restriction with regards to limitations of what initial material may be used. Rather than removing some of an already solid hydrophobic surface to give the morphology required for superhydrophobicity, the hydrophobic material is deposited in a controlled way to give a superhydrophobic surface.

One method that falls into this category is electrospinning,[49] where very thin polymer fibres are deposited from a charged jet onto a grounded collector plate. These fibres can then be aggregated into a mat to make a superhydrophobic surface. In one example in 2009, Han and Steckl[50] used a coaxial electrospinning method to electrospin a Teflon fluoropolymer, Teflon AF, and poly(ε-caprolactone) and yield a coaxial fibre membrane which displayed a WCA of 158° and water roll-off angle of 7°.

Plasma polymerisation can be used to deposit hydrophobic materials to induce superhydrophobicity. In 2000 Matsumoto *et al*[51] carefully controlled the plasma polymerisation of tetrafluoroethylene to give a solid with a "powder-like" finish on a silicon wafer, which showed superhydrophobic contact angles.

Reaction of metal salts with alkanethiols can form metal alkanethiolates which can then be deposited as a film on a chosen substrate. For example, dodecanethiol was reacted with cadmium chloride to give cadmium dodecanethiolate. This was then deposited onto silicon wafer as a film composed of small flower-like structures to give a material which showed a WCA of 154±2°.[52]

Using very similar initial materials to Larmour *et al*,[1] in 2011 Xu *et al*[53] rendered copper superhydrophobic by reacting silver nitrate with octadecanethiol to form the silver alkanethiolate. Once this was sprayed onto copper mesh the silver alkanethiolate deposited in small structures on the nanometre scale. The resulting superhydrophobic copper mesh did not allow water to pass through the mesh pores which were up to 400μm across.

1.4 Titanium Metal

Titanium is the ninth most common element in the earth's crust at 0.6% abundance, though it is seldom found in high concentrations and the pure metal does not exist in nature.[54] It was first discovered in 1791 when a Cornish vicar, William Gregor, extracted an impure metal oxide of a new element on treatment of ilemenite ($FeTiO_3$), with hydrochloric acid. The ilemenite was magnetically separated from sand[55] found in a local river, Helford in the Menachan Valley in Cornwall, England.[54] Independently four years later a German chemist, Martin Heinrich Klaproth, discovered the same metal oxide in a sample of rutile (TiO_2) ore and named the metal titanium after the Titans. In Greek mythology the Titans were the children of Heaven and Earth and were doomed to live in the hidden fires of the earth.[56] This name gives some indication of the difficulties Klaproth experienced in extracting the oxide from the ore.

Titanium metal is not able to be refined by the common method of reduction with carbon, since it forms a very stable and intractable carbide. It is also reactive at high temperatures toward oxygen and nitrogen, so is likely to be contaminated unless air is excluded during the preparation.[56] It was not until 1910, over a hundred years after Gregor's and Klaproth's discoveries, that a pure sample of the metal was prepared when Matthew Albert Hunter reduced $TiCl_4$ with sodium to give pure titanium.[56] In 1932 Wilhelm Justin Kroll, considered the father of the titanium industry, prepared substantial amounts of titanium on reducing $TiCl_4$ with calcium. He later changed the reducing agent to magnesium to give what is now known as the "Kroll process," which is to this day the most widely used method of preparing titanium.[54]

The Kroll process is a very expensive one, which in turn makes titanium an expensive commodity.[55] Nonetheless, the metal's unique and desirable properties offset the high cost involved in titanium purification. Titanium shows a low density when compared to other metals of similar mechanical strength being just over half the density of steel at 4.51gcm^{-3} [56] and is resistant to corrosion due to a protective oxide layer that readily forms at the surface.

This combination of high strength-to-weight ratio and corrosion resistance make titanium ideal for use in specialised applications including turbine engines, marine equipment, aircraft components and medical implants.[55] For example, as resources such as fuel grow scarcer and there is a demand for aircraft to be more frugal with fuel while carrying larger payloads, the cost of utilising titanium becomes rationalised. As of 2003, the automobile industry would tolerate a €10 cost for one kilogram saved on each unit, while the aerospace industry is prepared to pay approximately €1,000 to save the same amount of weight. At the extreme, for space applications a cost of €10,000 to save one kilogram is still considered at times to be economically viable.[54]

Titanium features widely as a construction material in these high end applications; its use has been steadily increasing in Boeing's commercial aircraft since the 1960s to the point that it accounts for approximately 9% of the empty weight of a Boeing 777 as of the mid-1990s. Similar growth in titanium usage is also seen in jet engine manufacture, a modern Rolls-Royce engine is comprised of over 30% by weight titanium while early examples in the 1950s consisted of only 3%. From here it can be seen that titanium finds a niche in highly specialised, relatively small production scale applications and their dependence on it continues to grow.

1.4.1 Occurrence of Titanium in New Zealand

New Zealand's black sand beaches have attracted interest from the early days of European colonisation due to the clear presence of high iron content. Records show that in as early as 1848 attempts were made to smelt the ironsands, but these invariably failed as the fine ore choked the furnace. Once this problem was overcome, a new issue arose from the titania present in the ore as it formed an impermeable layer beneath the slag and impeded the workings of the furnace.[57] The major iron ore mineral in New Zealand is titanomagnetite, and magnetic concentrates of ore found throughout the country average 7.8% titanium dioxide,[57,58] and it is this relatively high amount that causes issues with the iron smelting process. This problem has since been circumvented, however.

In spite of the large quantity of titanium dioxide present in New Zealand, to date there has been no production of titanium dioxide from New Zealand deposits.[59]

The recovery of titanium from the titanium bearing slag left over from New Zealand Steel's smelting of Waikato North Head is not deemed to be economically viable with the technology available. Currently the slag is exported and used in overseas steel production.[59] If value could be added to titanium by rendering it superhydrophobic, then this potentially valuable resource could become financially viable to extract in New Zealand.

1.4.2 Previously Reported Methods of Rendering Titanium Superhydrophobic

Untreated titanium is hydrophilic, with the smooth, polished metal exhibiting a WCA of 73±3°.[2] To date, there are very few reported syntheses of superhydrophobic coatings on titanium, and any that have been reported are very recent indeed.

In 2010, Zhang *et al.*[60] reported a synthesis which involved anodising titanium foil in an ammonium fluoride bath followed by treating the surface with a polyfluoroalkyl- triethoxysilane. The anodisation step left an array of titanium dioxide nanotubes on the surface of the foil which provided the roughness required for superhydrophobicity and the fluorinated silane lowered the surface energy by forming a self-assembled monolayer over the substrate. The material achieved WCAs of up to 160° and exhibited anti-corrosion properties.

Silanes with three hydrolysable groups such as the triethoxysilane used above have the ability to polymerise, as well as anchor onto exposed hydroxyl groups at the surface of titanium metal.[60] Unfortunately, difficulty is often experienced in making reproducible SAMs using silanes that polymerise, since there is a large number of variations in the manner in which they are able to polymerise.[61] An obvious solution to this difficulty in reproducibility is to use a silane with only one hydrolysable group, thereby allowing only one type of binding to the surface. However, the other two remaining hydrolysable groups need to be replaced by another non-hydrolysable group to maintain the correct valence on the silicon, and the size of these groups dictates the maximum achievable packing density. The cross-sectional area of an alkyldimethylsilyl group in a densely packed monolayer is approximately twice that seen in alkylthiol SAMs and the SAMs derived from alkylsilanes with three hydrolysable groups.[61] A lower packing density results in a more chemically heterogeneous surface and has been attributed to give larger contact angle hysteresis ranges than their densely packed counterparts,[62] which is an undesirable characteristic in superhydrophobic surface preparation.

Hozumi *et al*[63] have reported the utilisation of the cyclic siloxane 1,3,5,7-tetramethylcyclotetrasiloxane to prepare superhydrophobic surfaces on both titanium and aluminium. CVD processes carried out below the boiling point of the siloxane gave a smooth deposit over the underlying metal but contact angles were below what can be classed superhydrophobic. Once CVD temperatures were raised to 180˚C, above the boiling point of the siloxane, hydrolysis and condensation reactions occurred. These reactions resulted in the deposition of nano- and microscale spherical particles being deposited onto the metal surface. The resulting surface on titanium was superhydrophobic and showed very low contact angle hysteresis, with a θ_a of 163˚ and θ_r of 160˚.

More recently, in 2011, a method involving femtosecond laser ablation was utilised to modify a titanium substrate to give a WCA of 166±4˚.[2] Polished titanium was subjected to laser structuring by a femtosecond Ti:sapphire laser system to leave a surface consisting of large-scale bumps 10-20µm in size, on which irregular undulations up to 200nm in size were present. Interestingly, no subsequent chemical modification of the material was required to achieve the superhydrophobicity. Upon immersion in water, the surface was comprised of initially half air, and the air percentage dropped over one hour until air percentage reached six per cent. This suggests that the Cassie-Baxter state is kinetically favoured on this surface, but the wetted, Wenzel state is thermodynamically favoured and dominates over time. The method is also non-trivial and requires expensive, specialised equipment in the femtosecond laser. A very similar method which utilises a laser to roughen the surface followed by treatment with fluoroalkyl silane has also been reported to give Ti-6Al-4V alloy superhydrophobic properties.[64]

2 Ecdysiastic Superhydrophobic Materials

In 2010 the preparation of a robust superhydrophobic surface was reported by Larmour *et al*[65] which involved cold-pressing copper powder which had been previously rendered superhydrophobic. A porous disk results from the compression which has superhydrophobic characteristics throughout. If the exposed surface of the disk is damaged or soiled, the damaged surface can simply be abraded away to expose another fresh layer beneath (Figure 15). These disks were termed ecdysiastic materials, since this property is reminiscent of *ecdysis*, the shedding of reptiles' skins to expose new ones.

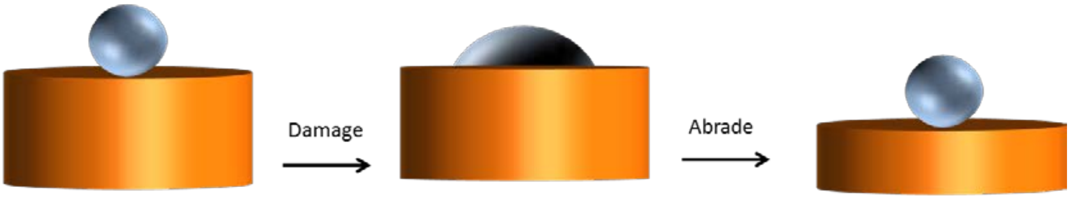

Figure 15: Ecdysiastic superhydrophobic copper disks

This characteristic is particularly appealing in that the micro- and nanoscale roughness that is required for superhydrophobic surfaces renders most preparations extremely fragile, [1,22] which is a major hurdle to superhydrophobic surfaces realising their potential in practical applications.

The requisite roughness for superhydrophobicity in this preparation is achieved by galvanic reduction of silver onto the copper powder. The silver deposits in a rough, textured fashion on the surface of the copper powder. An alkyl- or polyfluoroalkylthiol is then adsorbed onto the silver deposits to form a self-assembled monolayer (SAM) which gives a low surface energy coating.

The preparation can be viewed as a simplified powder metallurgy process. Powder metallurgy is the process where powdered materials are compacted into a desired shape and sintered to bind the powder particles together[66] to give a rigid final product of the desired characteristics. The method is particularly applicable to the large-scale production of small and intricate parts and often there is no subsequent requirement for further machining or finishing of the product.[54]

During the compaction step, the chosen metal powder is compressed to form a “green compact” where the powder is bound together by mechanical interlocking and cold welding of the metal particles. Compression pressures used typically range from 40 to 70MPa for porous metal parts to 1650MPa for high density steel parts.[66] Importantly, the powder does not compress to make a uniformly dense product and maximum density is seen where the die punch meets the powder and decreases as one travels further from the punch. This limits the height/width ratio that can be achieved to prepare parts that have constant density throughout. Once the height/width ratio exceeds a value of 2.0, large variations in density are seen as one travels through the material.[66] All materials prepared and tested in this work are well below this ratio.

The sintering step of the powder metallurgy process involves heating the green compact to a temperature below its melting point. At this temperature, typically around 70% of the metal’s melting point, metallurgical bonds form between the particles as a result of solid state diffusion. As a result, many desirable properties including increased strength, ductility, toughness, electrical and thermal conductivities are imparted to the compact. Sintering is carried out over a wide range of temperatures, for example aluminium alloys are typically subject to sintering temperatures of between 590-620˚C, while tungsten is generally sintered in the range of 2200-2300˚C. Sintering processes for copper are generally conducted at 750-1000˚C.[66]

Unfortunately no data could be found in the literature for the thermal stability of alkanethiol SAMs on silver, but alkanethiol SAMs have been reported to desorb from gold surfaces, which thiols have a very high affinity for, by several groups at temperatures that range around 200˚C.[67] This is far below the temperature ranges at which sintering is carried out, which implies that sintering is not an appropriate process for these materials, so the cold pressed green compact is the final product.

2.1 General Procedure for Coating of Copper Powder

Details are given here for a 70g batch. 70g 200 mesh copper powder (Adelaide Moulding Company) was sifted and washed with 50mL acetone and dried in a 40˚C oven. The dried powder was then washed in 50mL 1% nitric acid, drained, rinsed with distilled water and dried once more in a 40˚C oven. After passing through a sieve, 50mL of 0.02M aqueous silver nitrate was added to the powder with gentle stirring for two minutes. The powder was left to settle in the silver nitrate solution a further three minutes, and the liquid was then carefully decanted off. Another 50mL 0.02M silver nitrate was added to the powder with careful stirring for a further two minutes. The powder was then filtered, rinsed with distilled water, dried in a 40˚C oven and sifted once more. After drying the powder was treated with a solution of selected thiol (Figure 16).

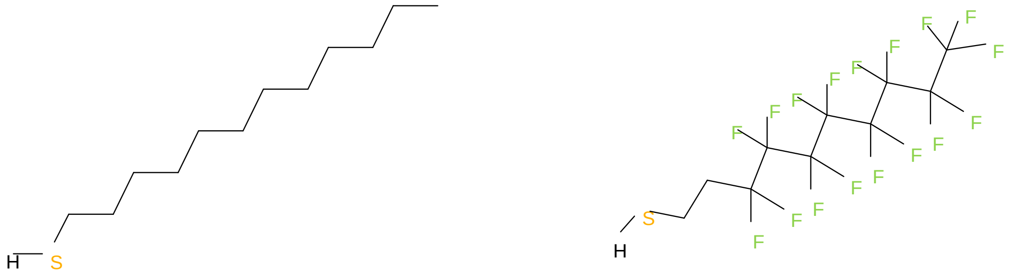

Figure 16: 1-dodecanethiol (left); 1H,1H,2H,2H-pefluorodecanethiol (HDFT) (right)

2.1.1 1-Dodecanethiol Coating

70g of the silver coated copper powder from Section 2.1 was added to 120mL of 0.1M 1-dodecanethiol (Alpha Aesar) (Figure 16) solution in 95% ethanol. This was left overnight with occasional agitation, filtered off, washed with 95% ethanol and dried overnight in a 40˚C oven. After drying the powder was then sifted.

2.1.2 1H,1H,2H,2H-perfluorodecanethiol (HDFT) Coating

25g of silver coated copper powder from Section 2.1 was added to 50mL 0.01M HDFT (Apollo Scientific) (Figure 16) solution in dichloromethane. This was left for 6 hours with occasional agitation, then the solution filtered off and the powder washed with 100mL dichloromethane, and then dried overnight in a 40˚C oven. After drying the powder was then sifted.

2.2 Infrared Spectroscopic Studies of Thiol Coated Powders

In an effort to gain an insight into whether the thiols were indeed present on the treated copper powders, the infrared (IR) spectra of the thiol treated powders from Sections 2.1.1 and 2.1.2 were recorded on a Perkin-Elmer Spectrum Spotlight 200 FT-IR Microscope. The resulting spectra were compared to the infrared spectrum of the corresponding neat thiol recorded through KBr windows recorded on a Perkin-Elmer Spectrum 100 FT-IR Microscope, as well as computationally generated spectra. It was also hoped that there would be diagnostic absorptions to confirm that the thiol was present as a physisorbed species rather than as a chemisorbed species. Thiols have been shown to bind to silver to form SAMs[68] via the following mechanism:[69]

$$RSH + M \rightarrow RSM + H^{+} + e^{-}(M) \ldots\ldots\ldots(12)$$

Where $e^{-}(M)$ is an electron associated with the whole metal surface, rather than an isolated metal atom. The disappearance of a thiol S-H stretching mode in the infrared spectrum is therefore an obvious place to start in order to see if the thiol had physisorbed or chemisorbed to the surface.

2.2.1 1-Dodecanethiol Infrared Spectra

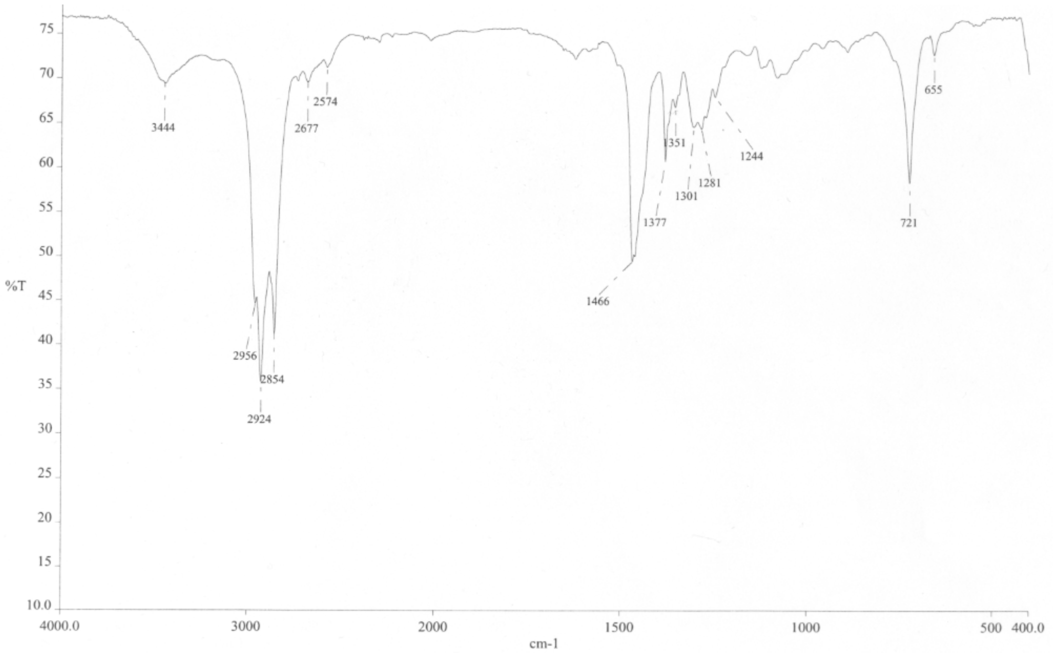

Figure 17: Infrared spectrum of 1-dodecanethiol

The S-H stretching mode of a thiol is seen in the 2550 to 2600cm^{-1} region of the infrared spectrum and is generally of weak intensity.[70] In Figure 17 a very weak absorption is seen at 2574cm^{-1} which is assigned as the S-H stretching mode. The expected C-H absorptions from the alkyl chain are observed between 2850-2960cm^{-1} for C-H stretching modes and the C-H bending modes are seen at 1466cm^{-1}.

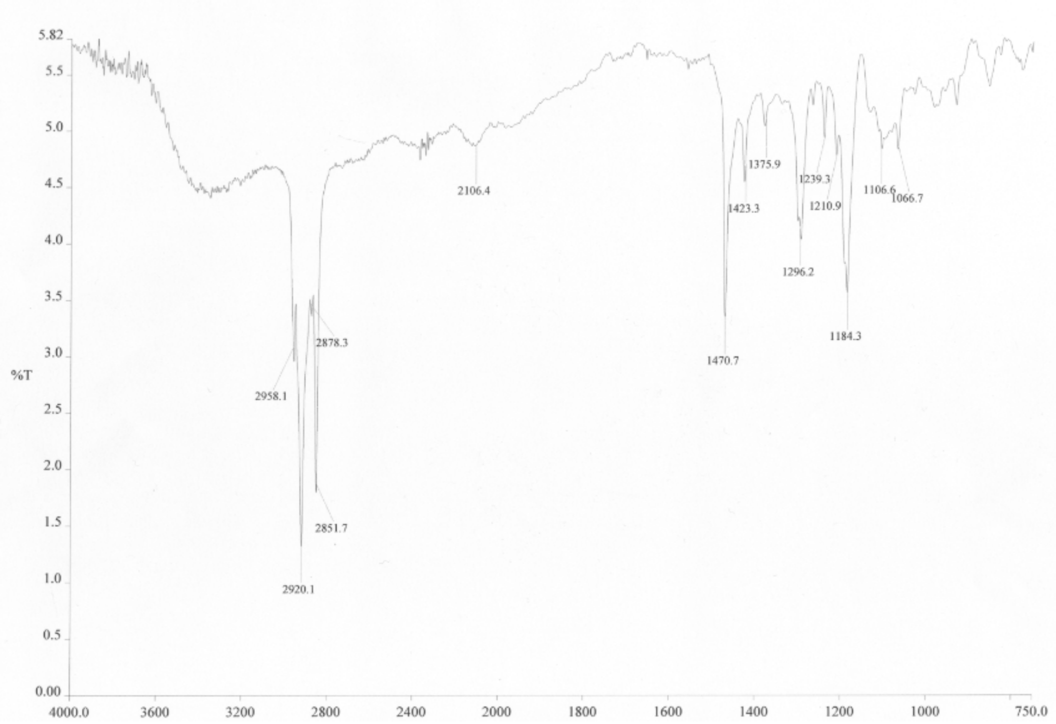

Figure 18: Infrared spectrum of superhydrophobic 1-dodecanethiol treated copper powder

Figure 18 shows many corresponding absorptions to the infrared spectrum of pure 1-dodecanethiol (Figure 17), but there is no suggestion of an absorption in the 2550-2600cm^{-1} area to which an S-H stretching mode can be attributed. The S-H stretching mode absorption of the neat thiol seen in Figure 17 was very weak, however, so the disappearance of this absorption in Figure 18, which has a much lower transmittance, is not diagnostic.

In 1987 Porter *et al*[71] investigated the variation in symmetric and asymmetric CH_2 stretching frequencies of SAMs of n-alkylthiols on gold as chain length was increased. With an increase in chain length it was found that the CH_2 stretching frequencies for the SAMs reduced from the values typically seen in the liquid thiol to approach values seen in the crystalline thiol. This is indicative of the alkyl groups packing with high degree of ordering in a monolayer. The wavenumbers of corresponding stretching modes of neat 1-dodecanethiol and the 1-dodecanethiol treated copper powder are compared in Table 1 together with the values quoted in the paper by Porter *et al*.[71]

Table 1: Characteristic infrared absorptions of alkylthiols

	Liquid C_8 thiol[71]	Crystalline C_{22} thiol[71]	Neat 1-dodecanethiol	1-dodecanethiol coated copper powder
$\nu_a(CH_3)$ cm^{-1}	2957±1	2956±1	2956±4	2958±4
$\nu_a(CH_2)$ cm^{-1}	2924±1	2918±1	2924±4	2920±4
$\nu_s(CH_2)$ cm^{-1}	2855±1	2851±1	2854±4	2851±4
$\nu(SH)$ cm^{-1}	-	-	2574±4	Not seen

Table 1 shows that any differences seen absorption frequencies between the neat 1-dodecanethiol and the 1-dodecanethiol treated copper powder are within experimental error of each other. It is therefore not possible, based on the data here, to definitively state that that the 1-dodecanethiol is chemically bonded to the surface.

2.2.2 HDFT Spectra

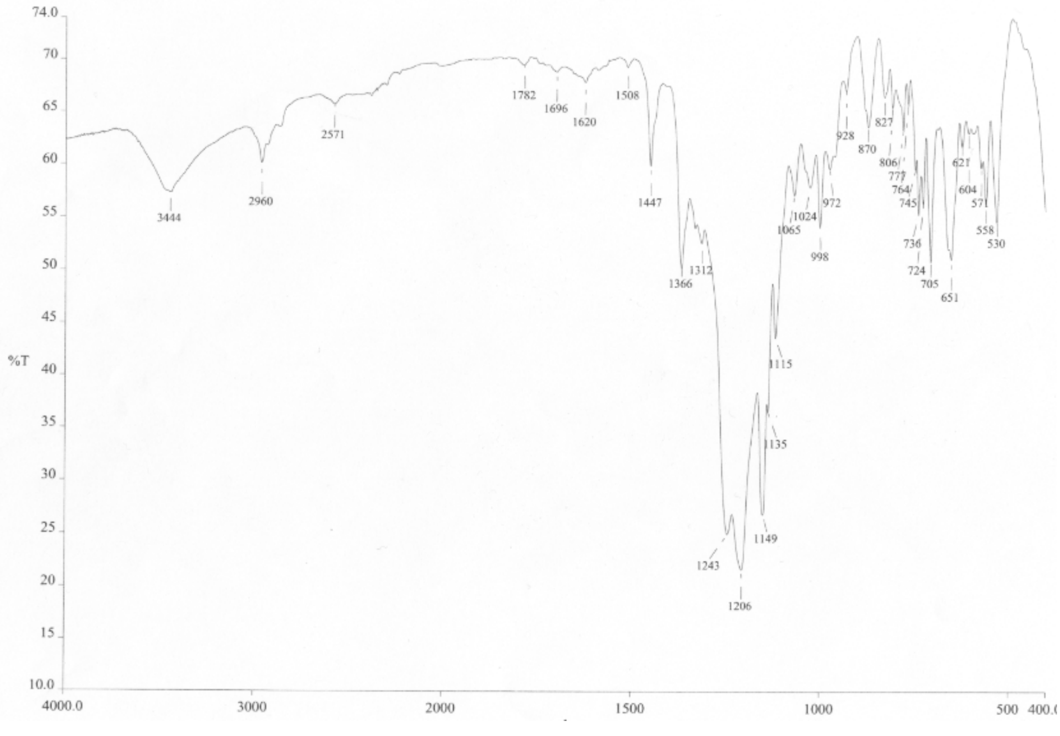

Figure 19: Infrared spectrum of HDFT

The S-H stretching mode of the thiol group is very weak but still visible at 2571cm^{-1} in Figure 19 together with relatively weak CH_2 stretching mode seen at 2960cm^{-1}. Strong absorptions from CF_2 and CF_3 vibrational modes are seen in the 1250-1150cm^{-1} range.[70] As was the case with the 1-dodecanethiol spectrum in Figure 17, the weakness of the S-H stretch of the neat thiol precludes it being a diagnostic peak when determining whether the thiol has been physisorbed or chemisorbed onto the surface of the superhydrophobic copper powder.

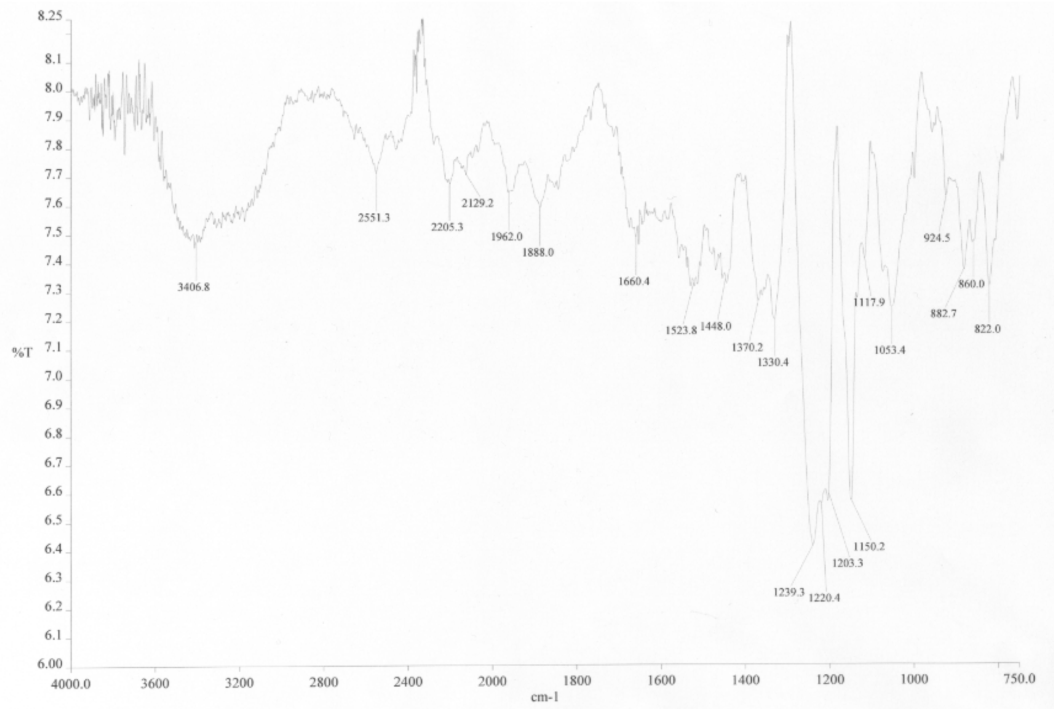

Figure 20: Infrared spectrum of superhydrophobic HDFT treated copper powder

In Figure 20 the CH_2 stretching absorptions are weakened compared to those seen in the HDFT spectrum in Figure 19 to the point that they are not discernible on the spectrum of the thiol treated copper powder. There is no absorption readily assignable to an S-H stretching mode, but CF_2 and CF_3 absorptions are readily apparent in the 1250-1150cm^{-1} range. Table 2 shows characteristic infrared absorptions of HDFT both neat, and applied to the copper powder.

Table 2: Characteristic absorptions of HDFT and HDFT treated copper powder

	Neat HDFT	HDFT treated copper powder
$\nu_a(CH_2)$ cm^{-1}	2960±4	Not seen
$\nu_a(CF_3)$ cm^{-1}	1243±4	1239±4
$\nu_a(CF_2)$ cm^{-1}	1206±4	1203±4
$\nu_s(CF_2)$ cm^{-1}	1149±4	1150±4
$\nu(SH)$ cm^{-1}	2571±4	Not seen

All of the corresponding absorptions seen are within experimental error of one another, so it is once again not possible to determine the method of sorption of the thiol based on the data presented here.

2.2.3 Computational Studies of Thiols and Silver-Thiolate Complexes

Computational studies were carried out using Gaussian 09[72] on the University of Waikato Symphony supercomputer. Input matrices were constructed using Gaussview 5.0.8 and density functional calculations were carried out using the B3LYP method and 6-31G+(d,p) basis sets for carbon, hydrogen, fluorine and sulfur. All structures were optimised using the Berny[73] routine while initially constrained to Cs symmetry, and frequency calculations were carried out on the optimised structures to ensure that the resulting structures were minima and not transition states.

The resulting structures then had carbon-carbon dihedral bond angles along the chain perturbed by *ca* 5^0 and the structure was optimised once again without constraint to Cs symmetry. The energies of the resulting structures were then compared and the lowest energy structure was used as the optimised structure. Calculations were performed on isolated structures with no solvation model.

To model the silver thiolate complex, the optimised free thiol structures were used as a base template with the thiol hydrogen atom replaced by a silver atom. This complex was treated as neutral, since the electron oxidised from the thiol is associated with the bulk metal surface (Equation 12). The silver thiolate complex was then optimised and frequency calculations carried out.

In order to keep the tasks computationally tractable, an effective core potential was used for silver, which was described by the LANL2DZ basis set and the chain lengths of the modelled thiols were restricted to six carbons long.

2.2.3.1 1-Hexanethiol Spectra

The optimised structure of 1-hexanethiol was found to be of Cs symmetry and in an *anti* configuration, and so too did the silver-thiolate structure (Figure 21).

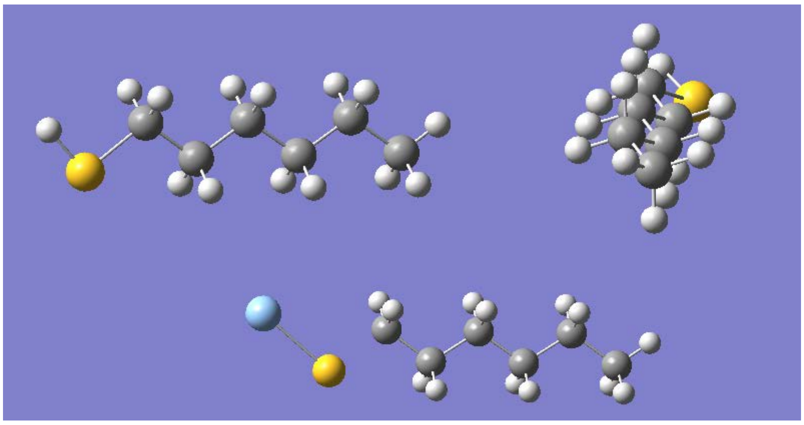

Figure 21: Optimised structures of 1-hexanethiol (top); silver-hexanethiolate complex (bottom centre)

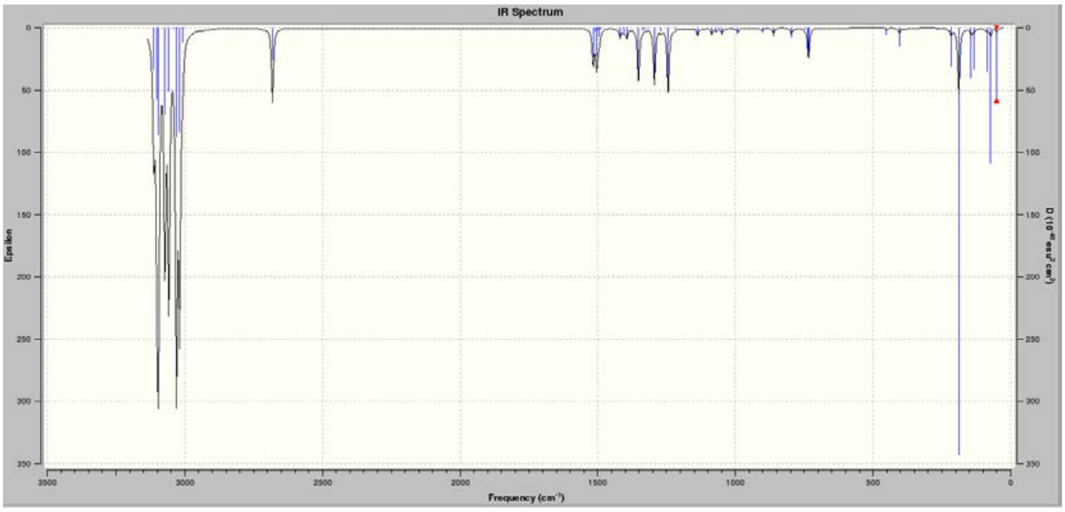

Figure 22: Computed infrared spectrum of 1-hexanethiol

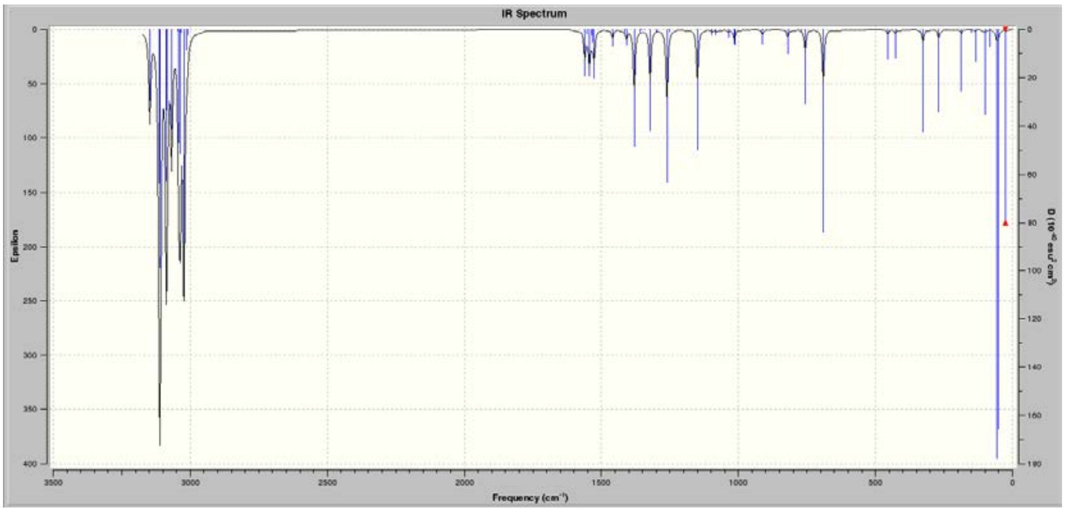

Figure 23: Computed infrared spectrum of 1-hexanethiolate-silver complex

The computed spectrum of free 1-hexanethiol (Figure 22) shows the S-H stretching mode at 2680cm^{-1} which is not present in the computed spectrum of the corresponding silver-thiolate complex (Figure 23). This absorption in the experimental spectrum was too weak to be diagnostic, however. The frequency of the calculated S-H stretching mode is significantly higher than the corresponding experimentally observed absorption of 2574cm^{-1}, but this is to be expected, as the computational model utilised uses the simple harmonic oscillator approximation for vibrational calculations, which overestimates stretching frequencies.

The most striking difference between the two spectra is the appearance of the peak at 690cm^{-1} on binding to silver (Figure 23) which is due to a C-S stretching mode. The corresponding absorption occurs at 735cm^{-1} in the free thiol's calculated spectrum, but is much weaker than the absorption seen in its silver-bound counterpart. The experimentally recorded infrared spectrum of the 1-dodecanethiol treated copper powder does not extend to below 750cm^{-1} so the computed peak at 690cm^{-1} will not be seen, particularly considering the experimental vibration will be at a still lower frequency due to the simple harmonic oscillator approximation used.

2.2.3.2 1H,1H,2H,2H-perfluorohexanethiol Spectra

Optimising the structure with constraint to Cs symmetry resulted in a transition state structure which was shown by the presence of an imaginary frequency in the computed spectrum. Optimisation after offsetting the dihedral angles between carbons down the length of the chain by 5° and removal of constraint to Cs symmetry resulted in the structure seen in Figure 24. There is a helical nature to the structure down the length of the carbon chain which relieves 1-3 fluorine-fluorine interactions. This is consistent with the fact that 1-3 eclipsed interactions between fluorine atoms are repulsive, while vicinal fluorine atoms are attracted to one another,[74] so repulsive interactions are minimised and attractive interactions are maximised in this configuration. The helical nature of the fluoroalkyl chain was maintained in the optimised structure of the silver-thiolate complex also.

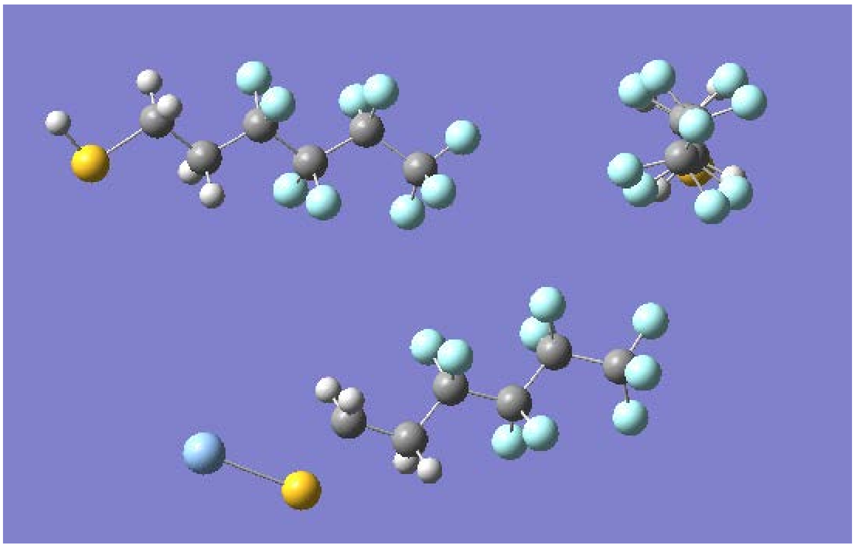

Figure 24: Optimised structures of 1H,1H,2H,2H-pefluorohexanethiol (top); silver-thiolate complex (bottom centre)

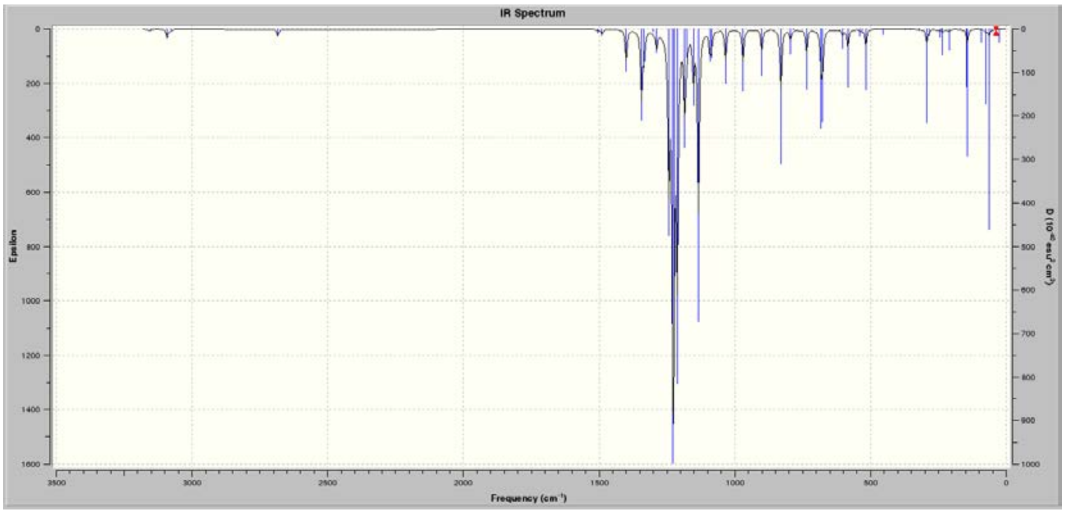

Figure 25: Computed infrared spectrum of 1H,1H,2H,2H-pefluorohexanethiol

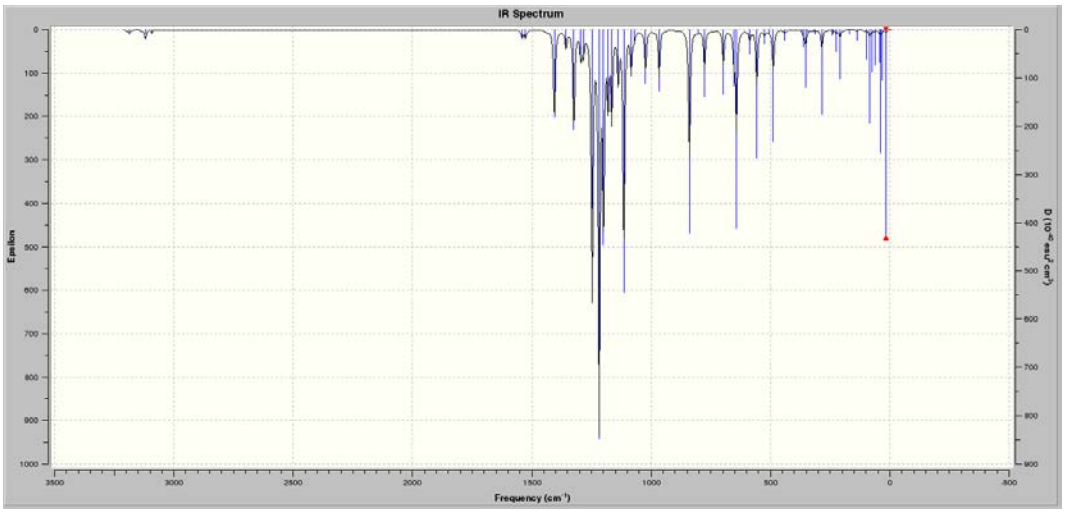

Figure 26: Computed infrared spectrum of silver-thiolate complex

There does not look to be a diagnostic difference between the two calculated spectra in Figure 25 and Figure 26 apart from the loss of the S-H stretching absorption which is very weak at 2681cm^{-1} once the silver-thiolate complex has been formed. However, the corresponding absorptions for S-H stretching modes in the experimental spectra were deemed too weak to be of diagnostic use.

Unfortunately after this investigation it seems that infrared spectroscopy is only able to confirm the presence of the alkyl or fluoroalkyl portions of the thiols on the superhydrophobic copper powder, rather than differentiate between physisorbed and chemisorbed states.

2.3 Effect of Pressure on Superhydrophobicity on Cold-Formed Materials

The 2010 paper on ecdysiastic superhydrophobic materials by Larmour *et al*[65] reported compressing superhydrophobic copper powder at three different pressures, and it was seen that the WCA and roll-off angles of the resulting compacts were affected by varying the compression pressure (Table 3).

Table 3: Larmour *et al*'s[65] results for ecdysiastic superhydrophobic materials

Pressure (MPa)	Density (gcm^{-3})	Treatment	Roll-off angle (Degrees)	WCA (Degrees)
7.5	4.7	Abraded x1	4.2±1.1	150.3±0.8
18.8	5.6	Abraded x1	6.4±0.6	162.9±1.0
		Abraded x2	6.3±1.1	162.2±1.4
		Abraded x3	5.5±2.4	162.0±1.3
37.5	6.6	Abraded x1	36.5±5.8	132.7±1.4

An error made when calculating compression pressures resulted in quoted pressure values being a factor of ten lower than they should be in this work, so the compression values reported in Table 3 should be 75, 188 and 375MPa respectively. The compression procedures were carried out on a hydraulic press, and hydraulic presses are known to be prone to inaccuracy when calculating the pressure to which a compact is subjected. A deeper study on the effect of compression pressure on the superhydrophobicity is carried out here using accurate, specialised equipment over a large number of compression values in an effort to find the optimum compression conditions for a suitable compromise between disk strength and superhydrophobicity.

2.3.1 Compression Procedure for Cold-Forming of Disks

Approximately 1.5 to 2 grams of 1-dodecanethiol treated, silver coated copper powder from section 2.1.1 was loaded into a SPECAC 13mm evacuable pellet die. The die was then compressed to the desired pressure in a Lloyd LR30K Plus Materials Testing Machine using the "Creep Test" programming in the accompanying "Lloyd Nexygen Plus" software.

Pressures ranging from 20MPa to 180MPa were assessed. The powder was initially compressed for ten seconds at 3.75MPa below the target compression pressure followed by a two minute compression at the desired pressure. Once prepared, the disks were carefully removed from the die.

A typical force versus time profile obtained for a two minute compression is given in Figure 27. When calculating the pressure that a disk was subjected to, the value for applied force used was taken from the central plateau region of the profile rather than the peak value seen at the beginning of the profile.

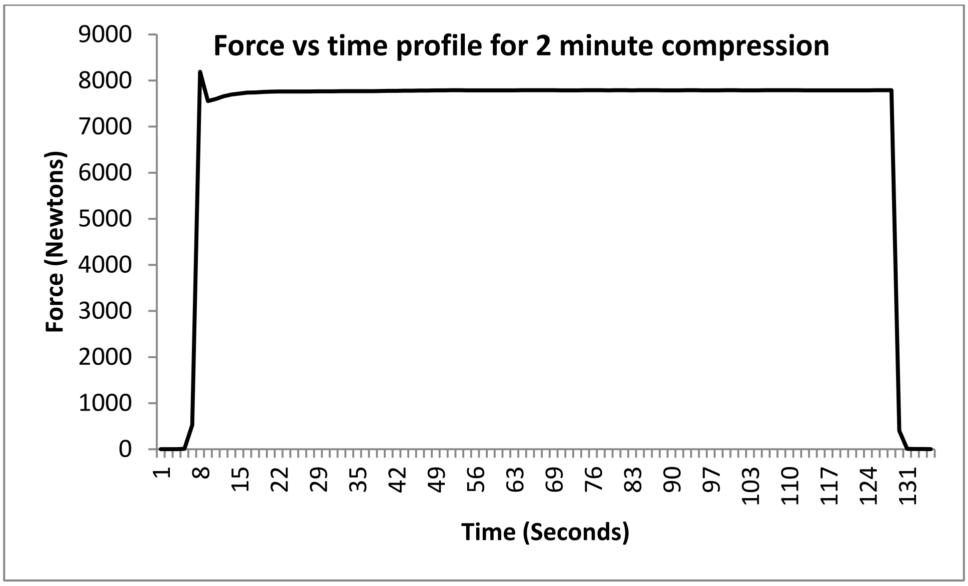

Figure 27: Typical compression profile for two minute disk compression

2.3.2 Effect of Compression Pressure on Ecdysiastic Materials

Roll-off angle values were used to quantify the superhydrophobicity of the resulting materials. A roll-off angle measuring device was constructed from two lengths of timber held together with a hinge at one end. Two rulers were glued 900mm apart on the bottom piece of timber, perpendicular to the length of it (Figure 28).

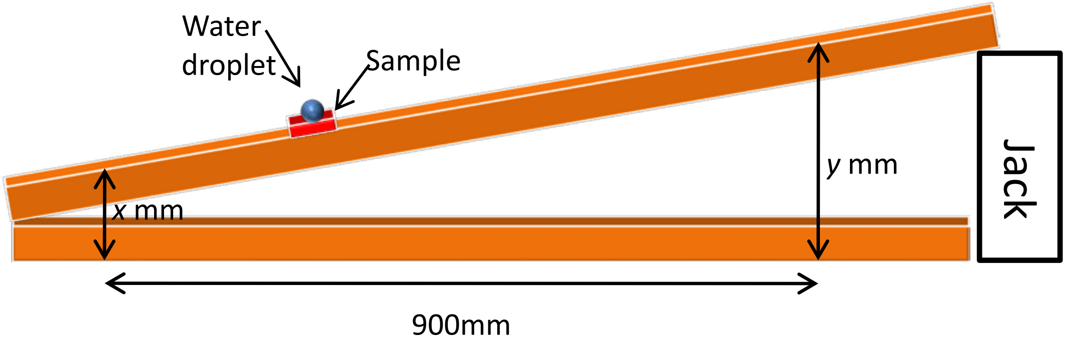

Figure 28: Schematic of roll-off angle measuring device

Disks were placed onto the upper platform of the roll-off angle measuring device and secured in position by double sided adhesive tape. The smooth layer at the surface of each newly compressed disk was filed off to expose a fresh layer beneath. Excess filed off powder was gently blown away from the freshly exposed layer, and a 20μL droplet of distilled water was applied using an autopipette. The angle of the platform the disk was on was gently increased using a lab jack until the water droplet rolled off the disk. Care was taken to avoid any sudden motions while increasing this angle in order to ensure that the droplet rolled due to the influence of the force exerted on the drop due to gravity, rather than being shaken off the disk. The height of the top of the platform at front and rear was read, and from there the angle can easily be calculated using trigonometry.

This procedure to measure a roll-off angle was repeated five times, the disk turned 180° and five more trials were run so as to cancel out any bias from uneven filing of the disk. Each disk was filed again to a depth of *ca* 1mm to expose a fresh surface and tested in the same fashion as above to prove the ecdysiastic nature of the disks. Each disk was subject to a total of three filings and thirty roll-off angle measurements, unless the disk broke during testing.

The results for roll-off angles for each fresh surface exposed on each disk (three readings for each disk, unless broken) were then averaged and 95% confidence intervals calculated to give an estimate of error in the measurement. Results for the roll-off angle trials are summarised in Figure 29 and Figure 30.

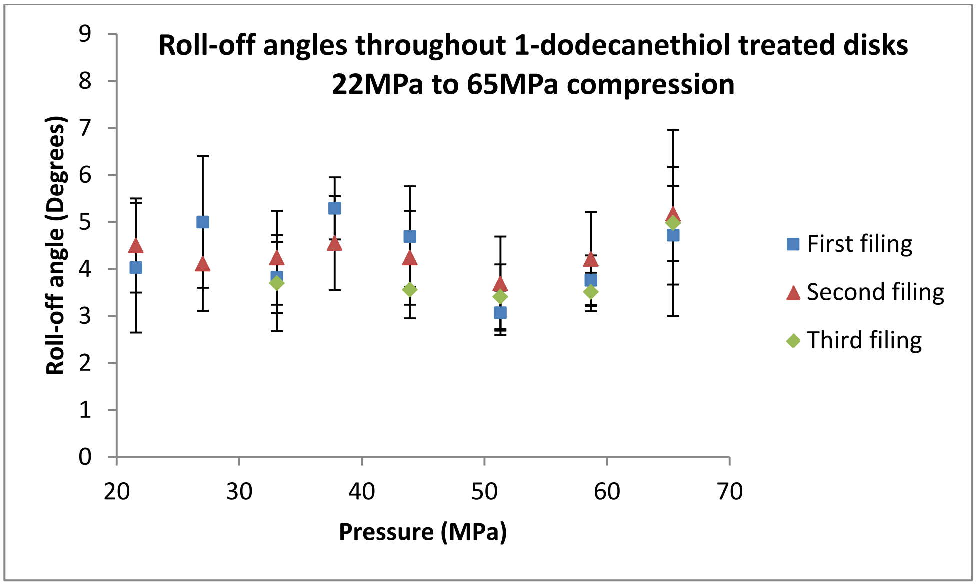

Figure 29: Roll-off angles throughout superhydrophobic copper disks compressed from 22MPa to 65MPa

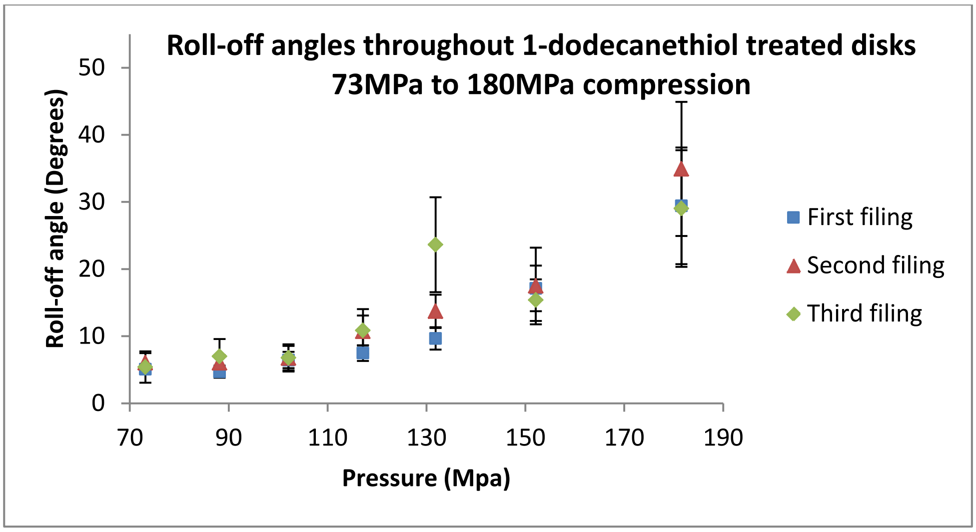

Figure 30: Roll-off angles throughout superhydrophobic copper disks compressed from 73MPa to 181MPa

The results demonstrate that roll-off angle remains constant within experimental error as one files their way through the disk (Figure 29, Figure 30), which confirms the ecdysiastic nature of the material. There does, however, appear to be an anomalous result for the disk compressed at 130MPa, though this is only one inconsistent trial from 42 in total. Using 95% confidence intervals, one time in twenty there will be a statistically significant difference picked up in a population where no difference exists,[75] so this observation is to be expected over 42 trials.

All thirty roll-off angle results for each disk of a given pressure were then treated as one data set, rather than three, to calculate an overall roll-off angle for each disk. This treatment gives a larger data set and a smaller error for each disk and the resulting data can be used to give an insight on how roll-off angle varies with compression pressure (Figure 31).

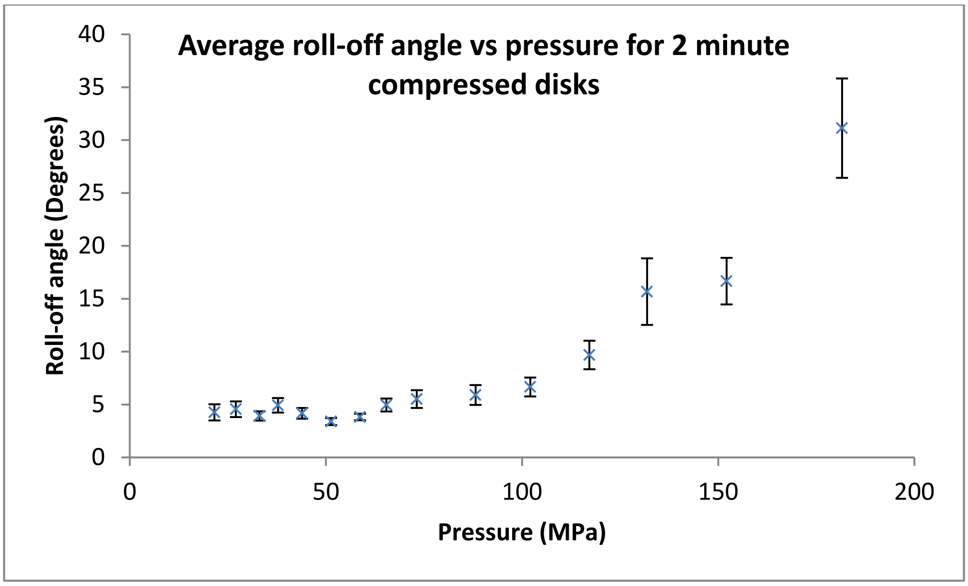

Figure 31: Variation in roll-off angle with pressure for two minute compressed disks

The results reveal the trend that as pressure increases past 59MPa the roll-off angle and associated error slowly increase. Once a pressure of 100MPa is reached the increase in roll-off angle with pressure becomes more pronounced. Numerical data for the roll-off angle trials can be found in Appendix One.

The 180MPa compressed disk prepared here has the same roll-off of 31±5°which is within experimental error of the roll-off angle of Larmour's 375MPa disk compressed on a hydraulic press (Table 3). The reported compression pressures for materials of similar wetting characteristics are of the same order of magnitude, and perhaps the difference in calculated pressures can be attributed to inaccuracies associated with the use of the hydraulic press in Larmour's preceding work.

2.3.2.1 Distribution of Roll-off Angles

The results for roll-off angles recorded throughout each disk were normalised into z-scores[75] to ensure that the measurements followed a normal distribution:

$$z = \frac{x - \mu}{\sigma} \dots\dots\dots (13)$$

Where x is the observed data point value, μ is the population mean and σ is the standard deviation. The data population that results has a mean of zero and a standard deviation of one. The resulting z-score data for each disk compressed to a different pressure was plotted into a histogram (Appendix 2) and inspected to see if it follows a normal distribution shape to confirm that the 95% confidence interval error treatment is appropriate.

The histograms generally followed the normal distribution reasonably well, although they tended to show a slight skew to the right. A typical example is seen in Figure 32 which shows data for the disk compressed at 44MPa.

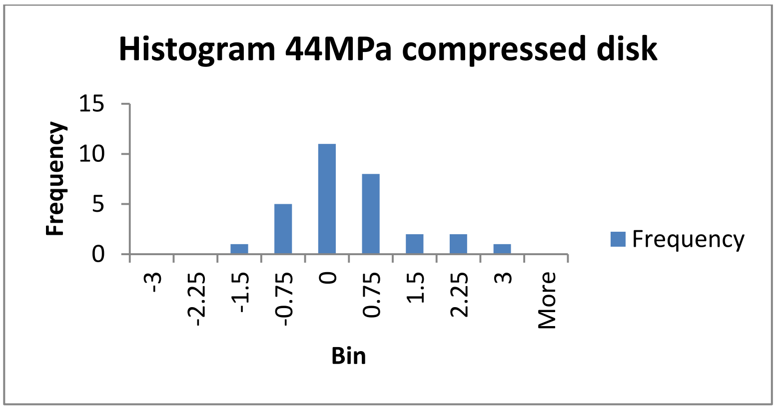

Figure 32: Histogram of z-scores for 44MPa compressed disk

As compression pressure was increased the asymmetry of the distributions tended to increase, to the point that some of the distributions almost appeared to become multi-modal. This is best seen in the disk that was compressed at 150MPa (Figure 33).

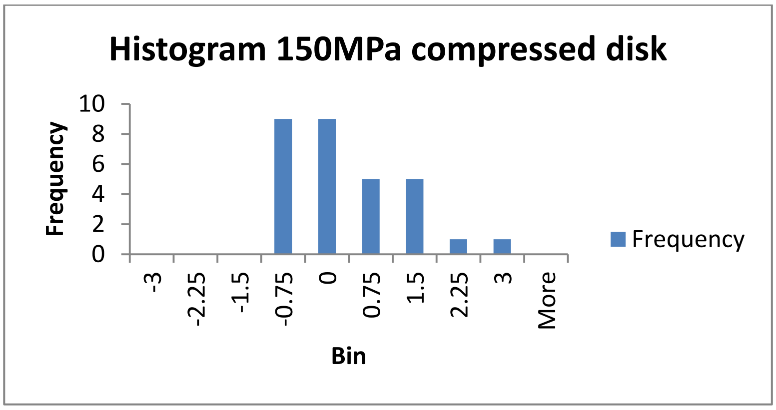

Figure 33: Histogram of z-scores for 150MPa compressed disks

This may be indicative of more than one type of surface being present on the disk, each of which can have its own roll-off angle value and associated error. This scenario would give rise to quite different roll-off angle values depending on where a water droplet is placed on the disk for a test.

2.3.2.2 Investigation of Water Contact Angle Variation with Compression Pressure

A selection of the copper disks had static WCA values recorded to see how this property varied with pressure. The disks chosen included one compressed at 33MPa, one at 59MPa pressure and one at the highest attained pressure of 180MPa. All WCA measurements were recorded at The University of Auckland. A water droplet approximately 1mm in diameter was placed onto the disk, and the WCA on either side (left and right) of the water droplet was measured 20 times. This process was repeated three times for each disk, each time with a fresh water droplet placed on a different area on the disk. 95% confidence intervals were constructed for all measurements to give an estimate of uncertainty.

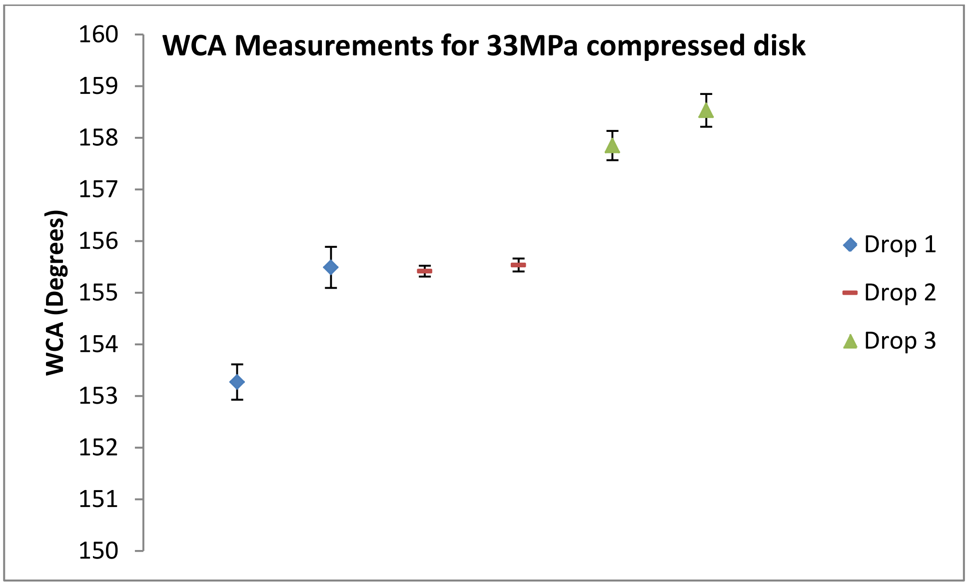

Figure 34: WCA measurements for 33MPa compressed disk

The WCAs seen in Figure 34 are all above the 150˚ threshold for a surface to be deemed superhydrophobic, but they are not all consistent with one another at the 95% confidence level. The data for the first droplet also indicate that there is a different WCA for each side of the drop.

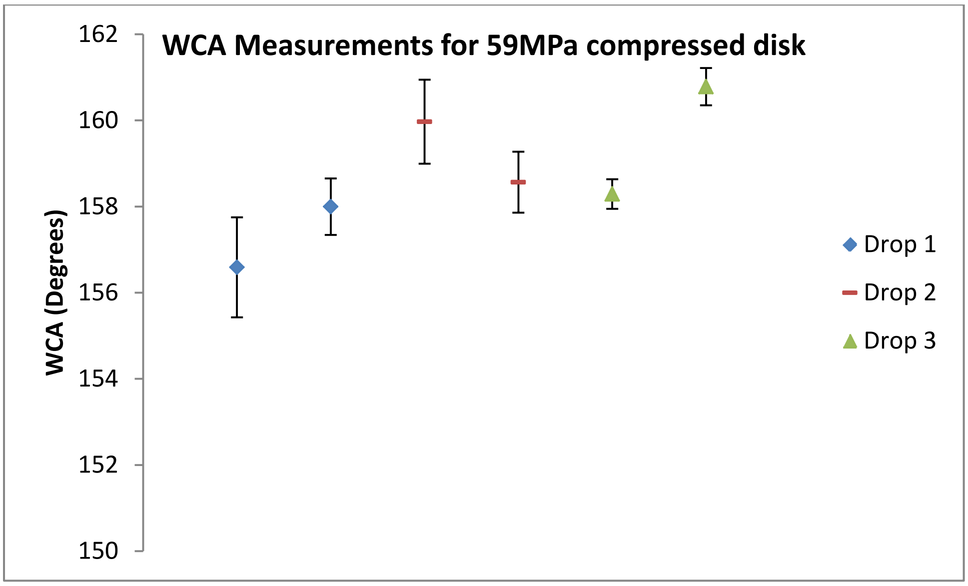

Figure 35: WCA measurements for 59MPa compressed disk

The WCAs seen in Figure 35 for the disk compressed at 59MPa look to be very similar in value and behaviour to those seen for the 33MPa compressed disk. This is consistent with the data obtained for the roll-off angles of the two disks, as they were both the same within experimental error (Table 4).

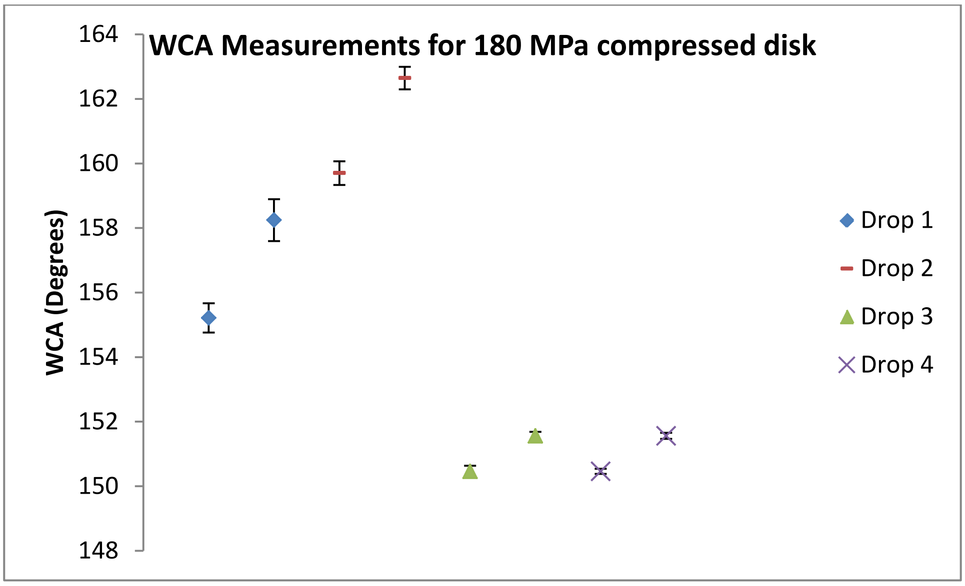

Figure 36: WCA measurements for 180MPa compressed disk

The WCAs seen for the 180MPa compressed disk (Figure 36) are surprising in that they appear to be very similar in value to those seen on the 33MPa and 59MPa compressed disks. WCAs for a fourth water droplet were even measured to ensure that the results were not anomalous. The roll-off angle of the 180MPa compressed disks is markedly higher than that seen on the disks prepared at lower the compression pressures (Table 4), so perhaps it could be expected that there would be a difference in WCA between this disk and the others compressed at lower pressure.

What does stand out is that every one of the droplets measured in Figure 36 shows an asymmetry in their WCA measured either side, and there appears to be a larger range in contact angle. This may imply that there is some pinning at the three phase interface as the drop is placed on the surface and as a result the water spreads unevenly. If there is pinning of the three phase contact line for all of the measurements taken, it may be indicative of the surface having a large contact angle hysteresis, which contributes to a large roll-off angle (Equation 11).

To directly compare WCAs of the three disks it was decided that since the WCAs tend to be different across each disk, a 95% confidence interval would be inappropriate. To compare, a range is given which is centred between the edges of the highest and lowest confidence intervals for WCAs of each disk. The results are summarised in Figure 37.

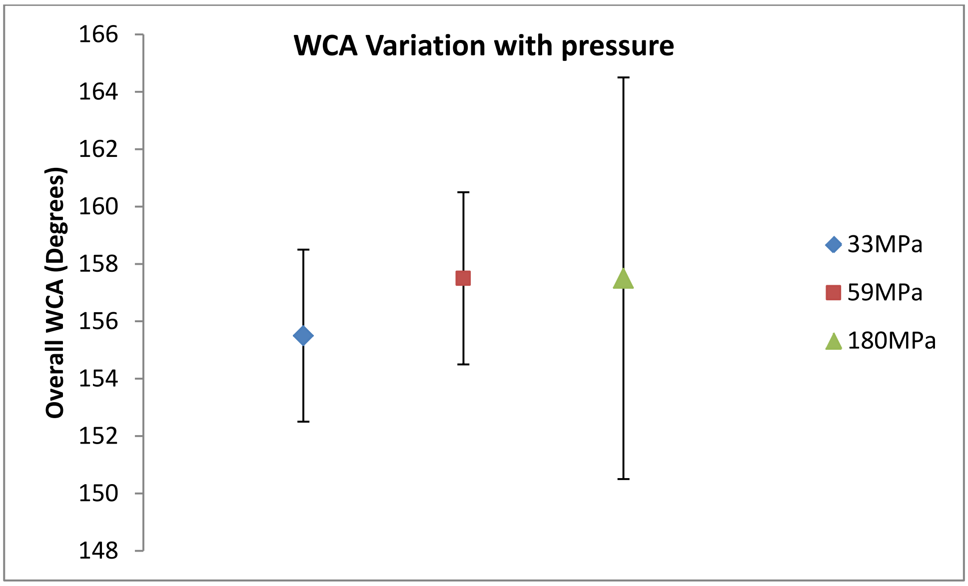

Figure 37: Comparison of WCAs for disks compressed at different pressures.

The overall WCAs seen in Figure 37 of all of the disks tested here are within experimental error of one another, which was not the case for the roll off angles (Table 4).

Table 4: Roll-off angle and WCA comparison for disks prepared at different pressures

Compression pressure (MPa)	Roll-off angle (Degrees)	WCA (Degrees)
33	3.9±0.4	156±3
59	3.8±0.3	158±3
180	31±5	158±7

From this it can be seen that the reporting of a single static WCA does not fully describe the wetting characteristics of these surfaces, and roll-off angle values give more insight into the wetting behaviours of the materials. This lack of variation in contact angle with pressure is inconsistent with what was seen in Larmour's work,[65] although WCA data was only recorded on compacts compressed to three different pressures in both sets of work. A complete study on WCA variation with pressure including measurement of advancing and receding WCAs on these surfaces could go some way to explaining this observation.

2.3.3 SEM Investigations of Ecdysiastic Materials

SEM images of the disks prepared at various pressures were recorded. Since the texture of a surface is so important with regards to its wetting behaviour, and wetting behaviour was seen to change with pressure through changing roll-off angles, it was hoped to gain an insight into any differences in morphology that may arise as pressure is increased. All SEM Images were recorded on a Hitachi S-4700 FE-SEM Scanning Electron Microscope at 20kV accelerating voltage.

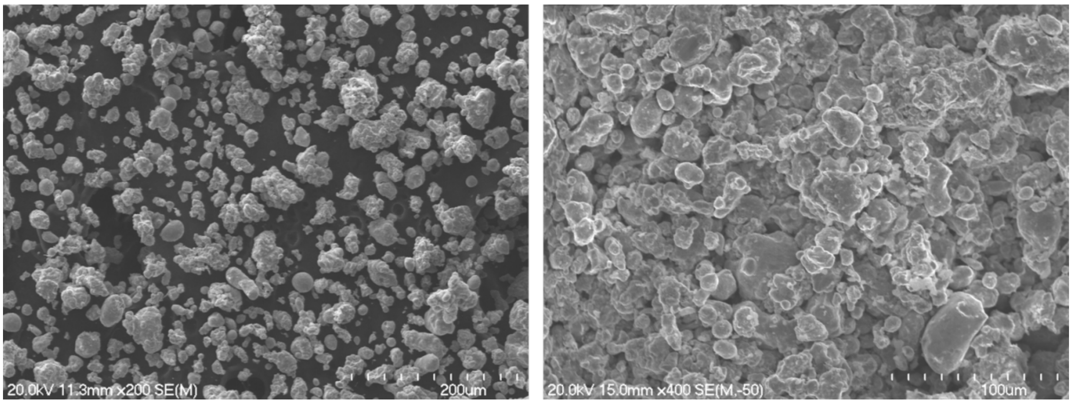

Figure 38: Superhydrophobic copper powder (left); 59MPa compressed disk (right)

Figure 38 shows uncompressed superhydrophobic copper powder and a freshly abraded surface of a 59MPa compressed superhydrophobic copper disk. The powder is irregular in shape and of a size range of 5-50µm across. When compressed into a disk, a high degree of mechanical interlocking is seen between powder particles.

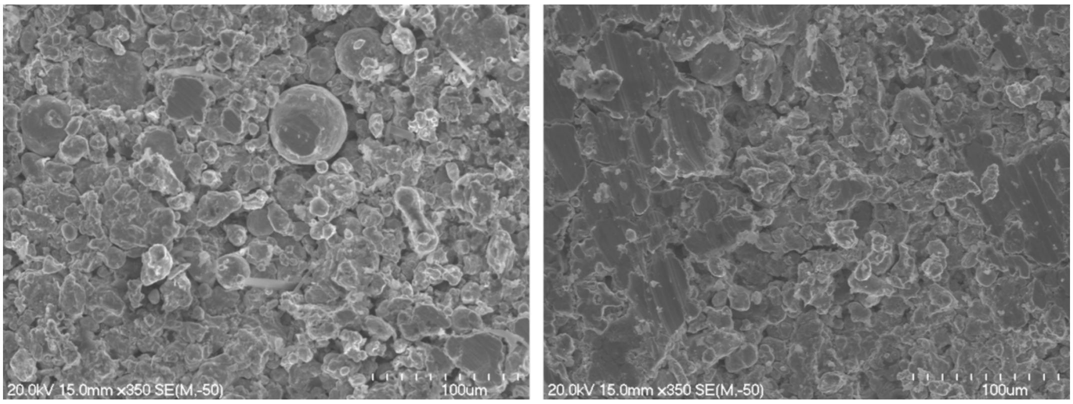

Figure 39: SEM images of 150MPa compressed disk (left); 180MPa compressed disk (right)

As pressure is increased to 150MPa, flat spots began to appear on the surface where the abrasion has occurred, and the effect becomes more prominent as pressure is increased to 180MPa (Figure 39). Even to the naked eye, copper coloured streaks could be seen on the disks prepared at high pressure when filed to expose a new surface.

It seems that at 59MPa pressure the disks can hold together well, but still freely allow the release of damaged particles during the abrasion process. When pressure is increased to 150MPa and 180MPa the powder particles are compressed to the point where the release of damaged particles is prevented from happening and these are retained and smeared by the abrasion process, exposing bare, untreated copper. Water droplets placed onto this surface can become pinned on these exposed untreated copper heterogeneities to give rise to the larger roll-off angles seen, as well as larger error margins in roll-off angle.

These heterogeneities may also go a way towards explaining the distributions of the roll-off angles of the compressed disks tending to become more skewed and even multi-modal with increased pressure also. The image of the 150MPa compressed disk in Figure 39 shows a relatively low concentration of these flattened features so it could be conceivable that a water droplet can become lodged on these flattened areas which will give one range of roll-off angle values, or it could predominantly be on the highly textured surface which escaped being damaged in the abrasion process. Each of these areas would have their own roll-off angle and associated error which would manifest itself as a multimodal distribution.

2.4 Effect of Compression Time on Superhydrophobicity

The effect of compression time on the both the superhydrophobicity and the ecdysiastic character of the prepared materials was also investigated. A series of disks was prepared at varying compression pressures as had been done with the disks prepared in Section 2.3.1, but these disks were subjected to a compression time of ten seconds rather than two minutes. There was no pre-compression procedure for the disks compressed for ten seconds.

A typical compression profile for force applied over time for a ten second compression routine is shown in Figure 40. The force shown in the central plateau region of the compression profile was used when calculating the pressure the disk was subjected to.

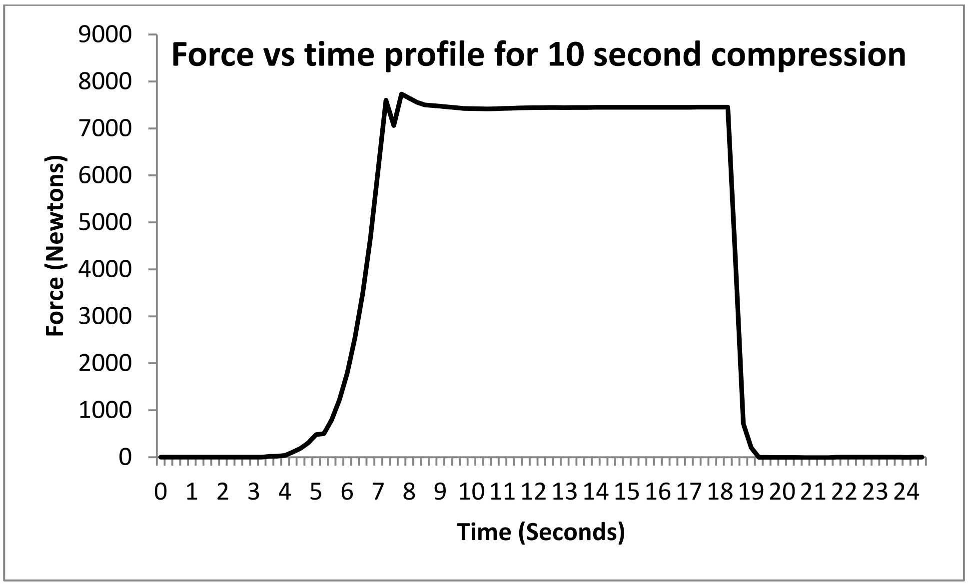

Figure 40: Compression profile for 10 second compression routine

The same roll-off angle measurement routine that is described in Section 2.3.2 was performed on all of these disks that were compressed for 10 seconds. Qualitatively, the disks that had been prepared using the shorter compression time of 10 seconds were far more fragile and friable than those that had been compressed for two minutes. The results of the roll-off angle trials to confirm the ecdysiastic nature of the disks are shown in Figure 41 and Figure 42.

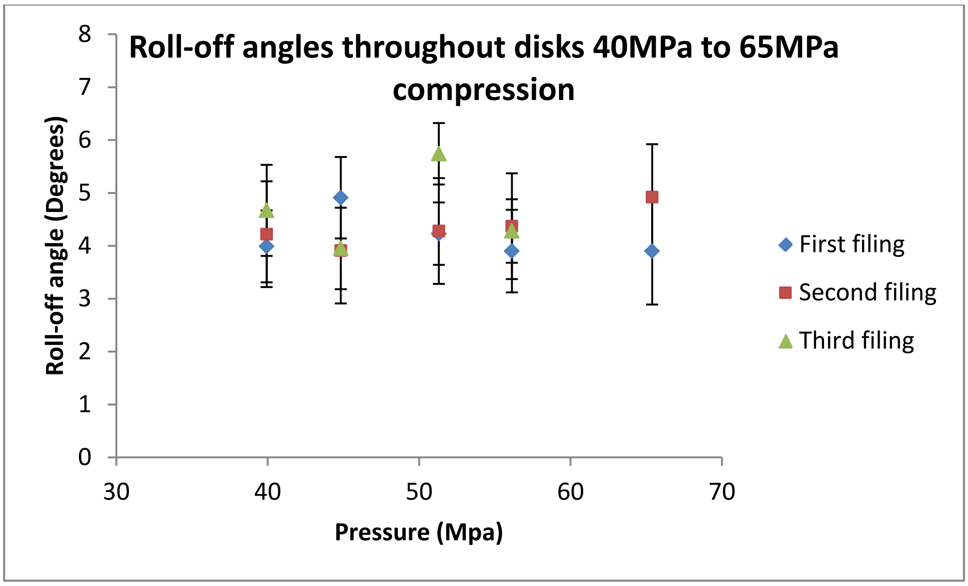

Figure 41: Roll-off angles throughout superhydrophobic copper disks compressed from 40MPa to 65MPa for 10 seconds

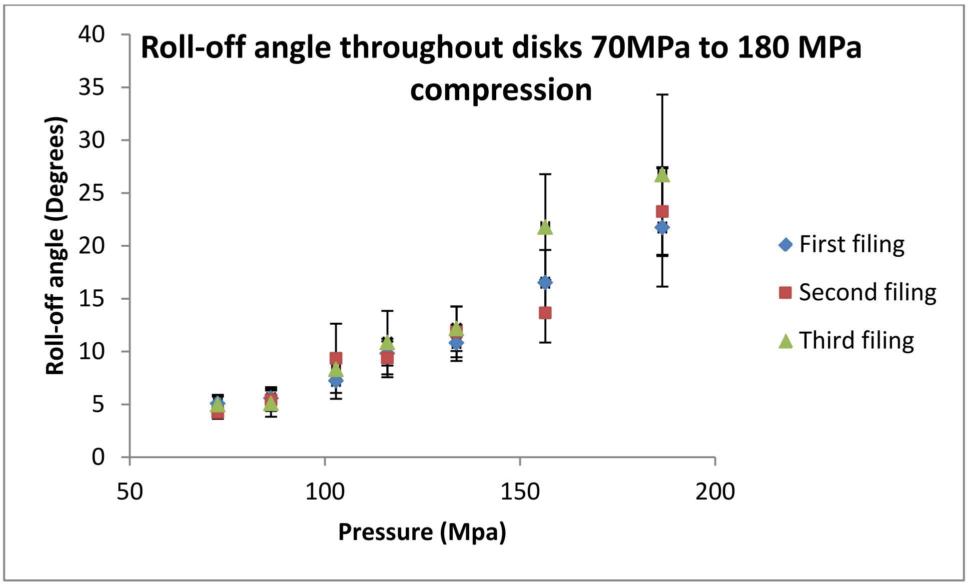

Figure 42: Roll-off angles throughout superhydrophobic copper disks compressed from 70MPa to 180MPa

The ecdysiastic nature of the material has been confirmed by reproducible roll-off angles for each fresh surface exposed after filing (Figure 41, Figure 42). This indicates that the reduction in compression time from two minutes to ten seconds has not influenced this aspect of the material.

In order to ascertain whether of the roll-off angle increases with an increase in compression pressure, as was the case with the disks compressed for two minutes, all thirty roll-off angle results recorded throughout each disk were pooled together to give an overall roll-off angle for each disk as was done in Section 2.3.2. The results of this data treatment are summarised in Figure 43, and clearly show that the shorter compression time has not changed the trend of a larger roll-off angle corresponding with increased compression pressure. Also consistent with the disks that were compressed for two minutes is a fairly consistent roll-off angle range until a force of *ca* 100MPa is reached after which roll-off angle steadily increases with pressure. Numerical data for these roll-off angle trials can be found in Appendix Three.

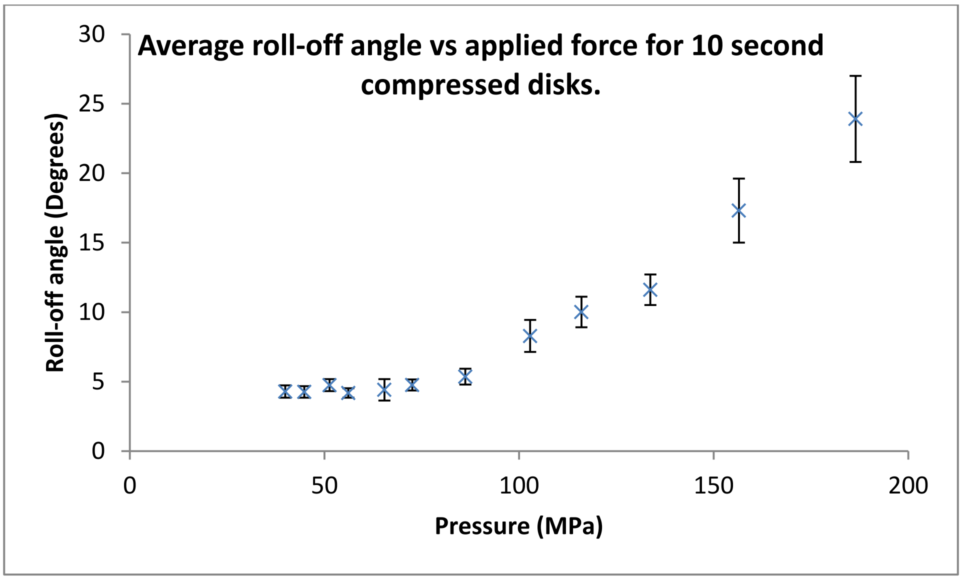

Figure 43: Variation in roll-off angle with pressure for 10 second compressed disks

2.4.1.1 Comparison of Roll-off Angle Values Between Different Compression Times

The overall values of roll-off angles for the two different compression times at varying pressures are compared in Figure 44 below.

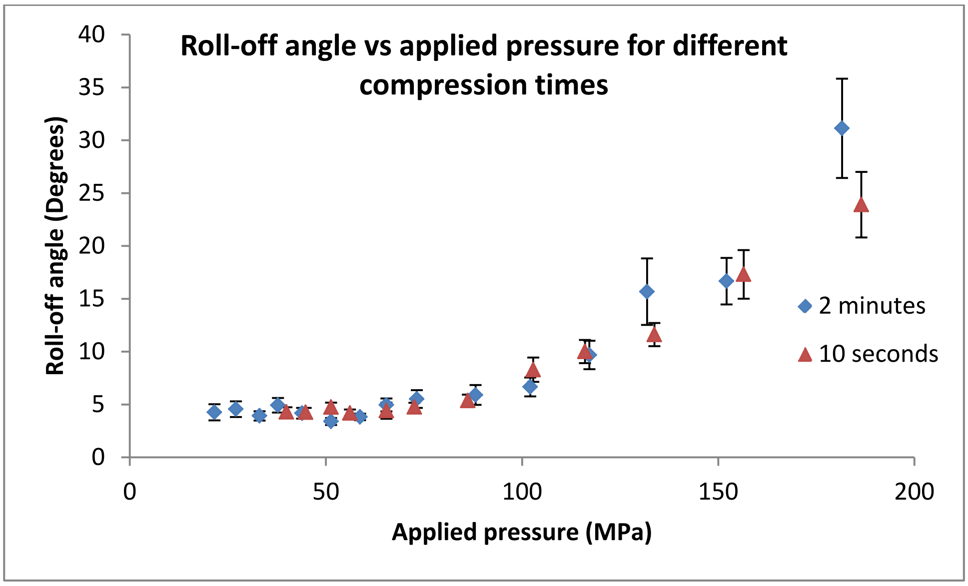

Figure 44: Roll-off angles for 2 minute compressed disks and 10 second compressed disks

Compression time appears not to have an effect on the roll-off angle values of the ecdysiastic materials in the range of compressions tested. To further ensure that compression time was not a factor in determining roll-off angle, a disk was prepared by compressing for 20 minutes at 59MPa and both the ecdysiastic character and overall roll-off angle were compared with the disks compressed to the same pressure for 10 seconds and for two minutes.

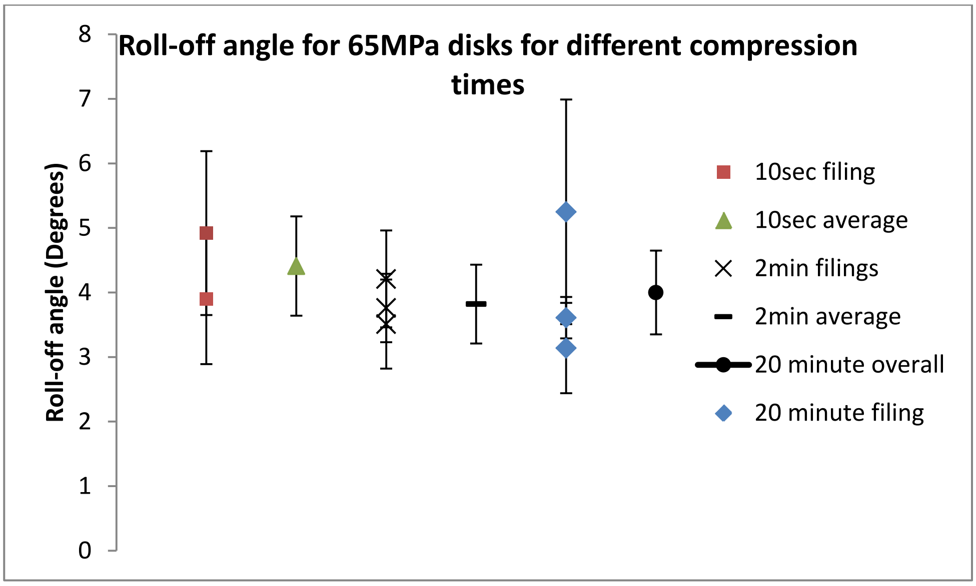

Figure 45: Roll-off angles for disks compressed to 65MPa for different lengths of time

Figure 45 demonstrates that there is no statistically significant difference amongst the average roll-off angles for the three different compression times and all showed uniform roll-off angles throughout. The disks which had the shorter compression time of ten seconds were more fragile and difficult to handle than those prepared at two minute or 20 minute compression times. Figure 45 also shows that only two roll-off angle measurements were obtained for the disk compressed to ten seconds; it broke before a third trial was able to be completed.

A two minute compression time at a pressure of 59MPa was settled on as a suitable compromise between the disk having a low roll-off angle of 3.8±0.3˚, reasonable disk strength and convenient preparation time.

2.5 Effect of Compression Pressure on Disk Density

The mass and dimensions of all of the disks were recorded as soon as they were prepared. Disk diameters and heights were measured using vernier calipers and volumes of the disks were calculated assuming the disks adopted a perfectly cylindrical form.

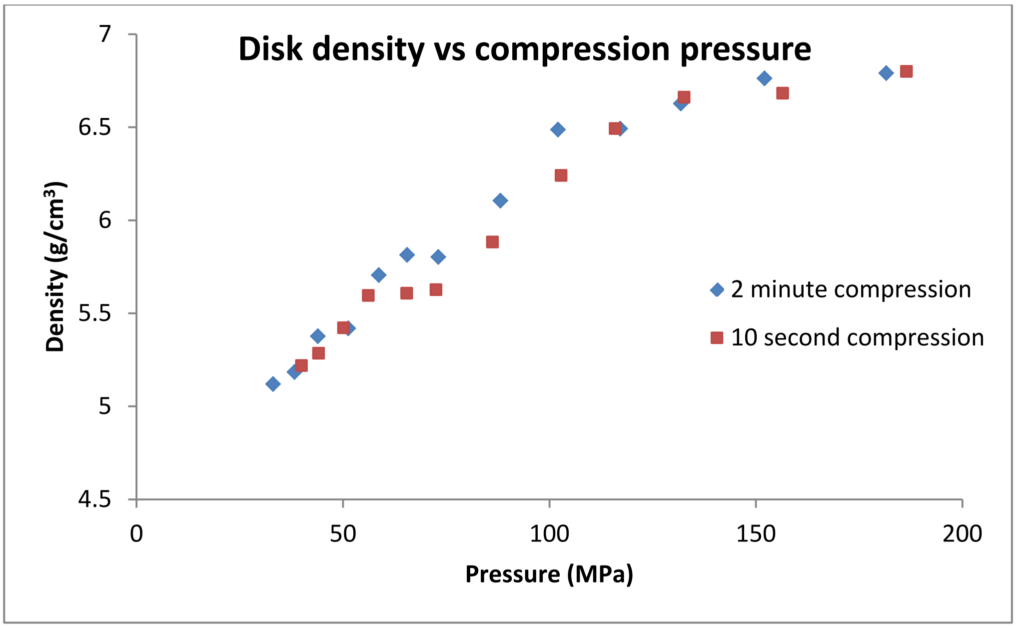

Figure 46: Variation of density with applied pressure for two minute compression and 10 second compression

As can be reasonably expected, Figure 46 shows that disk density increases with applied pressure. Disk densities were found to range from 5.12gcm^{-3} to 6.80gcm^{-3}. By comparison, pure copper has a density of 8.96gcm^{-3}.[76] The two different compression times are seen to have very similar profiles on the graph together with very similar values also.

The significantly lower density values of the disks compared to solid copper indicate that they are of a porous nature. If untreated copper powder is compressed in the same way as the superhydrophobic copper is to form a disk, it absorbs an applied water droplet, which further confirms the porosity of the disks.

The graph in Figure 46, particularly for the 2 minute compression data, shows a linear increase in density with pressure until a pressure of 100MPa has been reached. After that point, the trend of density increasing with applied pressure tapers off markedly. A closer look at this linear portion of the graph is shown in Figure 47.

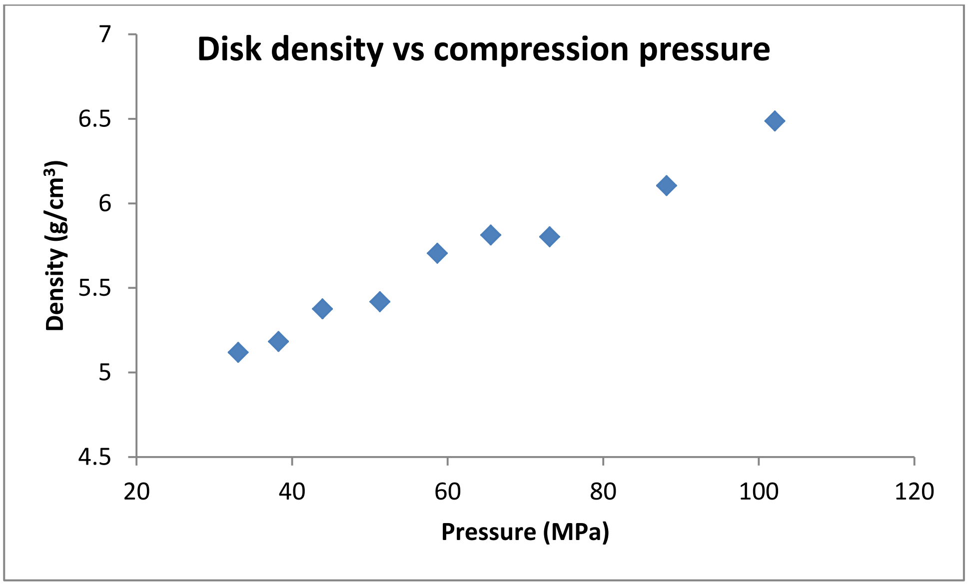

Figure 47: Change in density with pressure for disk compressed for two minutes, up to 100MPa

In 1998 Carnavas and Page[77] assessed the behaviour of copper powder when compressed with regards to its Young's Modulus and Poisson Ratio. It was found that once irregularly shaped copper powder, similar to that used in this study, was compressed to *ca* 0.7 times of the density of pure copper, both of these characteristics' behaviours changed. This was interpreted as the material being subject to predominantly localised inter-particle forces and localised plastic deformation of the particles when compressed to relative densities of below 0.7, but once the material was compressed to above this threshold there was bulk plastic deformation of the copper particles. Figure 48 shows how the relative density of the disks changes as compression pressure is increased.

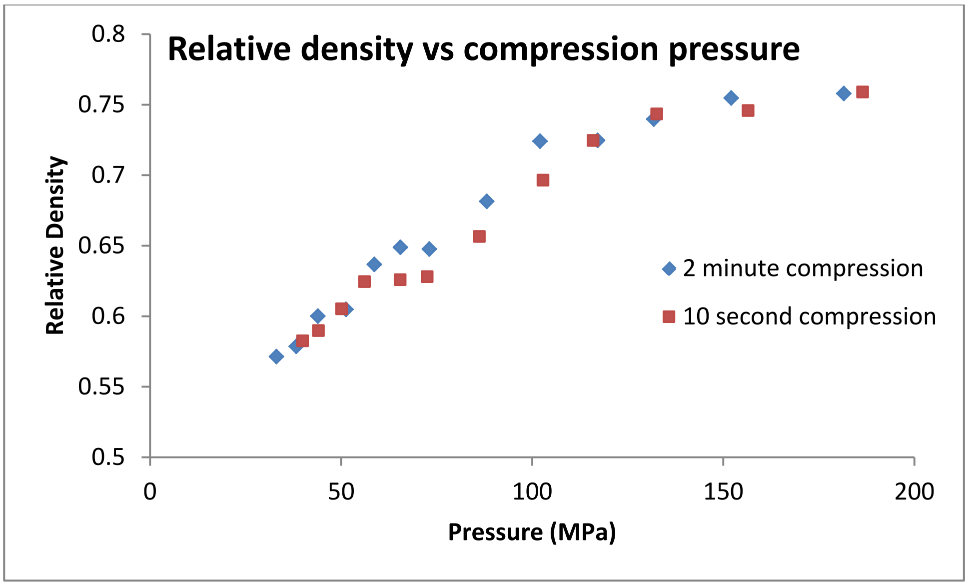

Figure 48: Change in relative density as compression pressure is increased

The data point for the disk compressed at 100MPa, the last point before the linearity of the graph is lost, has a relative density of 0.72. This change in compression behaviour is consistent with the relative density value seen by Carnavas and Page[77] before bulk plastic deformation was seen in the copper powder. As detailed in Section 1, the wetting characteristics of a solid are very strongly determined by surface structure, so in turn bulk plastic deformation of a surface should have a large effect on its wetting. Roll-off angle variation with relative density is shown in Figure 49.

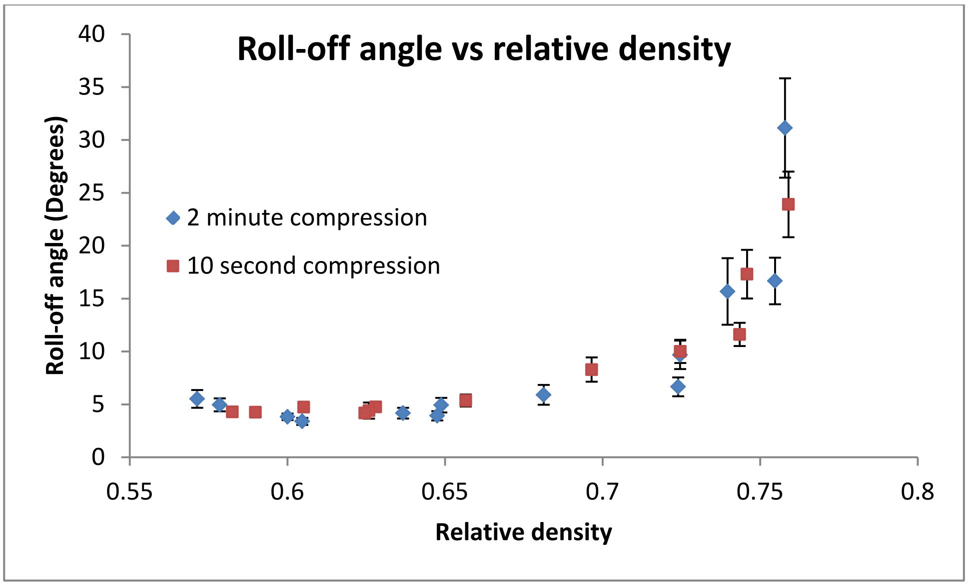

Figure 49: Roll-off angle variation with relative density

The roll-off angles seen in Figure 49 are reasonably consistent with one another until the relative density of 0.7 is surpassed. After this relative density is reached, much higher roll-off angles are begun to be seen. The onset of bulk plastic deformation of the powder particles at a relative density of 0.7 seen by Carnavas and Page is consistent with the SEM images of the disks compressed to 150 and 180MPa. Both of these materials had relative densities greater than 0.70, and easily seen in Figure 39 are the damaged particles left behind in the disk which were unable to be released in the abrasion process. This bulk plastic deformation observation explains the difference in surface structures seen in the SEM images in Figure 38 and Figure 39 as well as why large roll-off angles are seen in the compacts prepared at high pressures.

2.6 Effect of Temperature on Superhydrophobicity of Disks

In order to gain some insight into the thermal stability of the ecdysiastic materials, they were subjected to a range of elevated temperatures. These disks were then evaluated to confirm that their ecdysiastic character remained, and to see if there was any change in roll-off angle value using the testing method described in Section 2.3.2.

A series of disks composed of the 1-dodecanethiol treated superhydrophobic copper powder were compressed to 59MPa for two minutes as detailed in Section 2.3.1. These were then placed into an oven at a set temperature for one hour and removed and allowed to cool. A thermometer was placed in the same area of the oven as the disk, whose reading was used as the temperature each disk had been subjected to. The results for the roll-off angle trials are summarised in Figure 50.

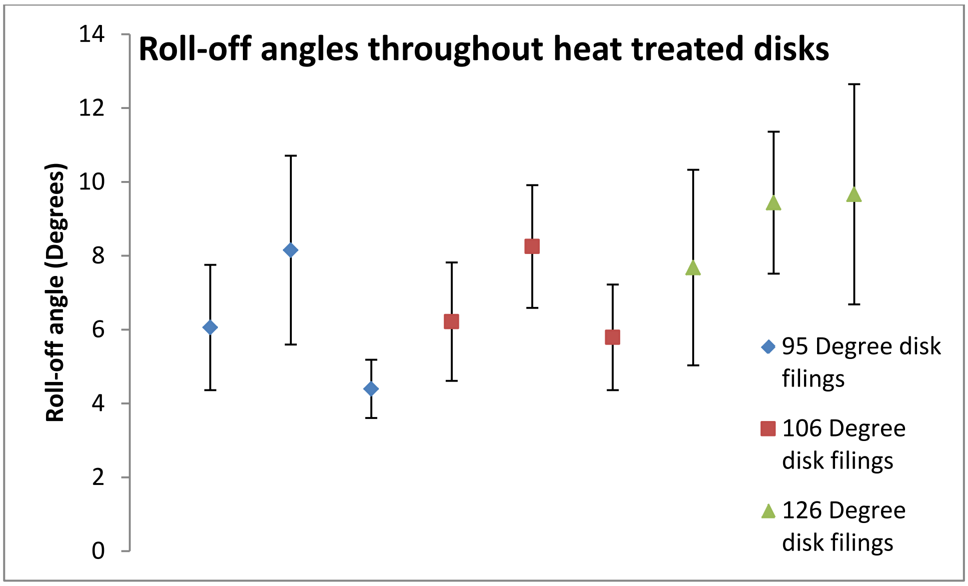

Figure 50: Roll-off angles recorded throughout heat treated 1-dodecanethiol treated copper disks

Figure 50 shows that, with the exception of one data point for the third freshly exposed surface on the disk subjected to 95˚C, roll-off angles are consistent throughout each disk, demonstrating that the ecdysiastic character of the disks is maintained after heating. Figure 51 shows overall roll-off angles calculated for each of the disks, whose thirty roll-off angle values for the three freshly exposed surfaces are treated as one data set.

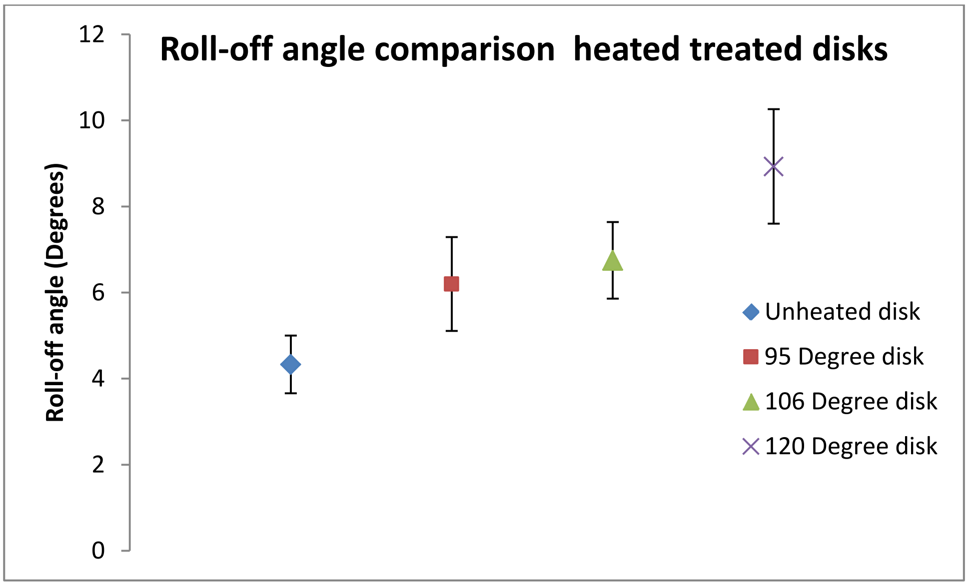

Figure 51: Comparison of overall roll-off angles for heat treated disks

The roll-off angle of the disks remains constant within experimental error for the disk that had been subjected to 95˚C temperature, but once 106˚C was reached it began to increase. The trend is seen to continue as the temperature is raised to

126˚C. This decrease in superhydrophobicity with increased temperature confirms that these ecdysiastic materials would not be amenable to sintering, as the temperatures used in sintering processes are regularly well in excess of the temperatures reached in the experimental work carried out.

2.7 Comparison of 1-Dodecanethiol with HDFT Treatment

Once the optimum compression conditions of a 59MPa, two minute compression for the 1-dodecanethiol treated copper powder ecdysiastic disks had been found, these conditions were applied to the HDFT treated powder from Section 2.1.2. The resulting material was compared with the 1-dodecanethiol treated analogue with regards to ecdysiastic character, roll-off angle and WCA.

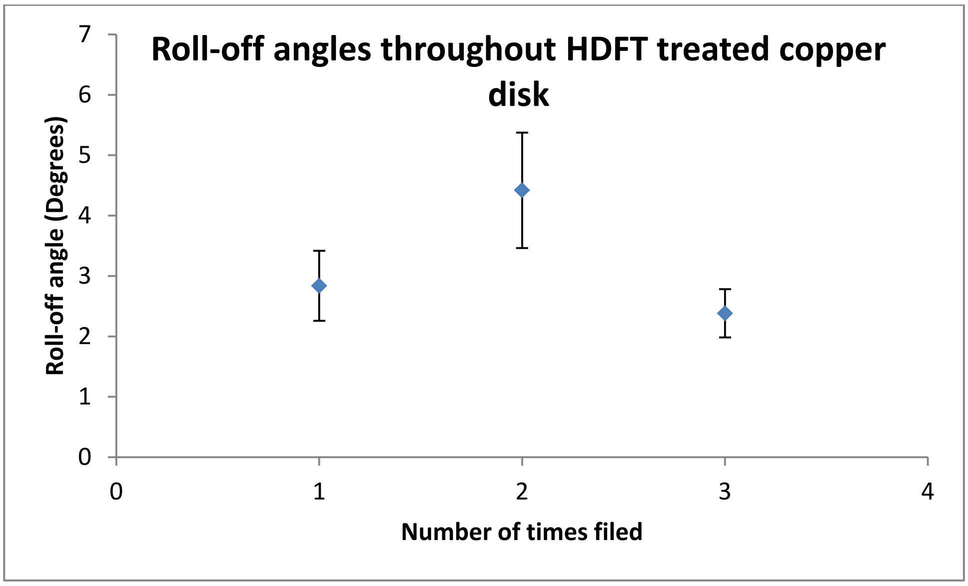

Figure 52: Roll-off angles throughout HDFT treated copper disk

Figure 52 shows that the second freshly exposed surface has a higher roll-off angle than the first and third measurements at the 95% confidence level. The first and third freshly exposed surfaces are consistent with one another within the margins of experimental error however, so the ecdysiastic nature of the material appears not to have been disproven here based on that aspect; the roll-off angle results for the second surface may well be an anomalous occurrence. WCA measurements of the disk were measured in the same way as described in Section 2.3.2.2 and the results are summarised in Figure 53.

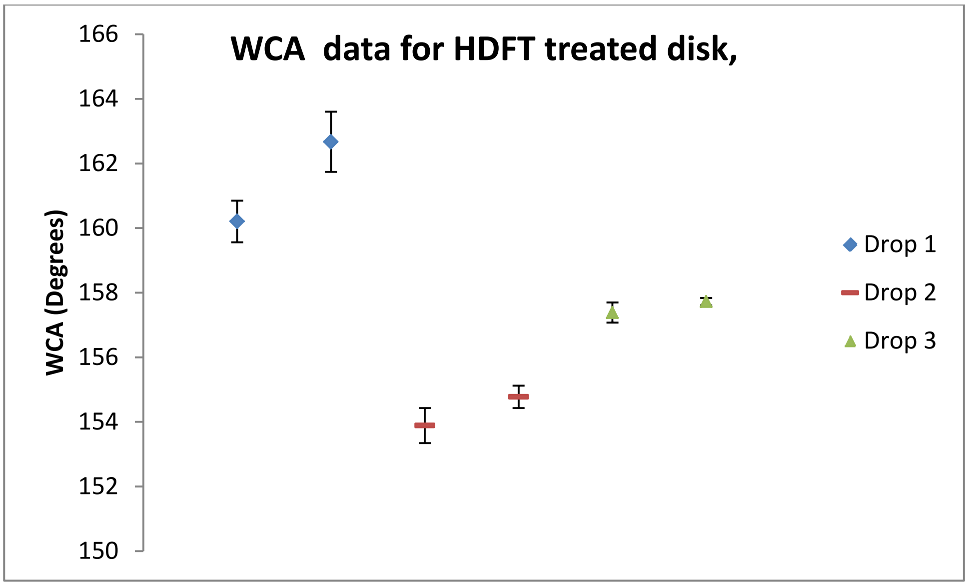

Figure 53: WCA measurements for HDFT treated disk compressed to 59MPa

The HDFT treated material is very similar in behaviour to its 1-dodecanethiol treated counterpart with regards to its WCA data. Different WCAs are seen on either side of one of the drops, there is some variation in WCA across each disk and the values of the WCAs appear to be in the same region for the two materials.

The results for all thirty roll-off angle measurements were combined to give an overall roll off angle for comparison with the overall roll-off angle of the 1-dodecanethiol treated copper disk which was prepared under the same compression conditions. An overall WCA range was calculated as detailed in Section 2.3.2.2 also, and the results are summarised in Table 5 below.

Table 5: Comparison of overall WCA and Roll-off angle data for different thiol treatments

Thiol treatment	Roll-off angle (Degrees)	WCA (Degrees)
1-Dodecanethiol	3.8±0.3	158±3
HDFT	3.2±0.5	159±3

Based on the data acquired here, there is no statistically significant difference between the two thiols when WCA and roll-off angle data are compared.

2.8 Replacing Copper with Zinc

The oxidation-reduction potentials of zinc also allow for galvanic deposition of silver, so the utilisation of zinc powder for ecdysiastic superhydrophobic materials was investigated.

2.8.1 General Procedure for Coating of Zinc Powder

25g zinc powder (BDH Limited, minimum assay 90%) was sifted and washed in 50mL acetone. This was then dried in a 40˚C oven. 40mL 0.02M aqueous silver nitrate was added with gentle stirring for two minutes. The mixture was left to rest for a further three minutes and the liquid was carefully decanted off. A further 30mL 0.02M silver nitrate was added with gentle stirring for two minutes. The powder was then filtered and washed with 150mL distilled water. It was then dried in a 40˚C oven and sifted. The powder was then treated with a solution of selected thiol.

2.8.1.1 1-Dodecanethiol Coating of Zinc Powder

10g silver coated zinc powder was added to 40mL of 0.1M 1-dodecanethiol (Alpha Aesar) solution in 95% ethanol. This was left overnight with occasional agitation, filtered off, washed with 95% ethanol and dried overnight in a 40˚C oven. Once dried the powder was then sifted.

2.8.1.2 1H,1H,2H,2H-Perfluorodecanethiol Coating of Zinc Powder

10g silver coated zinc powder was added to 40mL of 0.01M 1H,1H,2H,2H-Perfluorodecanethiol (Sigma-Aldrich) solution in dichloromethane. This was left overnight with occasional agitation, filtered off, washed with dichloromethane and dried overnight in a 40˚C oven. Once dried the powder was then sifted.

2.8.2 Assessment of Treated Zinc

The 1-dodecanethiol treated zinc powder was compressed into disks as outlined in Section 2.3.1 for two minutes at pressures of 59MPa and 150MPa. Roll-off angle measurements were carried out on each of the disks as described in 2.3.2 to establish the ecdysiastic character of the disks.

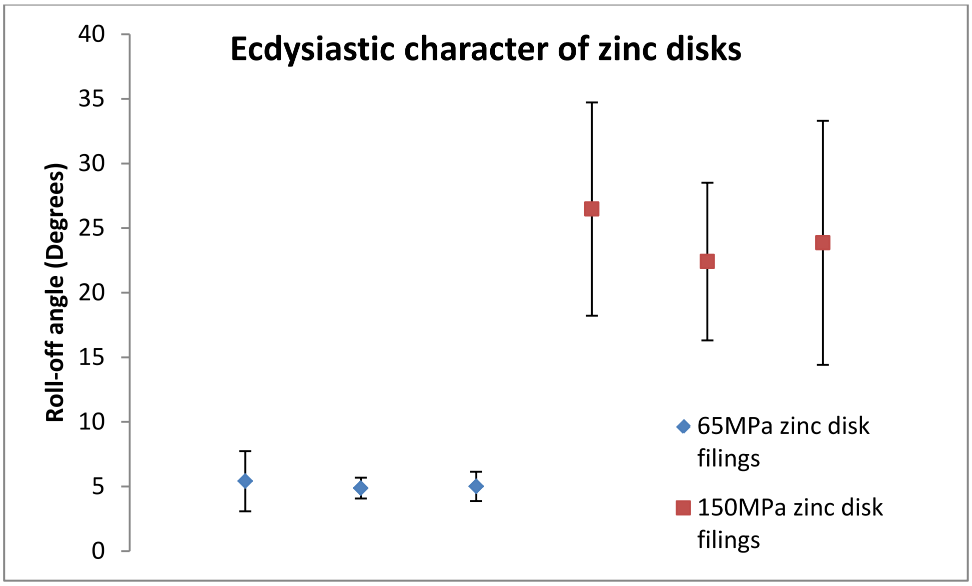

Figure 54: Roll-off angles throughout 1-dodecanethiol treated zinc disks compressed to 59MPa and 150MPa

The zinc powder appears in Figure 54 to have the same ecdysiastic characteristics that are seen in the ecdysiastic materials that are comprised of the superhydrophobic copper powder. The ecdysiastic nature of the material is not affected over the pressure range assessed, and it appears as though the trend of increasing roll-off angle with increasing pressure continues here with the zinc materials also.

The 30 individual roll-off angle measurements for the zinc disks were treated as one data set to give an overall roll-off angle each of the disks for comparison with the analogous superhydrophobic copper disk. The results are summarised in Table 6.

Table 6: Comparison of 1-dodecanethiol treated superhydrophobic zinc and copper ecdysiastic materials

	Roll-off angle (Degrees)	Density (g/cm^3)
Zinc Disk, 59MPa	5.1±0.8	4.49
Zinc Disk, 150MPa	24±4	5.80
Copper Disk, 59MPa	3.8±0.3	5.70
Copper Disk, 150MPa	17±2	6.76

Table 6 shows that the zinc disks have a higher roll-off angle than the copper analogues do but are of a lower density, and that the increase in pressure from 59MPa to 150MPa has increased the roll-off angle of the zinc compact.

2.8.2.1 Comparison of 1-dodecanethiol and HDFT on Superhydrophobic Zinc Disks

The HDFT treated zinc powder from Section 2.8.1.2 was compressed to 59MPa and roll-off angle testing as detailed in Section 2.3.2 was carried out. The results for roll-off angles calculated for all three of the freshly exposed surfaces are summarised in Figure 55.

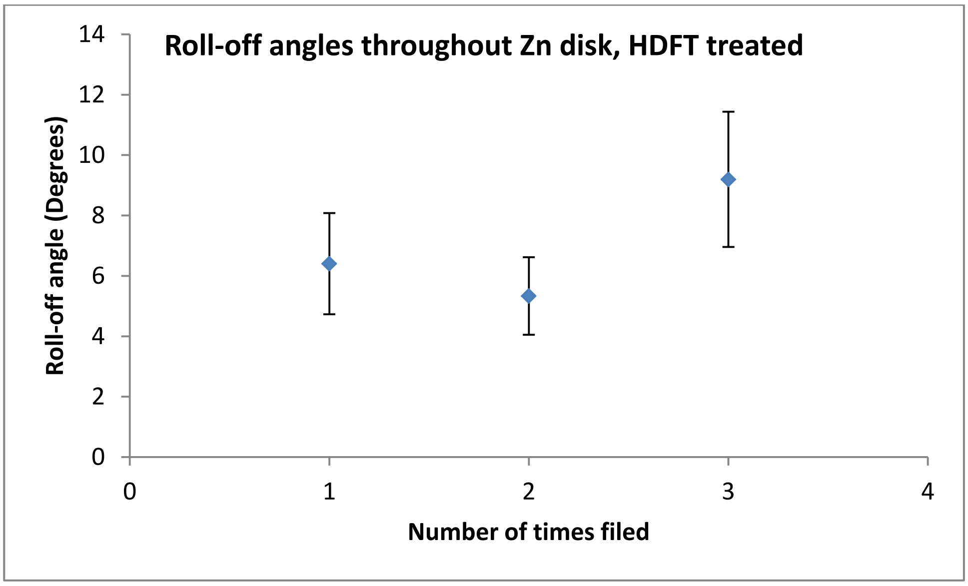

Figure 55: Roll-off angles recorded throughout HDFT treated zinc disk, compressed to 59MPa

Figure 55 shows that the second and third exposed surfaces are not consistent with each other at a 95% confidence level. A similar behaviour was seen in the HDFT treated copper powder analogue in Section 2.7 which was found not to be uniform throughout with regards to roll-off angle. Treating all thirty roll-off angles as one data set to calculate an overall roll-off angle resulted in a value of 7.0±1˚ for the HDFT treated zinc disk. This value is higher at the 95% confidence level than that seen for the 1-dodecanethiol treated material at 5.1±0.8˚. This is perhaps unexpected as fluoroalkyl groups have the lowest surface energies known, so one would expect that if there is any difference in roll-off angle between the two thiols used that the fluoroalkyl chain thiol would have a lower roll-off angle. These observations may have something to do with the lower concentration of the more expensive fluoroalkylthiol used when compared with the 1-dodecanethiol solution.

2.8.3 SEM Investigations of Superhydrophobic Zinc Materials

The morphology of the zinc materials was inspected by scanning electron microscope as detailed in Section 2.3.3. Untreated zinc powder, 1-dodecanethiol treated zinc powder and the two 1-dodecanethiol treated zinc disks prepared at different pressures in Section 2.8.2 were all examined. Figure 56 shows untreated zinc powder at two different magnifications. The zinc is seen to be irregular in shape and its size ranges from 5 to 50µm.

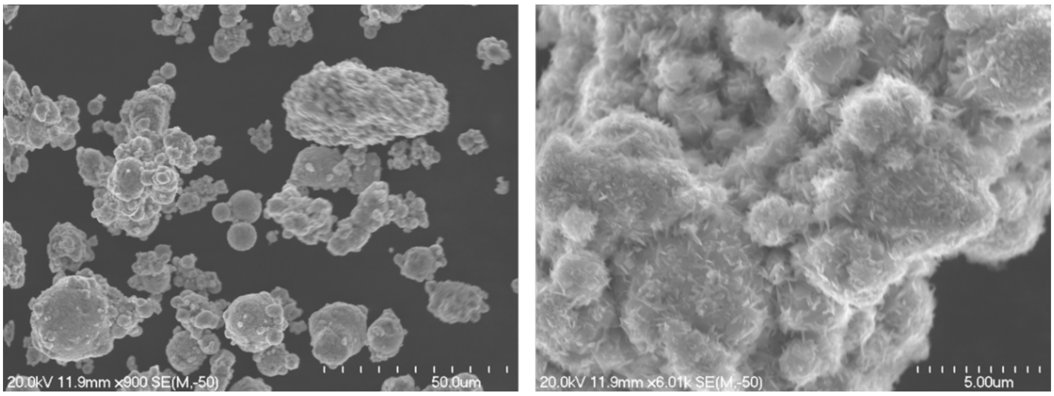

Figure 56: SEM images of untreated zinc powder

Figure 57 shows the zinc powder after treatment with silver nitrate and 1-dodecanethiol solution at two different magnifications. The silver does not appear to be deposited uniformly over the powder, though there is evidence of silver deposition shown by the dendritic structures seen in the higher magnification image.

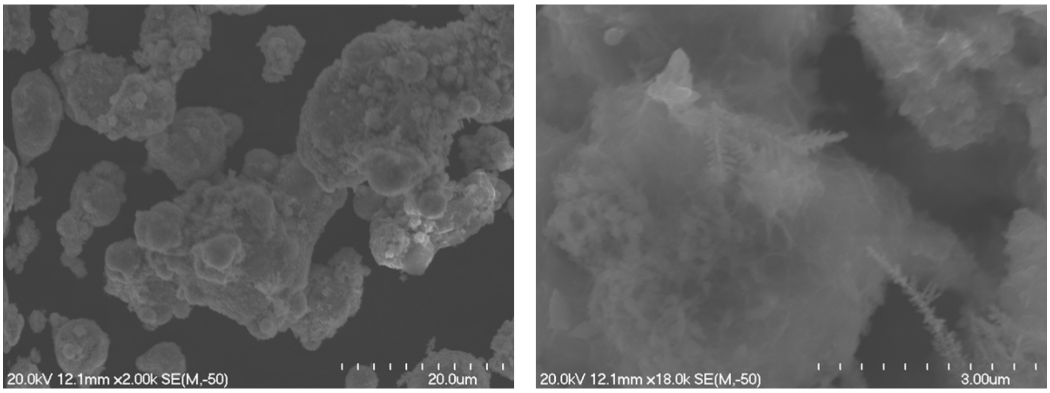

Figure 57: SEM images of silver coated, HDFT treated zinc powder. Dendritic structures seen at higher magnifications are silver deposits (right)

A freshly exposed surface of the HDFT treated zinc disk compressed at 59MPa is depicted in Figure 58. The images show flat spots on the surface where the zinc has been filed which are very similar in appearance to those seen on the copper disks compressed to high pressure in Figure 39.

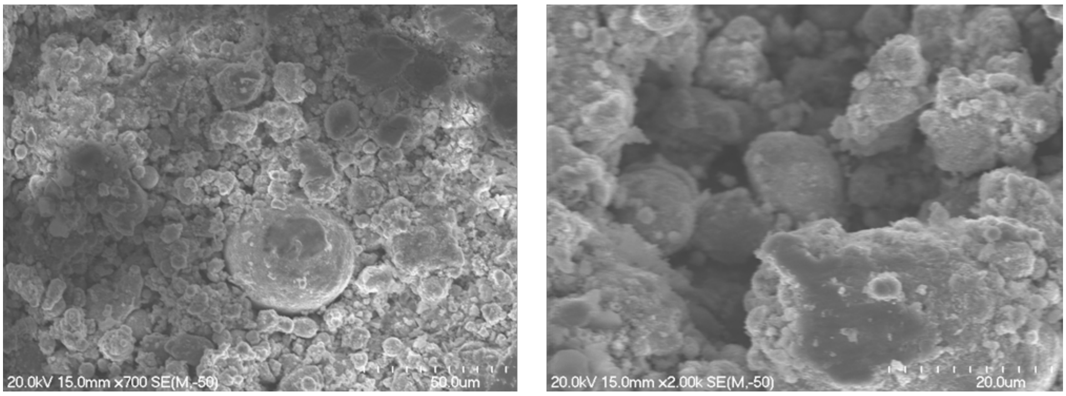

Figure 58: SEM images of HDFT treated zinc disk compressed to 59MPa

This suggests that the zinc disks have already at 59MPa pressure been compressed to beyond the point at which bulk plastic deformation of zinc begins. This may go some way towards explaining the zinc material’s higher roll-off angle compared to the superhydrophobic copper powder when compressed to the same pressure.

3 The Application of Superhydrophobic Ecdysiastic Powders to Titanium and Other Metals

The cold pressing method of generating ecdysiastic superhydrophobic materials described in Section 2 was adapted to apply it to a chosen metal substrate. Superhydrophobic copper powder was compressed onto a powdered form of the chosen metal to graft an ecdysiastic superhydrophobic surface onto a different bulk substrate which may have desirable bulk properties, for example titanium or aluminium (Figure 59).

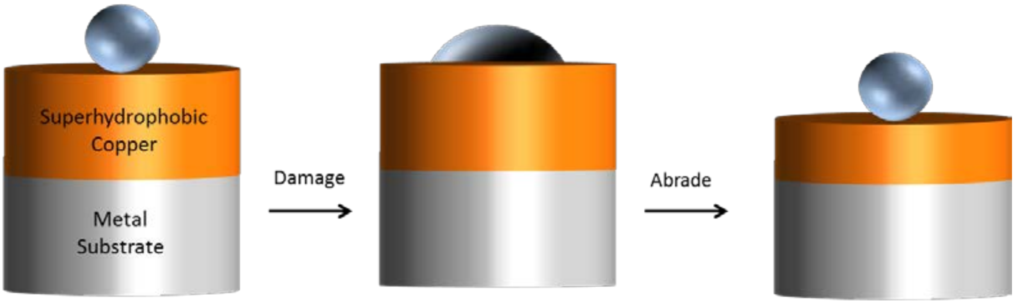

Figure 59: Superhydrophobic ecdysiastic copper layer applied to a metal substrate

It was expected that the copper layer on top of the chosen substrate would have the same superhydrophobic properties and ecdysiastic characteristics of the solely superhydrophobic copper disks in Section 2.

3.1 Superhydrophobic Ecdysiastic Surfaces on Titanium

Approximately 1.5 grams of 1-dodecanethiol treated superhydrophobic copper powder from Section 2.1.1 was loaded into a SPECAC 13mm evacuable pellet die and gently flattened. On top of the copper powder was loaded approximately 1 gram titanium 200 mesh hydrogenation-dehydrogenation (HDH) powder. The die was then compressed in a Lloyd LR30K Materials Tester as outlined in Section 2.3.1 for two minutes at a pressure of 59MPa. The disk was then removed and carefully de-moulded. The process was repeated using the HDFT treated superhydrophobic copper powder from Section 2.1.2 in place of the 1-dodecanethiol treated copper powder also. The resulting disks consisted of a layer of superhydrophobic copper powder on top of a titanium substrate (Figure 60).

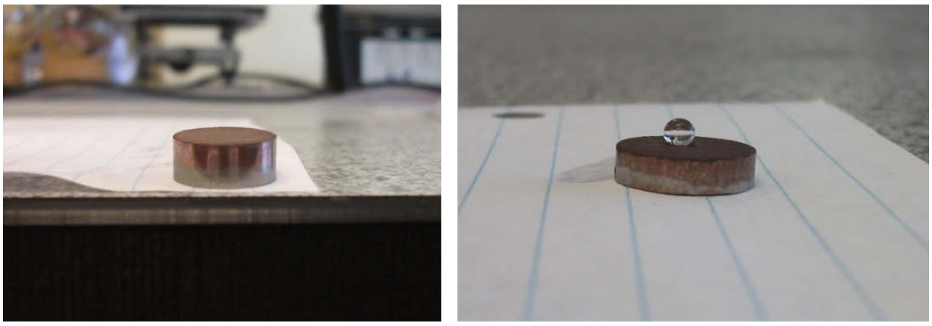

Figure 60: Superhydrophobic copper layer on titanium substrate

Roll-off angle measurements of the disks were carried out as described in Section 2.3.2. The results of the roll-off angle trials are shown in Figure 61 and Figure 62.

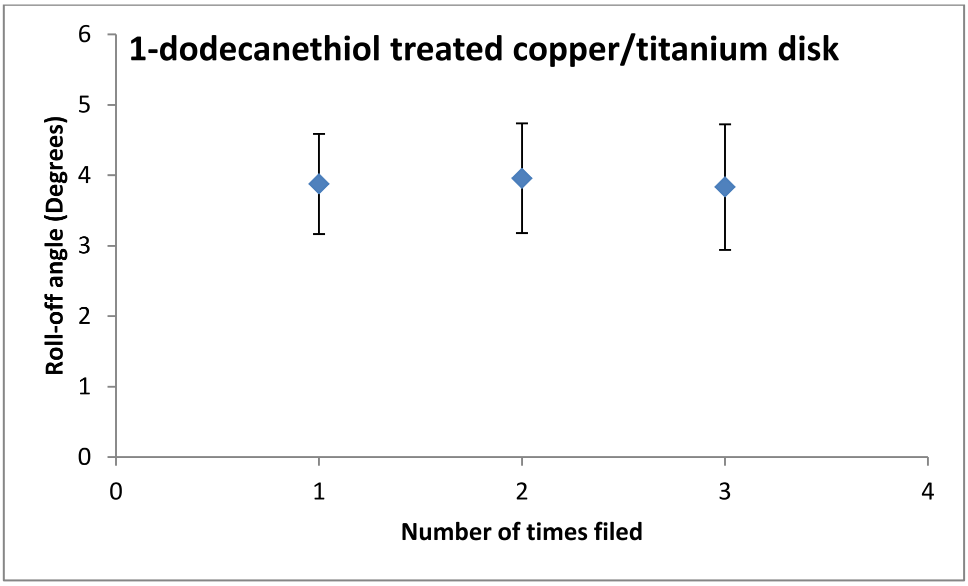

Figure 61: Roll-off angles throughout 1-dodecanethiol treated superhydrophobic copper/titanium disk

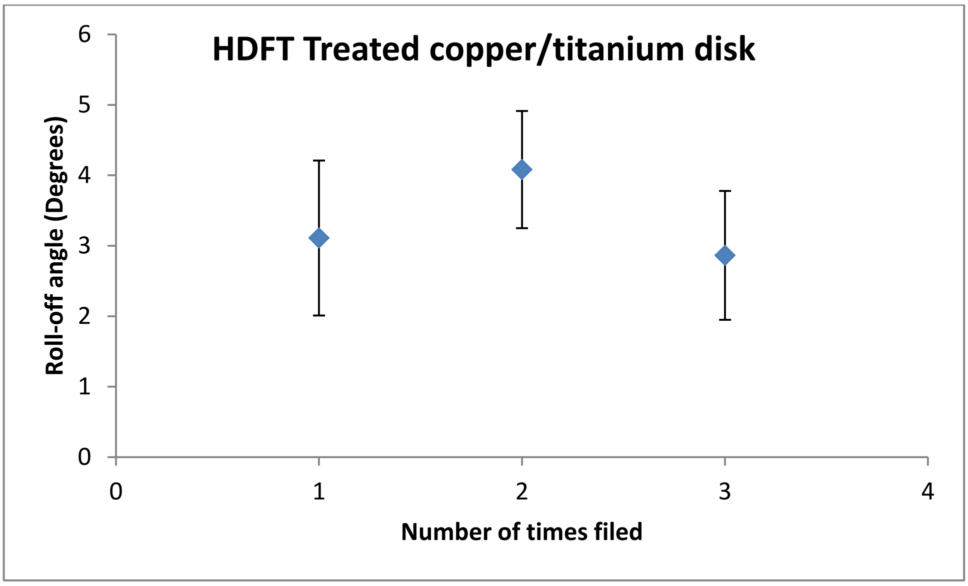

Figure 62: Roll-off angles throughout HDFT treated superhydrophobic copper/titanium disk

Figure 61 and Figure 62 confirm that the roll-off angles are the same within experimental error throughout the superhydrophobic copper layers applied to the titanium substrate, so the application to titanium has not affected the ecdysiastic qualities of the material. The exclusively HDFT treated superhydrophobic copper disk showed one roll-off angle as being inconsistent with others at the 95% confidence level in Section 2.7, but the confirmation of the ecdysiastic nature of the material here does suggest that the incident was an anomalous occurrence, however.

All thirty roll-off angles measured for each disk were treated as one data set to calculate an overall roll-off angle. These are compared with the roll-off angles of their solely superhydrophobic copper analogues in Figure 63.

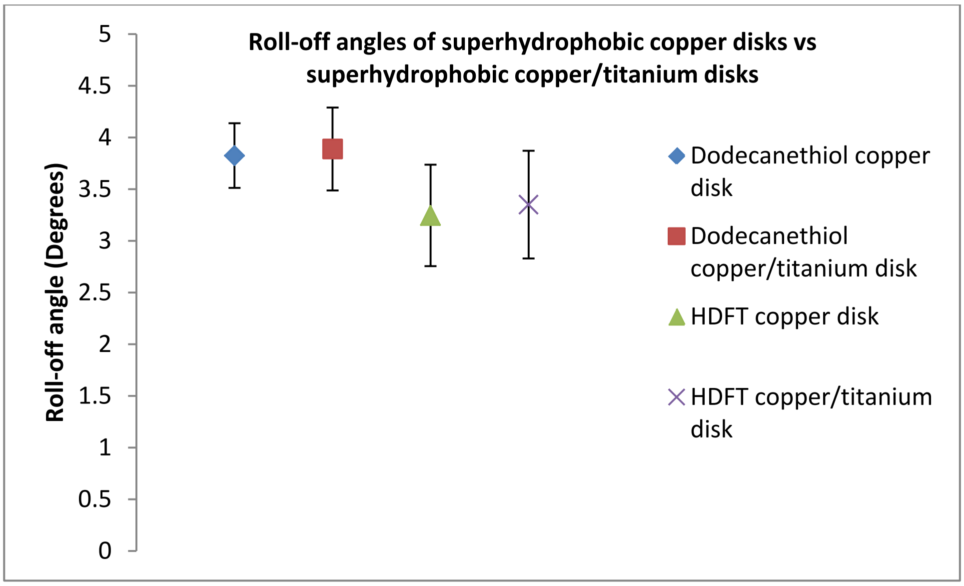

Figure 63: Comparison of roll-off angles for superhydrophobic copper disks and superhydrophobic copper/titanium disks

Figure 63 clearly indicates that there is no change in roll-off angle between the solely superhydrophobic copper disks and the superhydrophobic copper pressed onto titanium. Additionally, there is no statistically significant difference between the two different thiol treatments, which was also seen in the superhydrophobic copper materials in Section 2. Numerical data for the roll-off angles of the superhydrophobic ecdysiastic titanium materials can be found in Appendix Four.

3.1.1 WCA Measurements of Superhydrophobic Edcysiastic Surfaces on Titanium

WCA measurements were carried out on the superhydrophobic copper/titanium disks as outlined in Section 2.3.2.2 for comparison of their values and behaviour with their solely superhydrophobic copper counterpart. The results of the WCA measurements are summarised in Figure 64 and Figure 65.

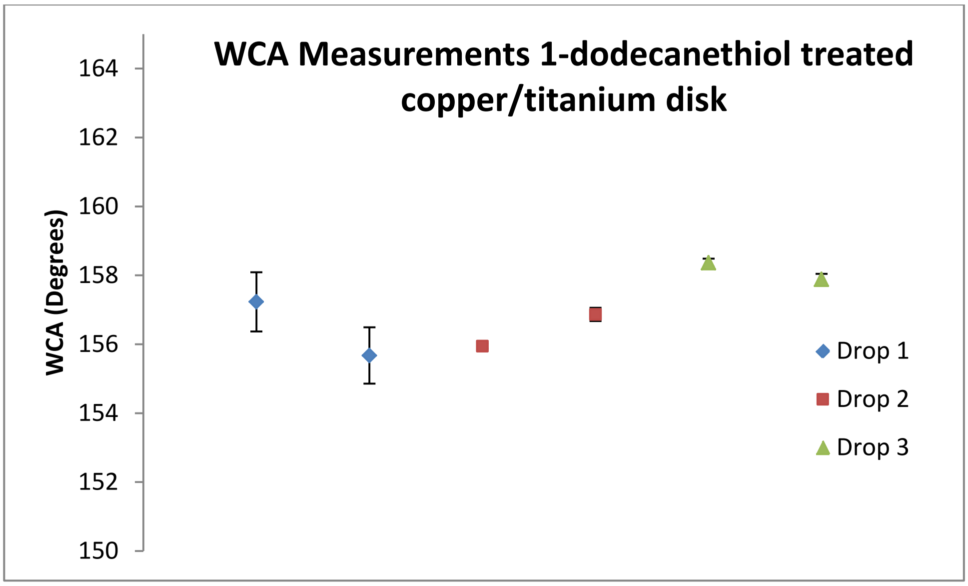

Figure 64: WCA measurements of 1-dodecanethiol treated copper/titanium disk

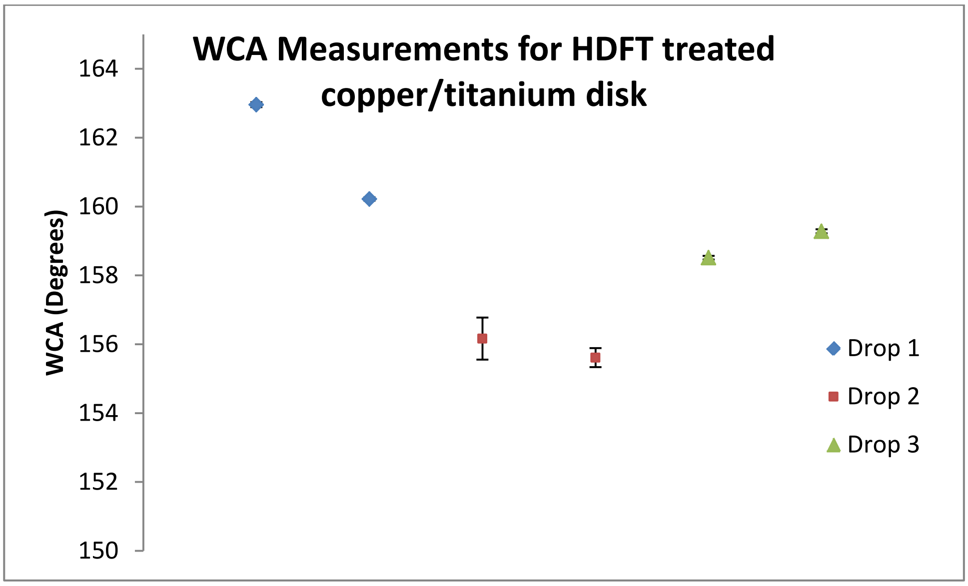

Figure 65: WCA measurements of HDFT treated copper/titanium disk

Both of the materials show very similar behaviours with regards to WCA values to the purely superhydrophobic copper disks tested in Section 2.3.2.2. All values recorded are above the 150° threshold required for a surface to be deemed superhydrophobic and not all drops show the same WCA within experimental error. Both disks here also have two water drops out of the three tested that exhibit different WCAs on either side of the drop. In order to compare the WCA values with the pure superhydrophobic copper disks, an overall WCA range was calculated as described in Section 2.3.2.2. The results of the comparison are shown in Figure 66 below.

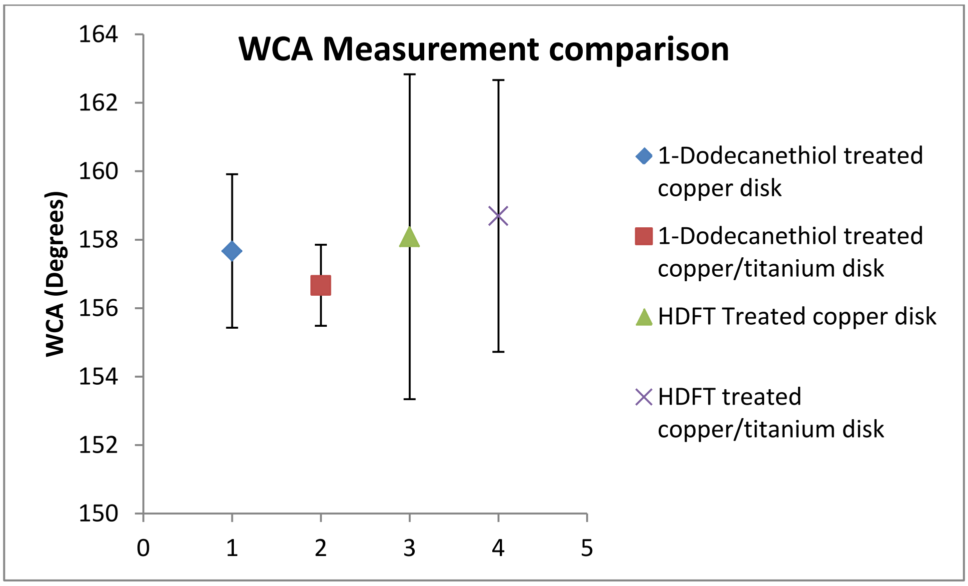

Figure 66: WCA comparison between superhydrophobic copper and superhydrophobic copper/titanium disks

Figure 66 demonstrates that the WCA values for the titanium with the superhydrophobic copper compressed onto it mirrors the behaviour of the purely superhydrophobic copper disks. Moreover, there is still no significant difference in WCA between the 1-dodecanethiol and HDFT treatments.

The static WCA data, while shown not to be as informative as roll-off angle data, is useful to confirm that another aspect of wetting is consistent between the purely superhydrophobic disks in Section 2 and these disks where the material has been grafted onto another substrate. Together with the roll-off angle data it indicates that the superhydrophobicity of the material, as well as the ecdysiastic nature of the superhydrophobic material, has been maintained on compression onto a hydrophilic titanium substrate.

3.1.2 SEM Investigation of Superhydrophobic Titanium Materials

The morphology of the ecdysiastic superhydrophobic materials was investigated as described in Section 2.3.3 to gain an insight into how the titanium powder was compacted together into a disk. First, images of the titanium 200 mesh HDH powder were recorded, followed by the recording of images of the powder compressed into a disk. The images recorded are depicted in Figure 67.

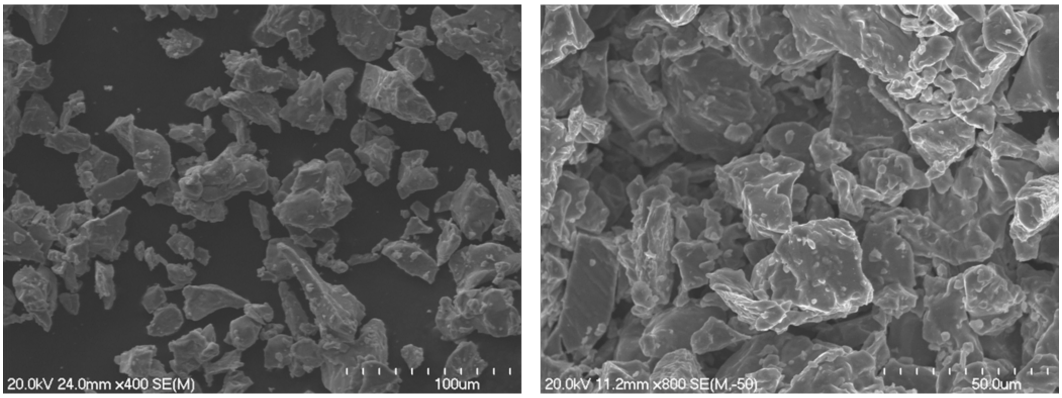

Figure 67: SEM images of titanium 200 mesh HDH powder at 400x magnification (left); titanium 200 mesh HDH powder compressed into a disk, 800x magnification (right)

The jagged form of the powder allows a high degree of mechanical interlocking of the particles on compression, which is of importance in holding the material together. This is proven by the fact that gas atomised (GA) titanium 200 mesh powder did not form a solid material when compressed under the same conditions, but rather remained in a fluid, powder form. Images of the titanium 200 mesh GA powder are shown in Figure 68.

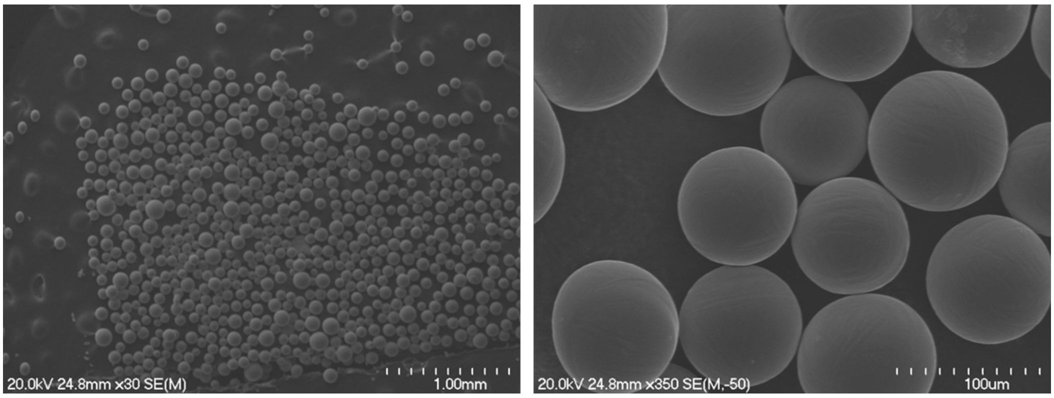

Figure 68: SEM images of titanium 200 mesh GA powder at 30x magnification (left) and 350x magnification (right)

The spherical form of the GA powder does not permit any of the mechanical interlocking that is seen in Figure 67 from the titanium HDH powder. While the mechanical interlocking of the powder particles is clearly of importance, it is not the only factor holding the titanium portion of the material together. The HDH 200 mesh powdered form of the titanium alloy Ti-6Al-4V did not form a solid compact after going through the compression procedure at the same pressure either. The HDH processed powder will have a similar morphology to the pure

HDH titanium powder due to its having the same HDH method of production, and hence has the potential to form these mechanically interlocking interactions.

Ti-6Al-4V is harder than pure titanium,[54] so is more resistant to plastic deformation. A potential explanation for it not forming a solid compact is that localised plastic deformation occurs on compressing the pure titanium HDH powder which aids in holding the material together, but at the pressures used in the study this did not occur for the Ti-6Al-4V alloyed HDH powder.

Gerdemann and Jablonski in their study[78] on the compaction of titanium powders found that Ti-6Al-4V powder gave the lowest densities amongst the tested powders for a given applied pressure. This was attributed to the high yield strength of the alloy, and it was concluded that both powder particle shape and strength are very important variables in the powder compaction and densification process for titanium and its alloys.

In order to view the interface at which the titanium and copper phases meet, one of the compressed disks had its curved outer edge filed followed by inspection of the exposed surface in the SEM. The images in Figure 69 show the superhydrophobic copper-titanium interface.

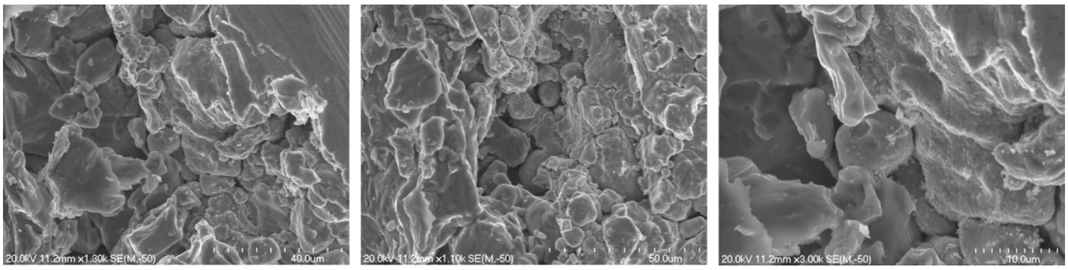

Figure 69: SEM images of the superhydrophobic copper-titanium 200 mesh HDH interface

In all of the images shown in Figure 69, the titanium is on the left, jagged in shape with a smooth surface. The copper powder is at the right of the image, with finer detail on its surface which is the deposited silver. There is no clear intermediate phase between the two portions of the disk; it appears to be a purely mechanical interlocking amongst the powder particles preventing the material shearing apart.

3.2 Effect of Order of Synthesis of Ecdysiastic Disks

The effect of the order processing of the ecdysiastic copper disks on a titanium substrate was investigated to see whether it affected either the roll-off angle values or the ecdysiastic nature of the materials. If the method of synthesis could be changed from that described in Section 3.1 to compressing the copper powder, or silver coated copper powder onto titanium and later rendering it superhydrophobic, it could have its advantages. This approach, if it retains the superhydrophobic ecdysiastic characteristics shown by the disks in Section 3.1, would potentially allow a sintering process after compressing the copper onto titanium to impart extra strength into the material before the thiol is adsorbed onto the material.

3.2.1 Compressing Copper Powder onto Titanium then Rendering Superhydrophobic

Approximately 1.5g 200 mesh copper powder was placed into a SPECAC 13mm evacuable pellet die and gently flattened. Approximately 1g of titanium 200 mesh HDH powder was placed on top of the copper powder and this was compressed for two minutes at 59MPa as described in Section 2.3.1. The resulting disk was washed for 90 seconds in 0.5% nitric acid, submerging several times to dissipate any bubbles evolving from the porous structure, and rinsed in distilled water. It was then dried in a 40˚C oven. The disk was then immersed in 20mL 0.02M silver nitrate solution for five minutes, again submerged several times to remove any air bubbles emerging from the porous structure. This was followed by a rinse with distilled water and drying in a 40˚C oven. Once dried it was left in 10mL 0.1M 1-dodecanethiol solution in ethanol for 24 hours. After removal it was rinsed in ethanol and dried in a 40˚C oven.

A second disk was prepared in parallel and immersed in 0.01M HDFT in dichloromethane for 24 hours and rinsed in dichloromethane followed by drying in a 40 ˚C oven in place of the 1-dodecanethiol treatment.

The disks prepared in this process had a thick, fluffy layer of silver deposited on the exposed layer of the copper portion of the disk. This silver layer was extremely fragile and showed very poor adherence to the copper below, to the point that some even detached when removing the disk from the silver nitrate solution. Several roll-off angle measurements of the disks were recorded before any abrasion was done, but these were of little use due to the discontinuities in the surfaces where the silver had come off. Roll-off angles of freshly abraded layers throughout the disks were recorded as outlined in Section 2.3.2 (Figure 70, Figure 71).

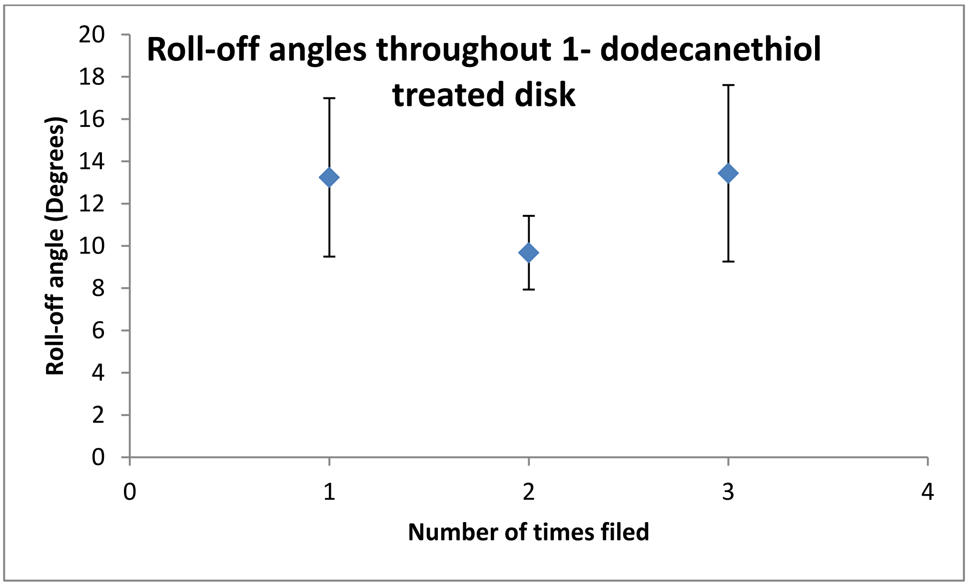

Figure 70: Roll-off angles throughout 1-dodecanethiol treated disk

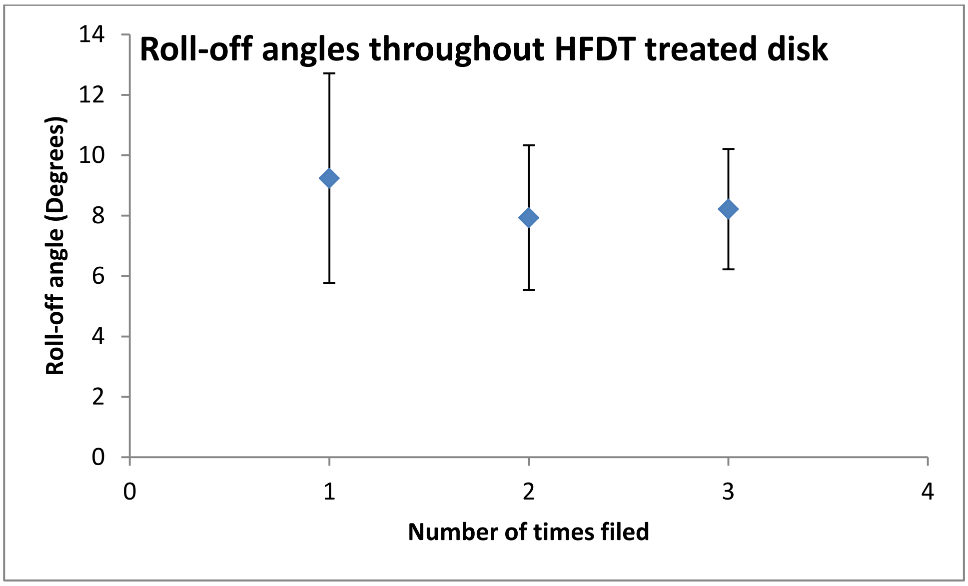

Figure 71: Roll-off angles throughout HDFT treated disk

Figures 70 and 71 indicate that this change in the order of preparation of the disks appears not to have affected the ecdysiastic nature of the materials within the margin of experimental error. Since there was no statistically significant difference throughout the disks, the results for filing through each disk were grouped together to see whether there was a difference in value of roll-off angle for this method from the method reported in 2.1 (Figure 72).

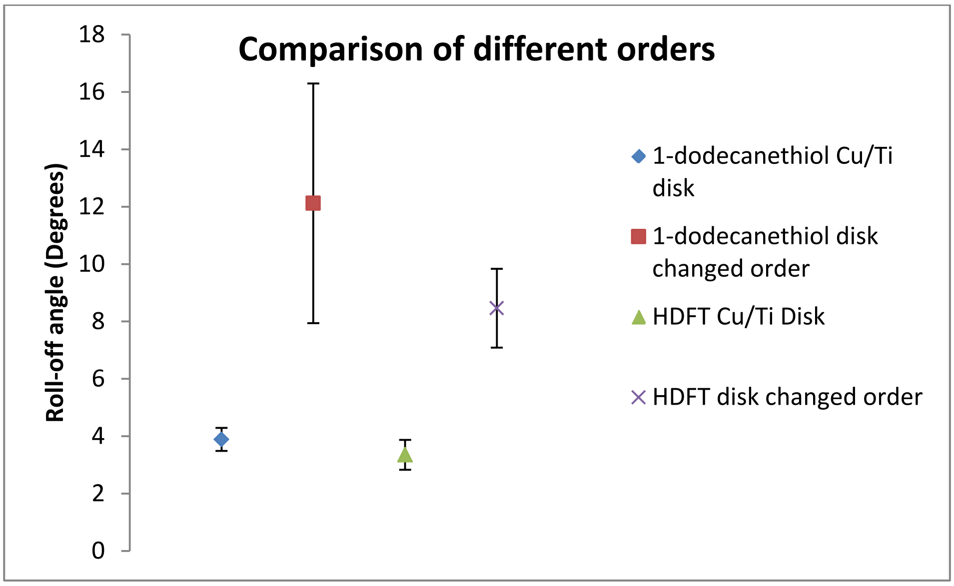

Figure 72: Roll-off angle comparison for different process order

Figure 72 indicates there is a clear difference in roll-off angle for the two different synthetic procedures. Rendering the copper superhydrophobic prior to the compression step gives a significantly lower roll-off angle than compressing the copper powder and attempting to render it superhydrophobic. It also appears to give a more consistent surface which is reflected in the errors associated with the measurements.

Intuitively these observations make sense in that the free copper powder has its entire surface exposed to the silver nitrate solution and later to the thiol which gives much better opportunity for complete surface coverage. When the copper is compressed into a disk beforehand it necessarily has some points of contact with other nearby copper particles which inhibits this access for silver deposition and thiol adsorption. This means that some portions of the copper powder are essentially untreated and are likely to become exposed as the disk is abraded.

3.2.2 Compressing Silver Coated Copper onto Titanium Followed by Thiol Treatment

Approximately 1.5g of silver coated copper powder from Section 2.1 was loaded into a SPECAC 13mm evacuable pellet die and gently flattened. 1g titanium 200 mesh HDH powder was placed on top of this, and the die was compressed to 59MPa for two minutes as described in Section 2.3.1. Two disks were prepared in this fashion; one was immersed in 10mL 0.1M 1-dodecanethiol solution in ethanol, the other in 25mL 0.01M HDFT in dichloromethane. Both were left in solution for two hours, removed and washed in their respective solvents and dried in a 40˚C oven.

The disks were removed after two hours in the thiol solution due to the fact that the silver coated copper portion of the disk was beginning to disintegrate. Both showed large water contact angles once dry but very large roll-off angles (*ca* 45˚) before any abrasion had been carried out. The ecdysiastic character of the disks was evaluated by measuring roll-off angles of freshly abraded layers throughout the disk as described in Section 2.3.2.

3.2.2.1 1-Dodecanethiol Treated Disk

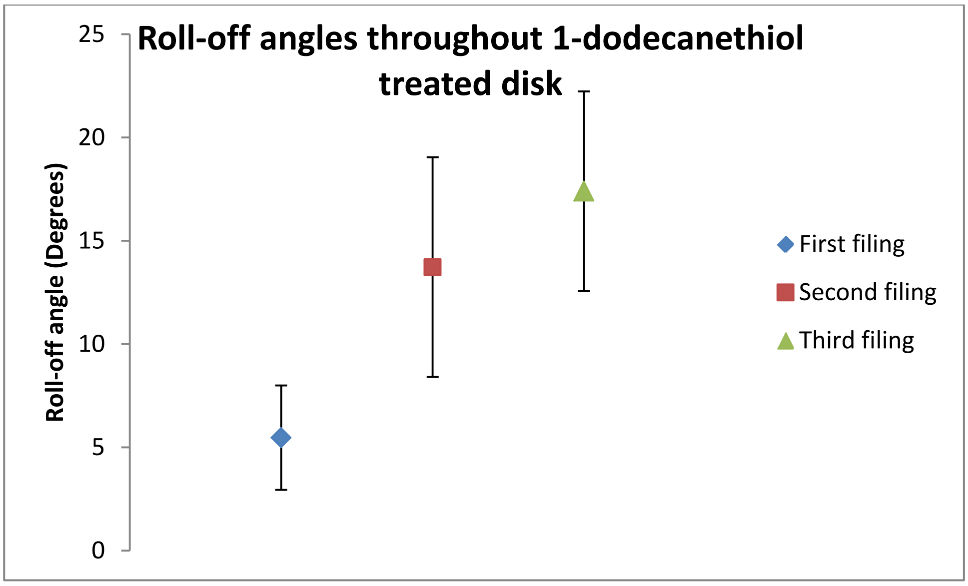

Figure 73: Roll-off angles throughout 1-dodecanethiol treated disk

The first exposed layer has a statistically significantly lower difference from the second and third layers of the material at the 95% confidence level. This means that the material does not show superhydrophobic ecdysiastic characteristics since the wetting behaviour changes as one progresses further through the disk.

This is perhaps unexpected, as diffusion of the thiol solution to form a SAM over the silver coated copper powder could be expected to be less hindered by contact points between the silver coated copper powder particles than silver deposition onto already compressed copper powder, which did show ecdysiastic character after treatment with thiol in Section 3.2.1. This is possibly attributable to the shorter immersion time of two hours in the thiol solution not allowing for diffusion of thiol throughout the material.

As roll-off angle changes throughout the disk for the 1-dodecanethiol treated sample, it would be inappropriate to pool all the roll-off angle measurements and treat it as one data set to give the disk an overall roll-off angle value. To further validate this, the distribution of the roll-off angles for all thirty measurements taken on each of the disks were normalised as detailed in Section 2.3.2.1 and a histogram constructed of the resulting data.

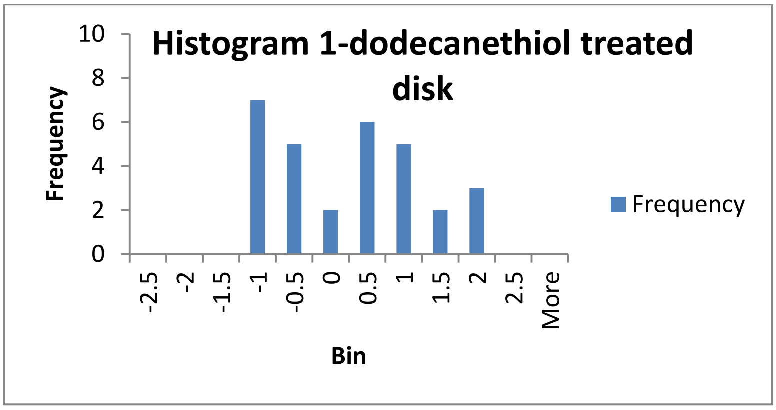

Figure 74: Histogram of z-scores for 1-dodecanethiol treated disk

Figure 74 shows the histogram of the z-scores for all 30 roll-off angle trials done on the 1-dodecanethiol treated disk, which indicates that the results are not normally distributed, confirming that the pooling of results for an overall roll-off angle would be inappropriate.

3.2.2.2 HDFT Treated Disk

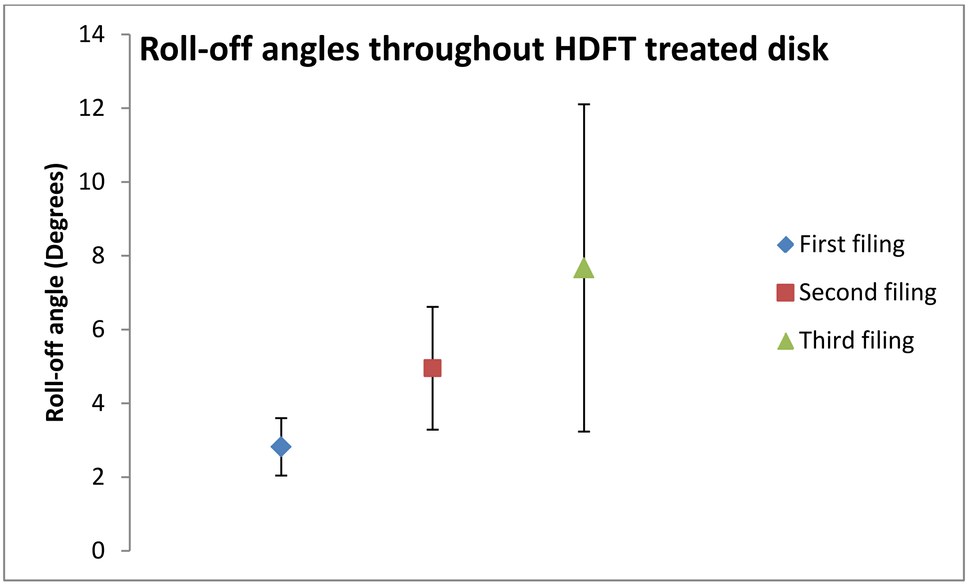

Figure 75: Roll-off angles throughout HDFT treated disk

In Figure 75, no statistically significant differences are seen for roll-off angle values for the material treated with HDFT, although the large errors associated with measurements seen on the 1-dodecanethiol treated disk in Figure 73 are also seen here. While the roll-off angles are within experimental error of one another as one travels through the disk in this instance, one is hesitant to say that the HDFT treated material shows ecdysiastic characteristics.

This is due to the fact that the errors associated with the measurements grow to become very large as measurements are taken further into the disk, and that the HDFT treated materials have mirrored the behaviour of the 1-dodecanethiol treated materials, which did not show ecdysiastic characteristics under this preparation method, throughout this work.

Figure 76 shows a histogram of the normalised distribution (Section 2.3.2.1) of all roll-off angles recorded for the HDFT treated disk.

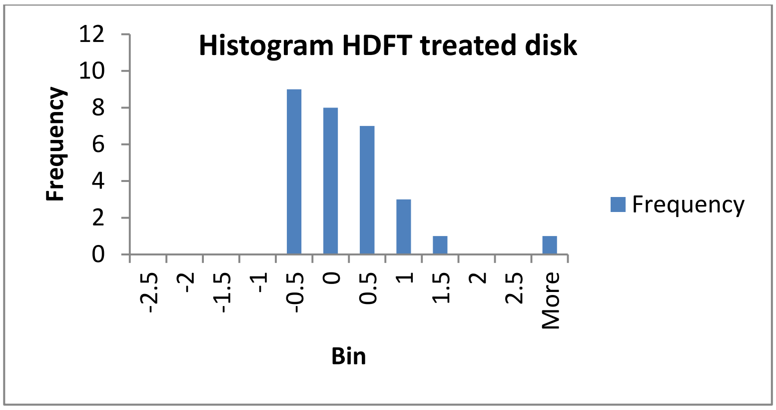

Figure 76: Histogram of z-scores for HDFT treated disk

The roll-off angle results for all measurements taken on the HDFT treated disk appear to be closer to a normal approximation than the 1-dodecanethiol treated counterpart, but there is still a marked asymmetry to it. Results were therefore not pooled from the layers throughout the disk to give an overall disk roll-off angle for the HDFT treated disk.

3.2.2.3 Comparison of 1-Dodecanethiol and HDFT Treated Disks

Since it was inappropriate to calculate an overall roll-off angle for the disks prepared in this fashion, it was chosen to compare their roll off angles for each layer tested. The comparisons for each layer are shown in Figure 77.

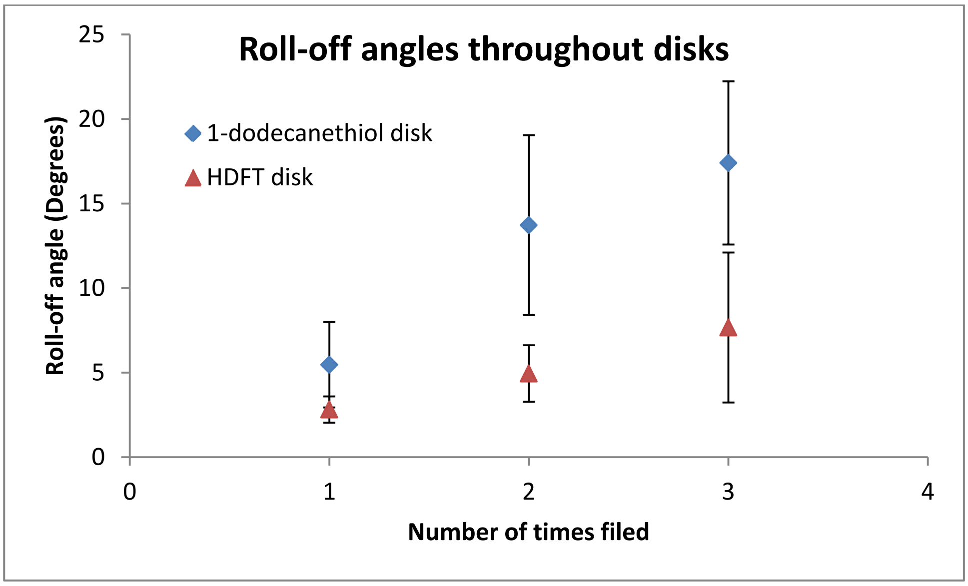

Figure 77: Roll-off angles throughout 1-dodecanethiol and HDFT treated disks

The fluorinated thiol treated disk shows a lower roll-off angle on the second and third filings than the 1-dodecanethiol treated material. This assertion must be treated with extreme caution however, since roll-off angle was shown to change with depth as one goes through the 1-dodecanethiol disk prepared using this preparation procedure. The number of times the material has been abraded gives some indication of depth travelled through the disk, but the depths travelled will not be exactly the same in both cases.

From this investigation it can be concluded that the method of putting a superhydrophobic surface on titanium as outlined in Section 3.1 gives the best results out of the methods trialled here. The method outlined in Section 3.2.1 maintains the ecdysiastic characteristics of the materials but the roll-off angle values are compromised, while the method described in Section 3.2.2 gives neither of the desired characteristics of low roll-off angle or ecdysiastic nature.

3.2.3 Effect of Combining Superhydrophobic Copper Powder Mixed with Titanium 200 Mesh HDH Powder

The effect of incorporating titanium powder into superhydrophobic copper powder was also evaluated. Titanium 200 mesh HDH powder was sifted together with the 1-dodecanethiol treated superhydrophobic copper powder from Section 2.1.1 in varying weight percentages to make up 1.5g total batches. The mixed powder was then compressed for two minutes in a SPECAC 13mm evacuable pellet die at a pressure of *ca* 60MPa in a hydraulic press. After careful removal from the die, roll-off angle measurements for the disks were carried out as described in Section 2.3.2. The results of the roll-off angle trials are summarised in Figure 78.

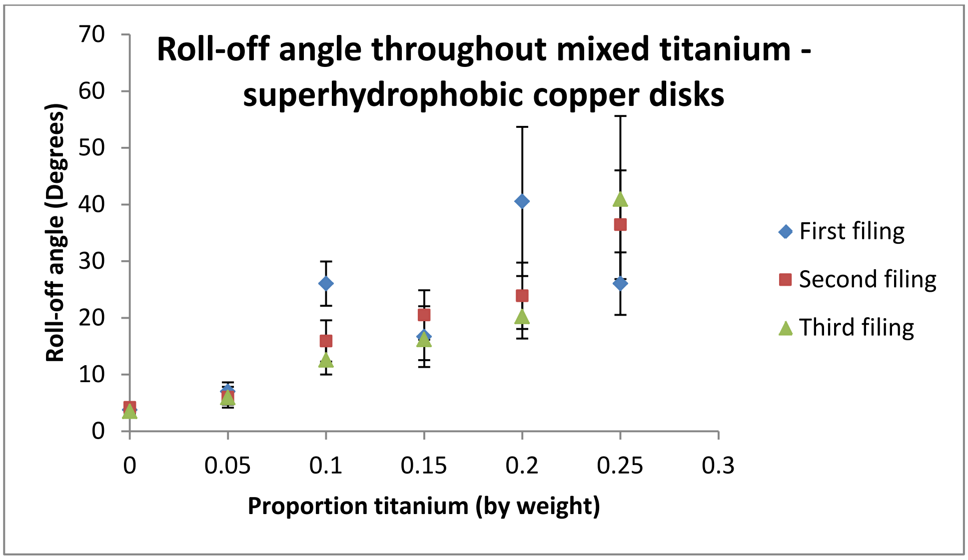

Figure 78: Ecdysiastic nature of mixed superhydrophobic copper/titanium disks

The addition of titanium to the superhydrophobic copper powder appears not to affect the ecdysiastic nature of the compressed disks, though errors associated with the measurements become very large. There is one data point for 10% weight titanium which is outside of the error margins for the other two points present, which is possibly indicative of an uneven composition of the compressed material, even though efforts were made to ensure the two powders were well mixed by sifting together.

The presence of hydrophilic titanium particles distributed amongst the superhydrophobic copper powder on the surface of the material may give rise to a multimodal roll-off angle distribution as seen on the some of the materials compressed to high pressures in Section 2.3.2.1. Histograms of all the normalised data were constructed in order to confirm the data is normally distributed as described in Section 2.3.2.1, and can be found in Appendix Five. The distributions show fairly close approximations to the normal distribution, though are skewed to the right. This, together with the fact that roll-off angles are for the most part constant throughout the material, indicates that the sifting method adequately mixes the two powders.

The one histogram that does stand out, however, is the histogram for the 10% titanium content material which is clearly bimodal (Figure 79). This is perhaps to be expected, as it contains the information for the one disk that did not have constant roll-off angles throughout (Figure 78).

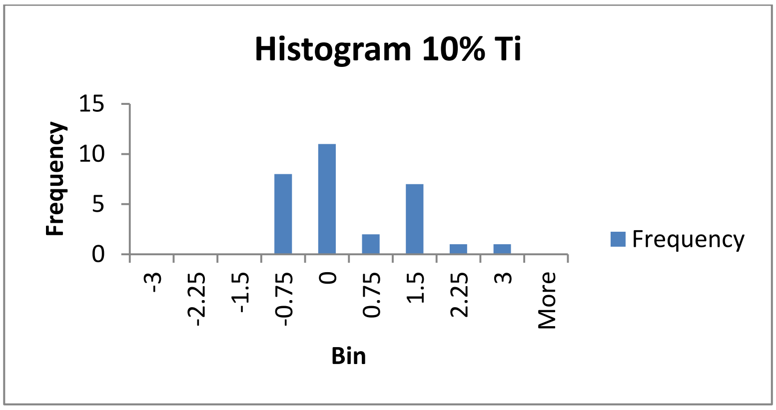

Figure 79: Histogram of z-scores for 10% titanium content disk

The fact that the roll-off angles were predominantly normally distributed and constant within experimental error throughout the materials allowed overall roll-off angles to be calculated for each disk. All thirty roll-off angles measured throughout each disk were combined and treated as one data set to give each disk an overall roll-off angle to discern the effect titanium addition to superhydrophobic ecdysiastic materials has on wetting characteristics.

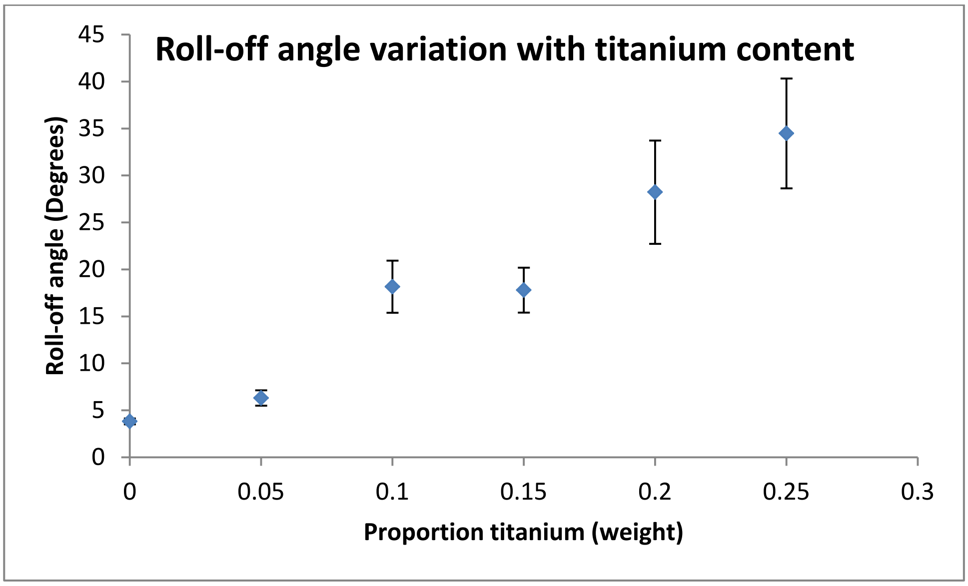

Figure 80: Roll-off angle variation with titanium content

An increase in titanium content for the superhydrophobic copper disks is shown in Figure 80 to adversely affect the superhydrophobic characteristics of the ecdysiastic materials. A clear increase in roll-off angle value is seen as titanium is added, together with an increase in the error associated with the measurement. Some of the variation in water roll-off angle values seen may arise from inaccuracies associated with using a hydraulic press to prepare these materials, although over a window of 20MPa to 100MPa roll-off angles varied only from *ca* 3.5° to *ca* 7° (Appendix One). This means that any errors associated with inaccurate pressures will not be large enough to affect the conclusions of this experiment, where roll-off angle ranges from *ca* 3.5° to *ca* 35° are seen.

3.3 Superhydrophobic Ecdysiastic Surfaces on Aluminium and Other Metals

3.3.1 Application to Aluminium

Aluminium is another industrially important metal which finds a great many engineering applications and forms a tenacious oxide coating which prevents its simple surface modification. The same procedure outlined in Section 3.1 to render titanium superhydrophobic was repeated, replacing the titanium powder with aluminium powder. A robust compact resulted from the die (Figure 81).

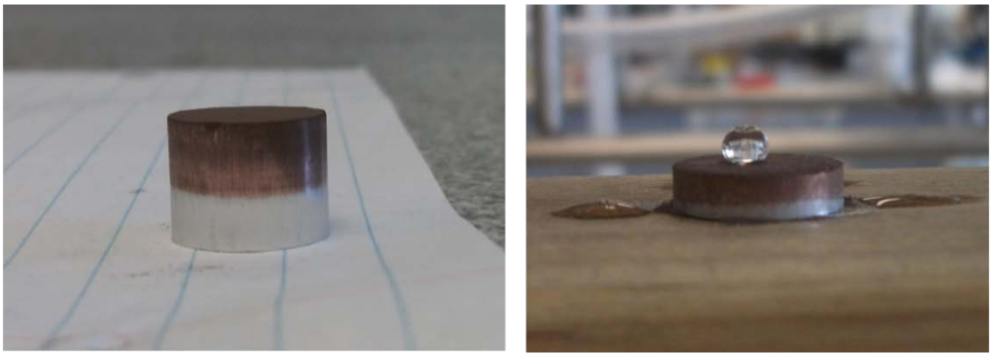

Figure 81: Superhydrophobic copper surface compressed onto an aluminium substrate

The roll-off angles of the resulting disk were assessed as described in Section 2.3.2. The results of the roll-off angle trials are summarised in Figure 82 below.

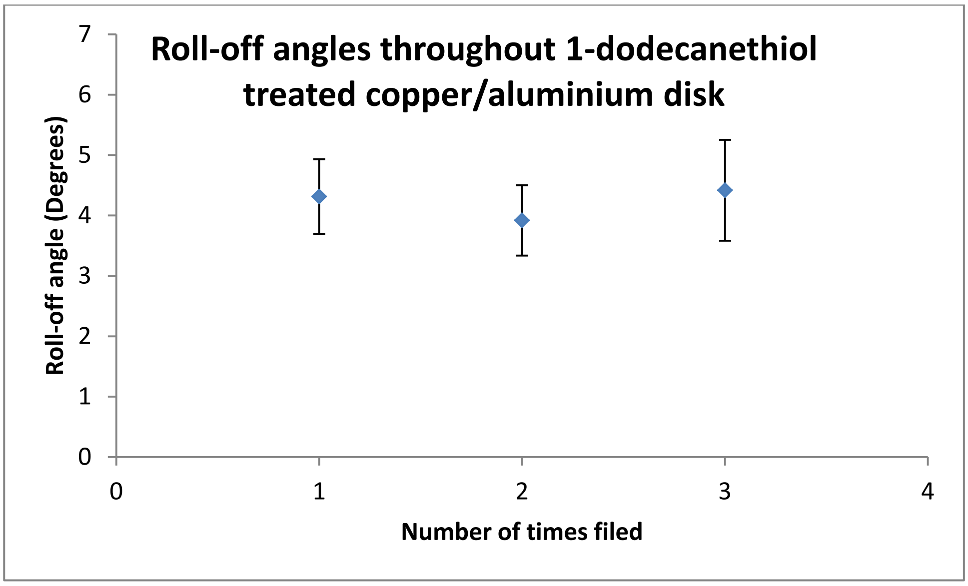

Figure 82: Roll-off angles throughout 1-dodecanethiol treated copper/aluminium disk

The roll-off angles measured throughout the superhydrophobic portions of the disks are consistent with one another within experimental error, which confirms the ecdysiastic nature of the material. All thirty roll-off angle measurements taken for the disk were treated as one data set to calculate an overall roll-off angle of 4.2±0.4˚. This is consistent with the roll-off angle of 3.8±0.3˚ which was calculated for the analogous disk composed of pure 1-dodecanethiol. These observations once again confirm the successful application of a superhydrophobic, ecdysiastic surface onto a chosen substrate.

3.3.2 Application to Other Substrates

A number of other substrates were attempted to be rendered superhydrophobic by this method, but the resulting compacts were very fragile and friable, so were of no practical use. These included nickel/aluminium alloy powder (BDH Chemicals Limited, England), silicon powder (BDH Chemicals, England) iron powder (Ajax Chemicals) and stainless steel powder (Adelaide Moulding Company).

4 Rendering Titanium Foil Superhydrophobic

The method that is employed in this work is once again an adaptation of the work carried out by Larmour *et al*[1] and is based on their superhydrophobic surfaces on copper foil. In their work, a rough layer of silver was galvanically deposited onto a copper foil followed by adsorption of a polyfluoroalkylthiol to lower the surface energy of the now roughened layer. The philosophy of the work carried out here is to apply a layer of copper over a titanium foil substrate, and then treat this in the same manner as they treated the copper foil (Figure 83).

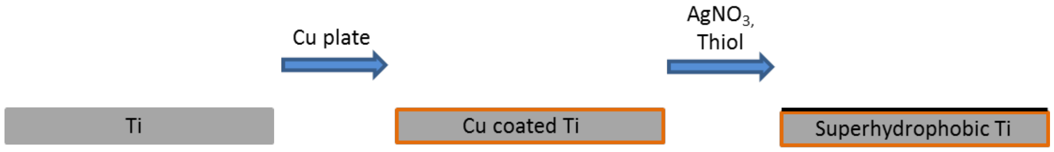

Figure 83: A schematic of the method used to render titanium foil superhydrophobic

4.1 Copper Plating of Titanium

The self-repairing oxide layer that forms on titanium is impervious and tightly adherent, and conditions required to remove it are often so harsh that the underlying freshly exposed metal reacts extremely quickly.[79] This makes getting an adherent electroplate onto titanium a very challenging task indeed.

In 1953 Colner, Feinleib and Reding[79] had some success in plating copper onto titanium utilising an anodic etch in a non-aqueous hydrofluoric acid-ethylene glycol bath before electroplating copper. Under the correct conditions, a rough surface was left on the titanium into which copper could deposit. It was concluded that the bond between the copper and the titanium was a mechanical one, so the texture of the titanium surface left after the etching treatment is of paramount importance in this method. Outside of the optimum conditions for etching the titanium foil was electropolished and smooth. Any copper deposits attempted on this surface were non-adherent, as this electropolished surface did not allow for these mechanical interactions between the titanium and the copper electroplate.

In 2007 von Gutfeld and West[80] reported an electrochemical method of plating copper onto Ti-6Al-4V alloy. The method involved a high voltage capacitor discharge across a copper electrolyte solution to destroy the oxide layer on the titanium electrode followed by an immediate electroplating of copper onto the titanium alloy. This method, however, suffered difficulties in providing a reproducibly adherent copper deposit. It was eventually decided to follow this route and experiment with different capacitances and voltages in an effort to try to find conditions that give a reliable and reproducible copper deposit.

4.1.1 Method for Electroplating of Copper

Titanium foil (2mm thick, 99.7%, Sigma-Aldrich) was cut into pieces of approximately 15mm x 20mm dimensions. After washing in distilled water followed by acetone these pieces served as the titanium cathodes. Copper anodes were cut to similar dimensions from copper foil (Technical Grade, 0.13mm thick, Ajax Chemicals), which were polished with a 3M Scotch Brite™ and washed in 1% nitric acid before use. Figure 84 schematically shows the circuit used in the electroplating procedure.

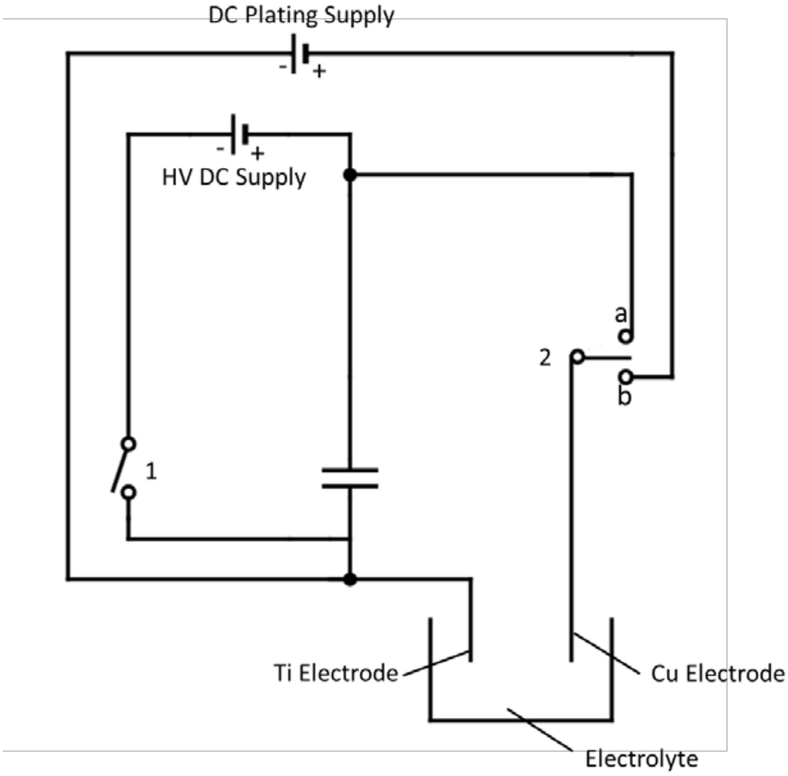

Figure 84: Circuit diagram for electroplating of copper onto titanium

The electrodes were partially submerged into an electrolyte solution of 0.24M copper sulfate in 1.8M sulfuric acid at distance of approximately 20mm apart, with approximately 400mm^2 immersed (two sides of 200mm^2) in solution.

All details reported here are in reference to Figure 84. Switches 1 and 2 were left open, and the chosen voltage to which the capacitor would be charged was set on the high voltage (HV) source (Metronix Regulated DC Power Supply, Model 652). The current to be supplied was set on the DC plating supply (Manson DC Power Supply, Model EP-613), which was run in constant current mode. To charge the capacitor, switch 2 was left in the open position and switch 1 was closed. Once current had stopped flowing and the capacitor was charged, switch 1 was opened. Switch 2 was then moved to position "a" to discharge the capacitor across the submerged electrodes in the solution. These last two steps were repeated a total of three times for three capacitor discharges across the solution. Switch 2 was then immediately moved to position "b" to apply a plating current of 40mA across the solution and deposit copper onto the titanium for seven minutes. Once the electroplating was complete, the titanium electrode was removed from the copper sulfate solution and rinsed with distilled water and dried with a paper towel.

Three different capacitance values were experimented with including 660µF, 1000µF and 4700µF. For each different experiment, the 660µF and 1000µF capacitors were charged up to voltages varying from 100V to 250V, increasing in 50V increments. The 4700µF capacitor was only charged to one voltage of 100V, its maximum safe rating.

The electroplating procedure deposited a copper coating onto the titanium on both sides of the foil where it had been submerged in the electrolyte solution. To assess how adherent the copper electroplate was, it was rubbed vigorously with a cloth, followed by the Scotch^{TM} tape test.[80] This test consists of pulling a piece of applied tape off the copper coating in both a vertical direction and then a tangential direction to the foil. If no copper was removed in any of these tests, the coating was deemed to be adherent. All of the procedures gave a copper deposit that would stand up to polishing of the surface with a cloth, but none passed the Scotch^{TM} tape test, where a force normal to the titanium substrate is applied to the deposited copper. All the copper coated titanium foils were then placed in a 120˚C oven for one hour and the adhesion tests were repeated on the other side of the foil to where they had been originally tested. Once again, all samples failed the Scotch^{TM} tape test.

4.1.2 Anodic Etching of Titanium Followed by Copper Deposition

In Colner *et al*'s work[79] on copper plating of titanium, they noted that on any of the adherent copper coatings they applied to titanium, there was a high degree of interlocking between the etched titanium base layer and the copper plate. They concluded that there was no special compound formed at the interface between the two metals, and that the binding interaction was a purely mechanical one. Due to the lack of success in achieving an adherent copper deposit onto a smooth titanium substrate in Section 4.1.1, a roughening step was introduced.

The same anodic etching conditions that Zhang *et al*[60] used in their method of rendering titanium superhydrophobic were used to roughen the titanium foil. In their work the anodic etching step introduced a series of titanium dioxide nanotubes at the titanium surface. It was hoped that copper could be deposited into the porous structure to allow a mechanical interlocking interaction between the base metal and the electroplated copper and hence yield an adherent copper deposit.

4.1.2.1 Anodic Etching Conditions

A titanium foil anode (2mm thick, 99.7%, Sigma-Aldrich) of 15mm x 20mm dimensions was washed with distilled water and acetone, then immersed in 50mL glycerol:water bath (75:25 volume%), to which 0.2938 grams of ammonium fluoride (AnalaR) was added. A copper foil (Technical Grade, 0.13mm thick, Ajax Chemicals) cathode of 15mmx20mm dimensions was polished with a 3M Scotch Brite^{TM} and washed in 1% nitric acid and also immersed in the solution approximately 10mm from the titanium anode and a potential of 20V applied (Figure 85). Both electrodes had approximately 400mm^2 surface area submerged in solution.

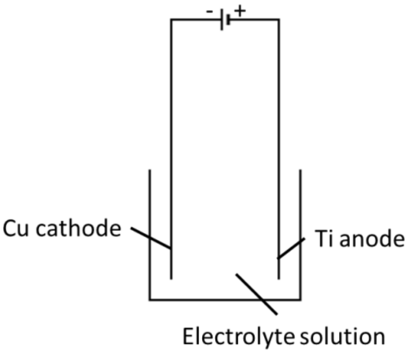

Figure 85: Circuit diagram for anodic titanium etch

The etching process was continued for three hours and the titanium foil was removed from solution before turning off the power source. The removed foil was then rinsed with distilled water and dried in a 120˚C oven for one hour. The etched portion of the foil shows an iridescent finish on removal from solution (Figure 86).

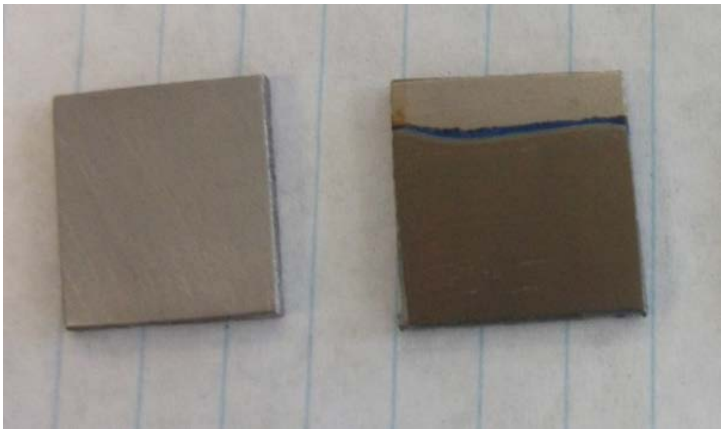

Figure 86: Un-etched titanium foil (left); etched titanium foil (right)

In order to confirm that the surface had indeed been roughened by the etching process, the etched foil was examined by SEM as described in Section 2.3.3.

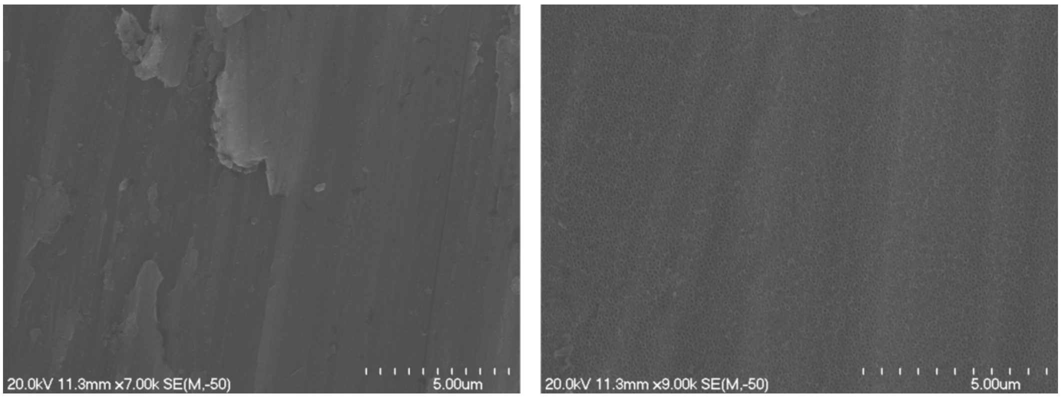

Figure 87: Un-etched titanium foil at 7000x magnification (left); etched titanium foil at 9000x magnification (right)

Figure 87 compares the topography of untreated titanium foil with its etched counterpart. The etched foil shows some evidence of pitting at this magnification, but at higher magnification the presence of the titanium dioxide nanotubes is easily seen on the etched titanium foil (Figure 88), indicating the etching process was successful.

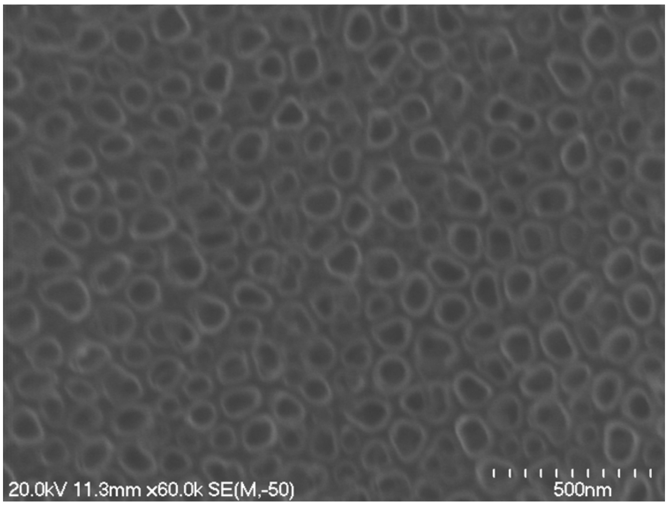

Figure 88: Titanium dioxide nanotubes at 60,000x magnification

4.1.2.2 Deposition of Copper onto Etched Titanium Foil

The etched portion of the titanium foil was immersed in 0.24M copper sulphate solution in 1.8M sulfuric acid. A copper anode was also placed into the solution and a plating current of 40mA was applied (Figure 89). The plating current was stopped after seven minutes, and the titanium foil removed, washed with distilled water and blotted dry. To the naked eye, there were visible areas where copper deposits appeared to nucleate from and the coating was not entirely uniform all over as appeared to be the case for the un-etched copper coated titanium foils.

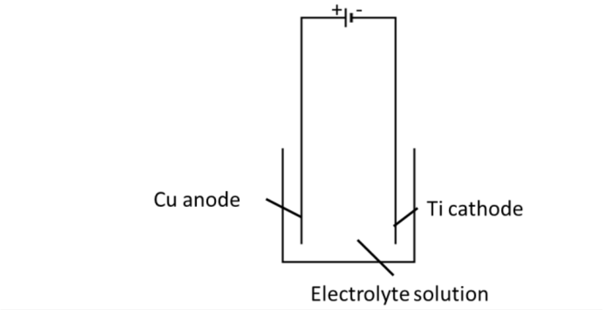

Figure 89: Circuit for electroplating copper onto etched titanium

The resultant foil was subjected to the adherence tests described in Section 4.1.1. The copper plate on the etched titanium foil failed the Scotch™ Tape test, but a far smaller portion of the copper came off than had been previously coming off in the tests described in Section 4.1.1 on the un-etched titanium foils. Moreover, any of the copper deposit that had come off had a black coating over it on the side that had been in contact with the titanium. The previous samples prepared in Section 4.1.1 were copper coloured on the side that had sheared away from the titanium in the Scotch™ Tape test (Figure 90). These observations suggest that the copper adheres well to the etched layer on the titanium, and now the limiting factor in its adherence is how strongly the etched layer is anchored to the titanium substrate.

Figure 90: Failed Scotch™ tape tests for un-etched titanium foil (left) and etched titanium foil (right)

The same etched and copper coated foil that failed the Scotch™ tape test was placed into a 120˚C oven for one hour and the Scotch™ Tape test was repeated on the other side of the foil. This time the copper deposit passed the test, so an adherent deposit had been successfully deposited using this method.

A second titanium foil was put through the anodic etching process followed by the copper electroplate as described above and placed in a 120˚C oven for one hour. The copper plate on both sides of this foil passed adherence tests. A third titanium foil was etched, plated and oven dried as above also, but this deposit failed the Scotch^{TM} tape test, indicating the method is not completely reliable and consistent. All of the copper deposits prepared in this etching method were qualitatively more adherent than those prepared using the method described in Section 4.1.1.

The capacitor discharge method is much quicker than the etching method and appears to give a more uniform copper coating. The downfall in the technique is that any copper coating it gives is rather weakly adherent to the titanium below. The etching method is time consuming and requires two electrolyte solutions to be prepared, but gives more robust coatings and does not require the high voltages and large capacitances that the capacitor discharge method uses.

4.2 Silver Coating and Thiol Treatment of Copper Coated Titanium Foil

A copper coated foil prepared as described in Section 4.1.2.2 was gently polished with a 3M Scotch Brite^{TM} and immersed in 0.02M aqueous silver nitrate solution for 40 seconds. The foil was then gently removed, immersed in distilled water and dried in a 40˚C oven. Once dry the foil was submerged in 0.01M HDFT solution in dichloromethane for one hour. Upon removal it was rinsed in dichloromethane and dried in a 40˚C oven.

This process was repeated on a second titanium foil which was copper coated as described in section 4.1.1 using a 660µF capacitance charged to a voltage of 250V followed by drying in a 120˚C oven for one hour. For a control, a copper foil (Technical Grade, 0.13mm thick, Ajax Chemicals) was also rendered superhydrophobic by this method.

4.2.1 SEM Investigation of Titanium Foils

The morphology of the treated foils was inspected by SEM to determine the nature of the copper coatings and silver deposits present on the foils. Images were recorded as described in Section 2.3.3.

4.2.1.1 Un-etched Superhydrophobic Titanium Foils

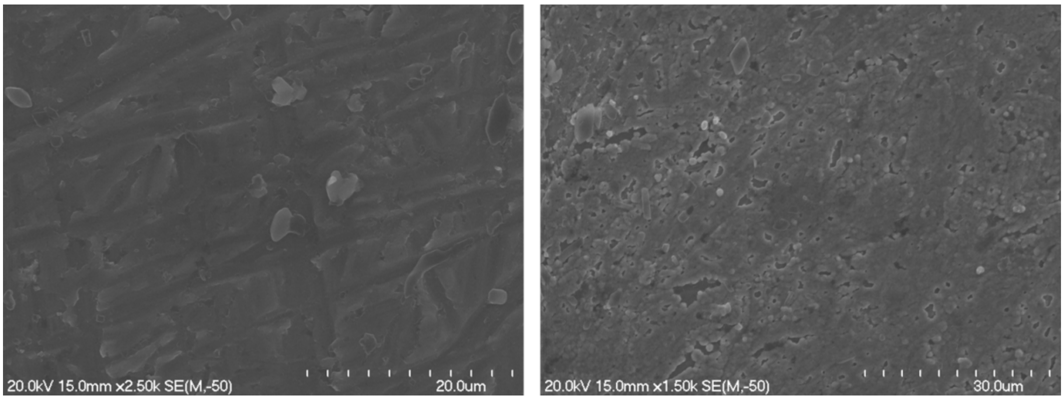

Figure 91: Untreated titanium foil at 2500x magnification (left); copper coated titanium foil at 1500x magnification (right)

Figure 91 shows that the copper plate on the titanium foil does not give a full coverage, and there are some small imperfections present in the coating. It is also seen to deposit in a reasonably smooth layer.

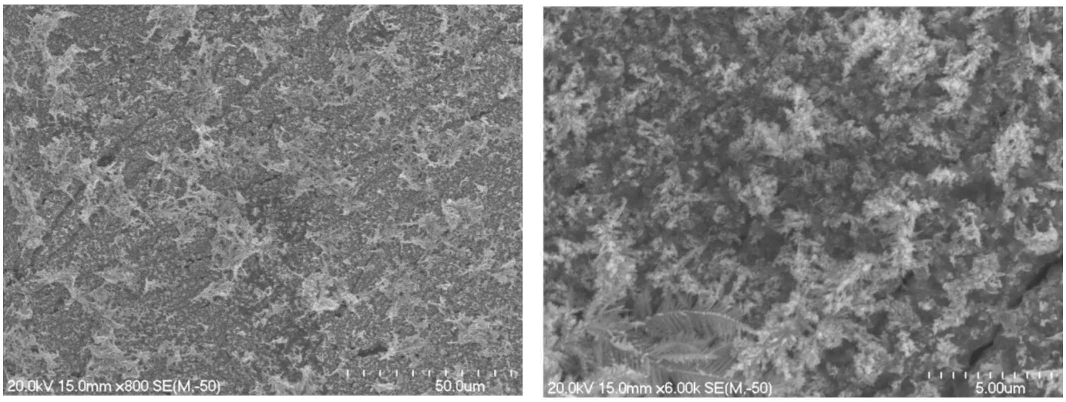

Figure 92: Silver deposits on titanium at 800x magnification (left) and 6000x magnification (right)

Figure 92 shows a remarkable transformation of the surface morphology on the deposition of silver. The dendritic structure of the silver deposits is evident on the higher magnification image, whose presence gives the micro- and nanoscale structures desired in preparing superhydrophobic surfaces.

4.2.1.2 Etched Superhydrophobic Titanium Foils

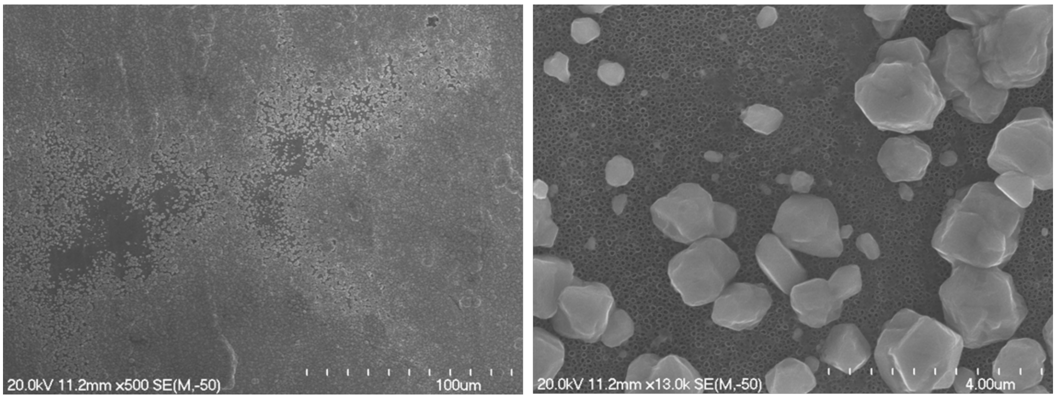

Figure 93: Copper deposits on etched titanium foil at 500x magnification (left) and 13,000x magnification (right)

Figure 93 shows the copper plating to be non-uniform on the etched foils. The higher magnification image appears to give some evidence of copper depositing into the pores present on the surface, although the copper deposits in general look to be much larger than the titanium dioxide nanotubes left after etching.

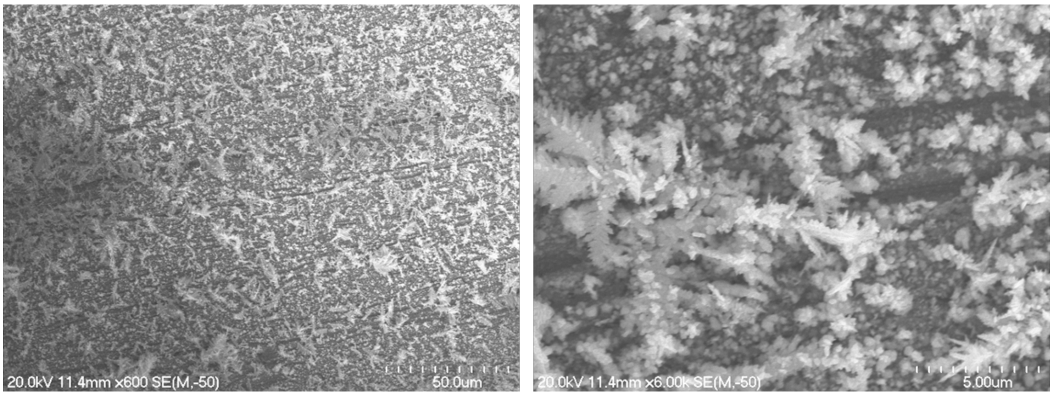

Figure 94: Silver deposits on superhydrophobic titanium at 600x magnification (left) and 6,000x magnification (right)

The superhydrophobic titanium foils prepared by the etching method are very similar in appearance to those prepared by the electrochemical method in Figure 94. The dendritic silver deposits show features in the micrometre and nanometre size domain to give the dual-scale roughness desired in superhydrophobic surface preparation and are clearly evident in the above images.

4.3 Assessment of Superhydrophobicity

4.3.1 Roll-off Angles

Initial attempts to record a water roll-off angle were fraught with issues of water droplets rolling off before any useful measurement was able to be made. If the water was able to be kept still on the surface for a roll-off angle trial to be carried out, it was invariably on an imperfection of the surface, and therefore not indicative of the bulk characteristics of the material.

In order to avoid this problem, roll-off angles were measured using glycerol rather than water, and glycerol proved to be a far easier material to work with due to the applied droplet moving much more slowly across the surface. To measure the roll-off angles of the superhydrophobic titanium foils, the foils were placed onto the roll-off angle measuring device (Figure 28) and a 20μL droplet of glycerol was placed with an autopipette onto the foil to be tested. The angle of the top platform of the roll-off angle measuring device was gently raised using a lab jack until the glycerol began to move across the surface. The height of the platform at front and rear was read and from there a roll-off angle was calculated. This was repeated five times, the foil rotated 180˚ so as to remove any bias from any slope associated with the shape of the foil, and the procedure repeated five more times. All ten measurements in total for each foil were averaged and 95% confidence intervals calculated to give an estimate of uncertainty. The results of the roll-off angle trials are shown in Table 7 below.

Table 7: Glycerol roll-off angles

	Roll-off angle (Degrees)
HDFT Copper foil	1.1±0.3
HDFT Etched Ti	0.6±0.2
HDFT Electroplated Ti	0.7±0.2

The roll-off angles for glycerol on the treated titanium foils are within experimental error of the superhydrophobic copper foil, and all roll-off angles are in the vicinity of 1˚ or less. Moreover, the two different superhydrophobic titanium preparations show practically identical roll-off angles and associated errors. The superhydrophobic copper foils that had been prepared in this manner by Larmour[1] were reported to have a WCA of 173±1˚, and a water roll-off angle of 0.64±0.04°. The superhydrophobic titanium foils here show the same roll-off angle within experimental error for glycerol as the straight superhydrophobic copper foil, which was prepared as Larmour[1] had reported. One can therefore extrapolate that a surface of the same superhydrophobic qualities has been grafted onto titanium based on the materials used, methods employed and data present here. If this is the case, these materials show a lower water roll-off angle value than is seen on any of the superhydrophobic ecdysiastic materials in Section 1 and Section 2. This is attributable to the titanium foil offering a much flatter, homogeneous substrate for the superhydrophobic surface to be prepared on than copper powder, allowing a far more consistent coating to be prepared. Also, no abrasion process has been carried out on this material so all of the small-scale structures that are so important in superhydrophobic surface preparations are as undisturbed as possible.

Glycerol has a lower surface tension than water does at 63mNm^{-1} and a higher density of 1.2gcm^{-3}.[76] In order to gain some insight into how a roll-off angle for glycerol would correlate to a roll-off angle for water, a series of values were substituted into Equation 11 from Section 1.2.3.3.

$$\gamma_{LV}(cos\theta_r - cos\theta_a) = \frac{mg}{w} sin\theta_{ro} \dots\dots\dots (11)$$

An estimated width (w) of contact a 20μL droplet of glycerol or water makes with the surface of 2.0mm (Figure 95) was used in all calculations and it was assumed the two substances would adopt the same shape on the surface also. Table 8 shows the calculated roll-off angles for 20μL droplets of each of water and glycerol with two contact angle hysteresis ranges.

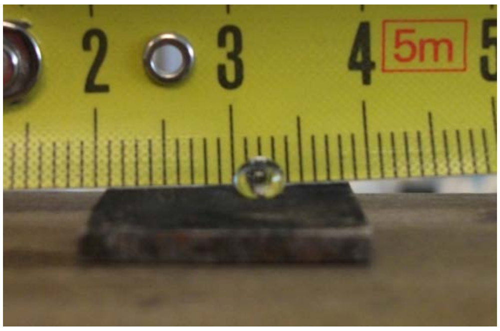

Figure 95: A 20μL glycerol droplet on a superhydrophobic titanium surface. Scale bars in the background are 1mm apart

Table 8: Calculated roll-off angle estimates

	θ_r (Degrees)	θ_a (Degrees)	Calculated θ_{ro} (Degrees)
Water	170	175	0.49
	165	175	1.29
Glycerol	170	175	0.34
	165	175	0.92

Using the assumption of a 2mm contact width with the surface for the droplets, a contact angle hysteresis range θ_r/θ_a of 170˚/175˚ underestimates the roll-off angles of both water in Larmour's work and the glycerol roll-off angles recorded here (Table 7). A larger estimate of contact angle hysteresis range θ_r/θ_a of 165˚/175˚ overestimates the roll-off angle value of water in Larmour's work, but fits in reasonably well with the observed roll-off angle data seen for glycerol in this work. Comparison of the data in Table 8 and Table 7 shows that the calculated glycerol roll-off angle using the larger contact angle hysteresis range θ_r/θ_a of 165˚/175˚ is consistent with the value seen on the HDFT treated copper foil, and is only barely above the margin of error for the two superhydrophobic titanium foils. From this comparison it can be concluded that the superhydrophobic titanium foils show a low contact angle hysteresis range and high contact angles for glycerol, which should also apply for water.

4.3.1.1 Comparison with 1-dodecanethiol Treated Foil

A 1-dodecanethiol treated superhydrophobic copper foil was prepared using an etched and copper coated foil which was prepared as described in Section 4.1.2. This foil was immersed in 0.02M aqueous silver nitrate for 40 seconds, rinsed in distilled water and dried in a 40˚C oven. Once dry, it was submerged in 0.1M 1-dodecanethiol solution in dichloromethane for one hour, removed and washed in dichloromethane and dried in a 40˚C oven. The same glycerol roll-off angle measurement process described in Section 4.3.1 was carried out on the 1-dodecanethiol treated foil, which gave a roll-off angle of 3.5±0.7˚. The results of all of the roll-off angle trials are summarised graphically in Figure 96.

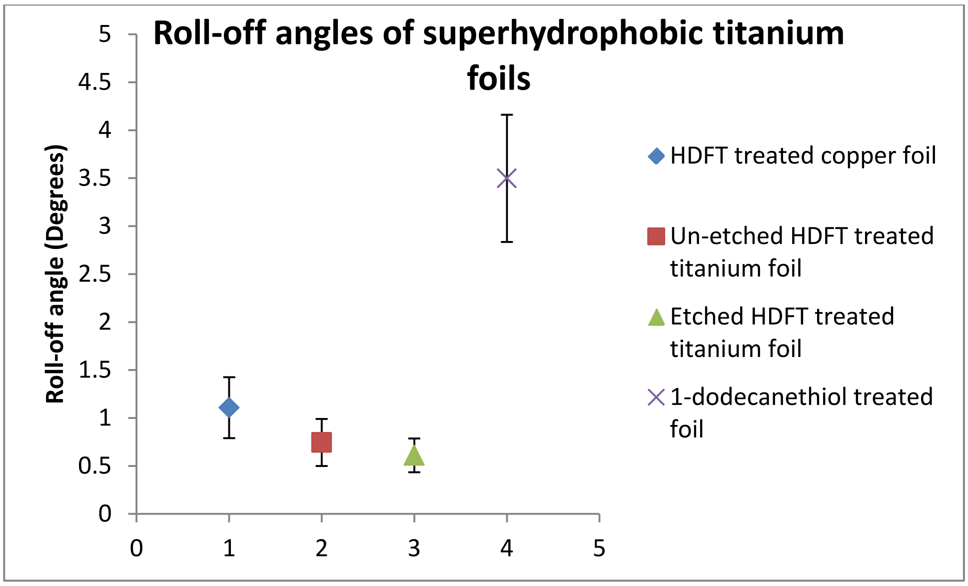

Figure 96: Roll-off angles of superhydrophobic titanium foils

The 1-dodecanethiol treatment clearly shows a larger roll-off angle than the HDFT treatment in this instance at the 95% confidence level. This may be attributed to the HDFT treated foil having a slightly lower surface energy than its alkyl chained counterpart, although the difference in roll-off angle seen is rather large when considering such a subtle difference in materials.

4.3.2 Qualitative Interactions with Water

Figure 97 shows a water droplet of the same 20µL volume on a variety of surfaces prepared based on titanium foil. The water appears to take a very similar form on the untreated titanium foil and the copper coated foil, but is seen to spread over a large area on the etched titanium foil.

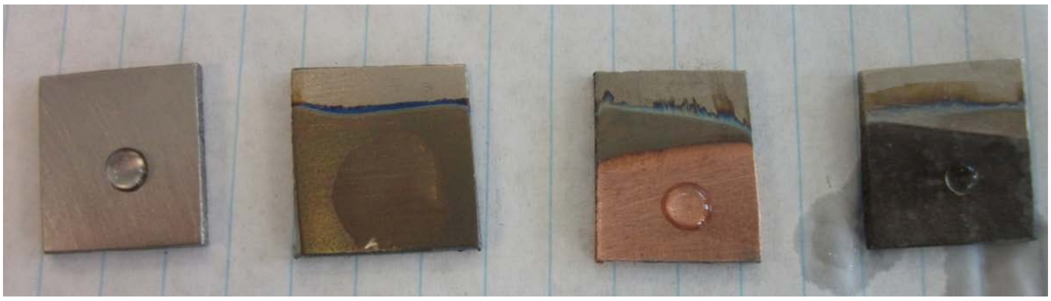

Figure 97: 20µL water droplet on, from left to right, untreated titanium; etched titanium; copper coated etched titanium; superhydrophobic HDFT treated titanium

This observation is consistent with the water conforming to the Wenzel wetting regime in this case. The water initially spread on the untreated titanium foil, and the roughening that results from the etching step is seen to amplify the hydrophilicity of the material. The water droplet applied to the superhydrophobic surface on titanium is seen to bead up into a spherical shape.

The superhydrophobic titanium foils showed a number of interesting qualitative characteristics that were seen in the work carried out by Larmour *et al*[1] with their superhydrophobic copper samples. Submerging the superhydrophobic titanium foil was also seen to induce a drastic distortion in the meniscus of the water, seen below in Figure 98.

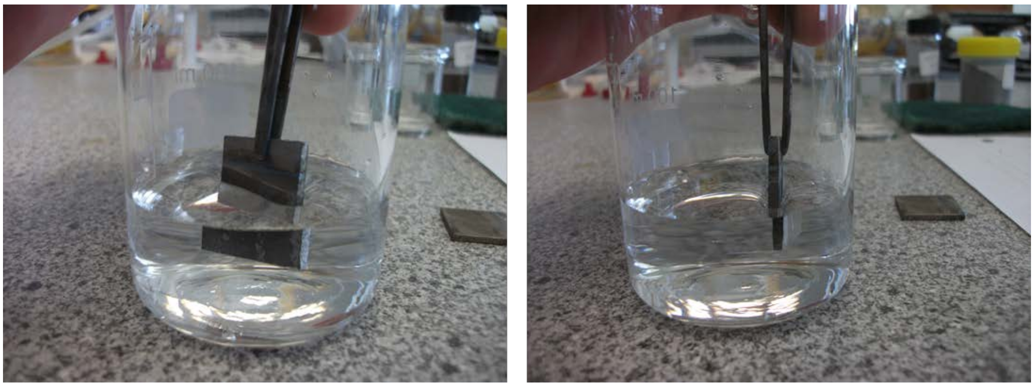

Figure 98: Superhydrophobic HDFT treated titanium surface distorting water meniscus

A most striking characteristic was the appearance of the foils, which are matt-black in appearance, to adopt a mirror like finish when tilted from the observer past the angle of reflection at an air-water interface (Figure 99). Plainly visible on the tilted foil in Figure 99 is the reflection of the scale on the side of the beaker it is submerged in. This is indicative of a layer of air between the water and the surface and hence the surface conforming to the Cassie-Baxter interaction with water. A freshly exposed surface of one the ecdysiastic superhydrophobic materials from Section 2 was seen to show the same behaviour when submerged in water also.

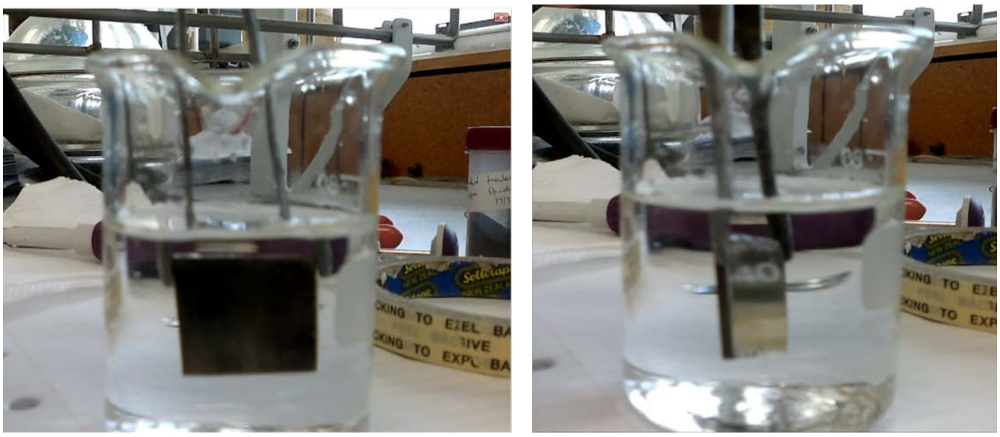

Figure 99: Submerged superhydrophobic HDFT treated titanium foil (left); tilted past angle of reflection at an air-water interface (right)

The method of rendering titanium superhydrophobic by inducing a roughness with femtosecond laser ablation[2] described in Section 1.4.2 was seen to revert from a partly Cassie-Baxter regime to predominantly a Wenzel wetting regime after one hour immersion in water. One of the superhydrophobic titanium foils was immersed in distilled water and photographs were taken over time to assess the stability of the air layer in between the water and the surface.

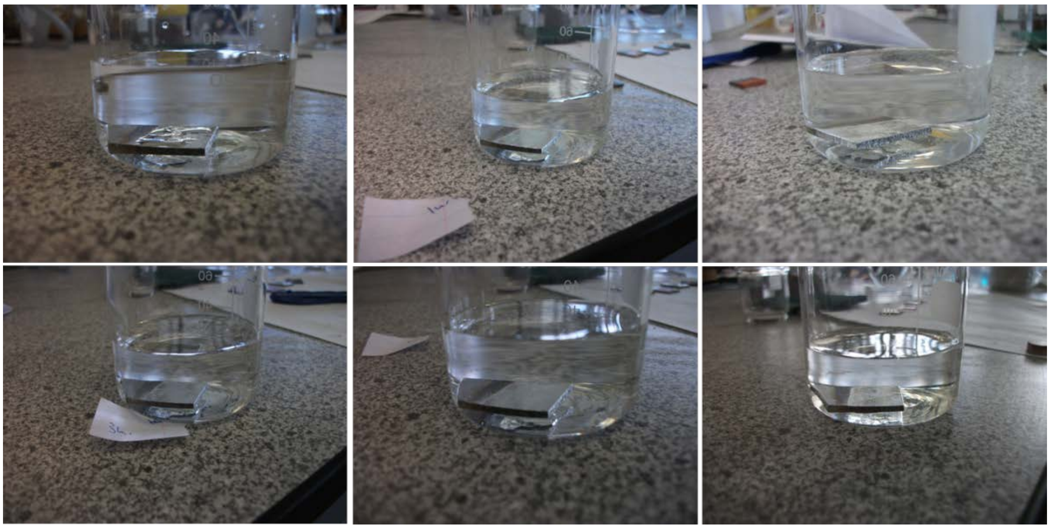

Figure 100: Silver mirror appearance of submerged superhydrophobic HDFT treated titanium foil over time, clockwise from top left, one minute immersion time; one hour; two hours; three hours; 24 hours; 72 hours

Figure 100 shows the silver mirror, and hence the layer of air between the water and the surface, is stable over the three day time period the foil was observed for. The above photographs show that the non-wetted state of this superhydrophobic titanium preparation is far more stable than that seen prepared by the femtosecond laser ablation method. This stability of the non-wetted Cassie-Baxter state is an important characteristic in that many of the benefits that are seen in superhydrophobic surfaces including self-cleaning, drag reduction in water and resistance to bio-fouling are dependent on keeping water off of a submerged surface.

5 Conclusions and Ideas for Further Work

5.1 Superhydrophobic Ecdysiastic Materials

The study on the effect pressure has on the superhydrophobicity of these ecdysiastic materials has demonstrated that the superhydrophobic qualities of the materials are adversely affected once the material has been compressed to the point of bulk plastic deformation. Compression time does not appear to affect the wetting characteristics of the materials, though a very short compression time does result in fragile compacts. The superhydrophobicity of the compacts was compromised by subjecting to temperatures in the vicinity of 100˚C which rules out the introduction of sintering as a process to impart strength to the materials. All of the variations in compression pressure, compression time and temperatures the disks were subjected to were shown not to affect the ecdysiastic nature of the materials.

No measurable difference was seen between the HDFT treated materials and the 1-dodecanethiol treated materials with regards to overall roll-off angle on copper a copper substrate. There were two instances where the HDFT treated samples did not show ecdysiastic characteristics throughout their composition, however. The HDFT treated zinc compact was seen to have a higher roll-off angle than the 1-dodecanethiol treated counterpart also. These observations are perhaps attributable to the lower concentration of the more expensive HDFT used relative to 1-dodecanethiol in the experimental work. Experiments could be repeated with the same concentration of the two thiols to rule this out as a factor.

5.2 Superhydrophobic Ecdysiastic Materials on Other Metals

The superhydrophobic copper powder was successfully grafted onto both titanium and aluminium powders and retained its superhydrophobicity and ecdysiastic nature. Examination of titanium compacts showed that both mechanical interlocking of powder particles and localised plastic deformation are required for a stable compact to be formed at the compression pressures being utilised.

Changing the order of synthesis of the disks to allow a final step of thiol treatment resulted in materials which had either their superhydrophobicity compromised, or the ecdysiastic nature was compromised. This change of synthesis was attempted in order to see if a sintering process could be applicable to impart extra strength to the materials, but unfortunately the resulting products were not able to maintain their desired characteristics.

Combining titanium powder and superhydrophobic copper powder and then compressing it to form a compact was shown to yield an ecdysiastic material whose wetting behaviour was uniform throughout. Unfortunately the superhydrophobic characteristics of the material were compromised on addition of titanium, making this method not a viable one for rendering titanium superhydrophobic.

It seems that the limiting factor when it comes to rendering other materials superhydrophobic by this method is the pressure to which you can compress the superhydrophobic material without inducing bulk plastic deformation of the copper particles. If another base substrate could be found to replace copper which is much harder and resistant to plastic deformation, then it can be expected that the number of materials that can be rendered superhydrophobic by this approach would be broadened. There are two main requirements for the powders to be used for these ecdysiastic materials prepared in this fashion. These are that the powdered material must have irregular particle shape to allow mechanical interlocking of particles in a porous structure, and an appropriate redox potential to allow the galvanic reduction of silver onto it.   A suitable candidate to test this hypothesis would be brass, an alloy of copper and zinc, which is harder than either of the pure metals, both of which have suitable redox potentials for galvanic deposition of silver.

5.3 Rendering Titanium Foil Superhydrophobic

The main difficulty in this strategy was encountered when the deposition of an adherent copper coating was attempted. Two methods were attempted, neither of which was found to be completely reliable in giving an adherent copper deposit. The capacitor discharge method followed by immediate copper plating tried was rapid, but none of the prepared electroplates were robust to an upwards force which was applied in the Scotch^{TM} Tape test. The etch then electroplate method was time consuming but gave more strongly adherent copper deposits, some of which stood up to the Scotch^{TM} Tape test, but was not entirely consistent.

Once coated in copper the titanium foils were very simple to render superhydrophobic. The resultant superhydrophobic titanium foils were so difficult to record a roll-off angle with water that measurements were performed using glycerol. These foils gave the same glycerol roll-off angles as those seen on purely superhydrophobic copper foils prepared as in Larmour's previous study[1] which were reported to have a WCA of 173±1° and a water roll-off angle of 0.64±0.04°. While this work has shown that roll-off angle data is useful in characterising the wetting characteristics of a surface, a study of WCA data, particularly advancing and receding contact angles, would be useful for comparison with other reported materials since this is a more commonly quoted characteristic of superhydrophobic materials.

A roll-off angle comparison of HDFT treated superhydrophobic titanium foils with a 1-dodecanethiol treated titanium foil showed that the HDFT treated products had lower glycerol roll-off angles of below 1°, while the 1-dodecanethiol treated foil showed a value of 3.5±0.7°. This can perhaps be attributed to the lower surface energy of the fluoroalkyl group compared to the alkyl group of 1-dodecanethiol, although the difference seen in roll-off angles seen was quite large for this to be the only factor.

The silver deposit that gives the roughness required for superhydrophobicity is very fragile, to the point that the relatively weak adherence of the copper layer to the titanium below is not the material's weak point. While the weakest point in the material is not the strength of the copper deposit, work can still be done in optimising copper electroplating techniques. The capacitor discharge method does not show much promise in getting reliable copper deposits, and time and resources would be better spent in optimising the etch and plate method.

References

(1) Larmour, I. A.; Bell, S. E. J.; Saunders, G. C. *Angewandte Chemie International Edition* **2007**, *46*, 1710-1712.

(2) Fadeeva, E.; Truong, V. K.; Stiesch, M.; Chichkov, B. N.; Crawford, R. J.; Wang, J.; Ivanova, E. P. *Langmuir* **2011**, *27*, 3012-3019.

(3) Gao, L.; McCarthy, T. J.; Zhang, X. *Langmuir* **2009**, *25*, 14100-14104.

(4) Chao-Hua, X.; Shun-Tian, J.; Jing, Z.; Li-Quiang, T.; Hong-Zheng, C.; Mang, W. *Science and Technology of Advanced Materials* **2008**, *9*, 035008.

(5) Barkhudarov, P. M.; Shah, P. B.; Watkins, E. B.; Doshi, D. A.; Brinker, C. J.; Majewski, J. *Corrosion Science* **2008**, *50*, 897-902.

(6) Rothstein, J. P. *Annual Review of Fluid Mechanics* **2010**, *42*, 89-109.

(7) Marmur, A. *Annual Review of Materials Research* **2009**, *39*, 473-489.

(8) Li, X.-M.; Reinhoudt, D.; Crego-Calama, M. *Chemical Society Reviews* **2007**, *36*, 1350-1368.

(9) Barthlott, W.; Neinhuis, C. *Planta* **1997**, *202*, 1-8.

(10) Shirtcliffe, N. J.; McHale, G.; Atherton, S.; Newton, M. I. *Advances in Colloid and Interface Science* **2010**, *161*, 124-138.

(11) Sun, T.; Feng, L.; Gao, X.; Jiang, L. *Accounts of Chemical Research* **2005**, *38*, 644-652.

(12) Parker, A. R.; Lawrence, C. R. *Nature* **2001**, *414*, 33-34.

(13) Bormashenko, E.; Bormashenko, Y.; Stein, T.; Whyman, G.; Bormashenko, E. *Journal of Colloid and Interface Science* **2007**, *311*, 212-216.

(14) Butt, H. J.; Graf, K.; Kappl, F. *Physics and Chemistry of Interfaces*; Wiley-VCH, 2003.

(15) Reid, T.; P, E. *Physical Chemistry*; Pearson Benjamin Cummings, 2006.

(16) Quere, D. *Annual Review of Materials Research* **2008**, *38*, 71-99.

(17) Young, T. *Philisophical Transactions of the Royal Society of London* **1805**, *95*, 65-87.

(18) Barbieri, L. W., E.; Hoffmann,P. *Langmuir* **2007**, *23*, 1723-1734.

(19) de Gennes, P.-G.; Brocherd-Wyart, F.; Quere, D. *Capillarity and Wetting Phenomena; Drops, Bubbles, Pearls, Waves*; Springer: New York, 2003.

(20) Wenzel, R. N. *Industrial & Engineering Chemistry* **1936**, *28*, 988-994.

(21) Cassie, A. B. D. B., S. *Trans. Faraday. Soc.* **1944**, *40*.

(22) Kim, S. H. *Journal of Adhesion Science & Technology* **2008**, *22*, 235-250.

(23) Roach, P.; Shirtcliffe, N. J.; Newton, M. I. *Soft Matter* **2008**, *4*, 224-240.

(24) Larmour, I. A.; Saunders, G. C.; Bell, S. E. J. *New Journal of Chemistry* **2008**, *32*, 1215-1220.

(25) Gao, L.; McCarthy, T. J. *Langmuir* **2007**, *23*, 3762-3765.

(26) McHale, G. *Langmuir* **2007**, *23*, 8200-8205.

(27) Gao, L.; McCarthy, T. J. *Langmuir* **2009**, *25*, 14105-14115.

(28) Zimmermann, J.; Seeger, S.; Reifler, F. A. *Textile Research Journal* **2009**, *79(17)*, 1565-1570.

(29) Marmur, A. *Soft Matter* **2006**, *2*, 12-17.

(30) Nosonovsky, M.; Bhushan, B. *Current Opinion in Colloid & Interface Science* **2009**, *14*, 270-280.

(31) Bartell, F. E.; Shepard, J. W. *The Journal of Physical Chemistry* **1953**, *57*, 211-215.

(32) Morra, M.; Occhiello, E.; Garbassi, F. *Langmuir* **1989**, *5*, 872-876.

(33) Zhang, J.; Li, J.; Han, Y. *Macromolecular Rapid Communications* **2004**, *25*, 1105-1108.

(34) Shirtcliffe, N. J.; McHale, G.; Newton, M. I.; Perry, C. C.; Roach, P. *Chemical Communications* **2005**, 3135-3137.

(35) Sun, M.; Luo, C.; Xu, L.; Ji, H.; Ouyang, Q.; Yu, D.; Chen, Y. *Langmuir* **2005**, *21*, 8978-8981.

(36) Feng, X.; Zhai, J.; Jiang, L. *Angewandte Chemie International Edition* **2005**, *44*, 5115-5118.

(37) Feng, X.; Feng, L.; Jin, M.; Zhai, J.; Jiang, L.; Zhu, D. *Journal of the American Chemical Society* **2003**, *126*, 62-63.

(38) Ma, M.; Hill, R. M. *Current Opinion in Colloid & Interface Science* **2006**, *11*, 193-202.

(39) Teshima, K.; Sugimura, H.; Inoue, Y.; Takai, O.; Takano, A. *Applied Surface Science* **2005**, *244*, 619-622.

(40) Balu, B.; Breedveld, V.; Hess, D. W. *Langmuir* **2008**, *24*, 4785-4790.

(41) Callies, M.; Chen, Y.; Marty, F.; Pepin, A.; Quere, D. *Microelectronic Engineering* **2005**, *78-79*, 100-105.

(42) Bhushan, B.; Nosonovsky, M.; Chae Jung, Y. *Journal of The Royal Society Interface* **2007**, *4*, 643-648.

(43) Shibuichi, S.; Yamamoto, T.; Onda, T.; Tsujii, K. *Journal of Colloid and Interface Science* **1998**, *208*, 287-294.

(44) Qian, B.; Shen, Z. *Langmuir* **2005**, *21*, 9007-9009.

(45) Liu, T.; Yin, Y.; Chen, S.; Chang, X.; Cheng, S. *Electrochimica Acta* **2007**, *52*, 3709-3713.

(46) Wang, Y.; Wang, W.; Zhong, L.; Wang, J.; Jiang, Q.; Guo, X. *Applied Surface Science* **2010**, *256*, 3837-3840.

(47) Fu, X.; He, X. *Applied Surface Science* **2008**, *255*, 1776-1781.

(48) Neto, C.; Joseph, K. R.; Brant, W. R. *Physical Chemistry Chemical Physics* **2009**, *11*, 9537-9544.

(49) Jiang, L.; Zhao, Y.; Zhai, J. *Angewandte Chemie International Edition* **2004**, *43*, 4338-4341.

(50) Han, D.; Steckl, A. J. *Langmuir* **2009**, *25*, 9454-9462.

(51) Matsumoto, Y.; Ishida, M. *Sensors and Actuators A: Physical* **2000**, *83*, 179-185.

(52) Chen, S.; Hu, C.; Chen, L.; Xu, N. *Chemical Communications* **2007**, 1919-1921.

(53) Xu, X. H.; Zhang, Z. Z.; Yang, J.; Zhu, X. *Colloids and Surfaces A: Physicochemical and Engineering Aspects* **2011**, *377*, 70-75.

(54) Leyens, C.; Peters, M. *Titanium and Titanium Alloys - Fundamentals and Applications*; WILEY-VCH Verlag GmbH & Co. KGaA: Weinheim, 2003.

(55) Cotton, F. A.; Wilkinson, G.; Murillo, C. A.; Bochmann, M. *Advanced Inorganic Chemistry, 6th Edition*; John Wiley & Sons, Inc: New York, 1999.

(56) Greenwood, N. N.; Earnshaw, A. *Chemistry of the Elements*; Pergamon: Oxford, 1984.

(57) Limited, T. N. Z. S. I. C. *Report of the New Zealand Steel Investigating Company Limited*; R.E. Owen, Government Printer, Wellington, New Zealand: Wellington, 1963.

(58) Kear, D. *Geology of Ironsand Resources of New Zealand*; Department of Scientific and Industrial Research, 1979.

(59) Christie, T.; Brathwait, B. *Mineral Commodity Report 16 - Titanium*, Institute of Geological and Nuclear Sciences Ltd.

(60) Zhang, F.; Chen, S.; Dong, L.; Lei, Y.; Liu, T.; Yin, Y. *Applied Surface Science* **2011**, *257*, 2587-2591.

(61) Fadeev, A. Y.; McCarthy, T. J. *Langmuir* **2000**, *16*, 7268-7274.

(62) Lahann, J.; Mitragotri, S.; Tran, T. N.; Kaido, H. *Science* **2003**, *299*, 371-374.

(63) Hozumi, A.; Cheng, D. F.; Yagihashi, M. *Journal of Colloid and Interface Science* **2011**, *353*, 582-587.

(64) Jagdheesh, R.; Pathiraj, B.; Karatay, E.; Romer, G. R. B. E.; Huis in't Veld, A. J. *Langmuir* **2011**, *27*, 8464-8469.

(65) Larmour, I. A.; Saunders, G. C.; Bell, S. E. J. *ACS Applied Materials & Interfaces* **2010**, *2*, 2703-2706.

(66) de Garmo, E. P.; Black, J. T.; Kohser, R. A. *de Garmo's Materials & Processes in Manufacturing*; 10 ed.; John Wiley & Sons, 2008.

(67) Ulman, A. *Chemical Reviews* **1996**, *96*, 1533-1554.

(68) Ulman, A. *Chem. Rev.* **1996**, *96*, 1533-1554.

(69) Paik, W.-k.; Eu, S.; Lee, K.; Chon, S.; Kim, M. *Langmuir* **2000**, *16*, 10198-10205.

(70) Conley, R. T. *Infrared Spectroscopy* Allyn and Bacon, Inc.: Boston, 1972.

(71) Porter, M. D.; Bright, T. B.; Allara, D. L.; Chidsey, C. E. D. *Journal of the American Chemical Society* **1987**, *109*, 3559-3568.

(72) Frisch, M. J., Trucks, G.W., Schlegel, H.B., Scuseria, G.E., Robb, M.A., Cheeseman, J.R., Scalmani, G., Barone, V., Mennucci, B., Petersson, G.A., Nakatsuji, H., Caricato, M., Li, X., Hratchian, H.P., Izmaylov, A.F., Bloino, J., Zheng, G., Sonnenberg, J.L., Hada, M., Ehara,M., Toyota, K., Fukuda, R., Hasegawa, J., Ishida, M., Nakajima, T., Honda, Y., Kitao, O., Nakai, H., Vreven, T., Montgomery, Jr., J.A., Peralta, J.E., Ogliaro, F., Bearpark, M., Heyd, J.J., Brothers, E., Kudin, K.N., Staroverov, V.N., Kobayashi, R., Normand, J., Raghavachari, K., Rendell, A., Burant, J.C., Iyengar, S.S., Tomasi, J., Cossi, M., Rega, N., Millam, J.M., Klene, M., Knox, J.E., Cross, J.B., Bakken, V., Adamo, C., Jaramillo, J., Gomperts, R., Stratmann, R.E., Yazyev, O., Austin, A.J., Cammi, R., Pomelli, C., Ochterski, J.W., Martin, R.L., Morokuma, K., Zakrzewski, V.G., Voth, G.A., Salvador, P., Dannenberg, J.J., Dapprich, S., Daniels, A.D., Farkas, O., Foresman, J.B., Ortiz, J.V., Cioslowski, J. And Fox, D, J.; Revision A.02 ed.; Gaussian, Inc.: Wallingford, CT, 2009.

(73) Schlegel, H. B. *Journal of Computational Chemistry* **1982**, *3*, 214-218.

(74) O'Hagan, D. *Chemical Society Reviews* **2008**, *37*, 308-319.

(75) Spatz, C. *Basic Statistics - Tales of Distributions*; Wadsworth: Belmont, CA, 2011.

(76) *CRC Handbook of Chemistry and Physics*; 59 ed.; CRC Press, Inc.: Boca Raton, Florida, 1979.

(77) Carnavas, P. C.; Page, N. W. *Journal of Materials Science* **1998**, *33*, 4647-4655.

(78) Gerdemann, S.; Jablonski, P. *Metallurgical and Materials Transactions A* **2011**, *42*, 1325-1333.

(79) Colner, W. H.; Feinleib, M.; Reding, J. N. *Journal of The Electrochemical Society* **1953**, *100*, 485-489.

(80) von Gutfeld, R.; West, A. *Journal of Applied Electrochemistry* **2008**, *38*, 531-536.

Appendices

Appendix One: Roll-off Angle Data for Two Minute Compressed Disks

Pressure (MPa)	θ_{ro} 1st filing (Degrees)	θ_{ro} 2nd filing (Degrees)	θ_{ro} 3rd filing (Degrees)	θ_{ro} Average (Degrees)
22	4.0±1.4	4.5±1.0		4.3±0.8
27	5.0±1.4	4.1±0.7		4.6±0.7
33	3.8±0.8	4.2±0.8	3.7±1.0	3.9±0.4
38	5.3±0.7	4.6±1.3		4.9±0.7
44	4.7±1.1	4.2±1.1	3.6±0.6	4.2±0.5
51	3.1±0.5	3.7±0.8	3.4±0.7	3.4±0.3
59	3.8±0.5	4.2±0.8	3.5±0.4	3.8±0.3
65	4.7±1.1	5.2±1.4	5.0±2.0	5.0±0.6
73	5.1±0.7	6.0±1.4	5.4±2.3	5.5±0.8
88	4.7±0.9	6.0±1.2	7.0±2.6	5.9±0.9
100	6.5±1.2	6.7±1.8	6.8±2.0	6.7±0.9
120	7.5±1.2	11±3	11±2	9.7±1.4
130	10±2	14±2	24±7	16±3
150	17±3	17±6	15±3	17±2
180	29±9	35±10	29±9	31±5

Appendix Two: Histograms of z-scores for Two Minute Compressed 1-Dodecanethiol Treated Disks

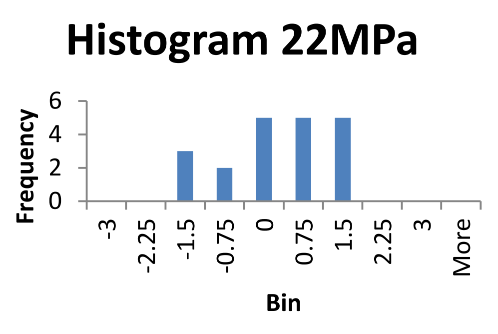

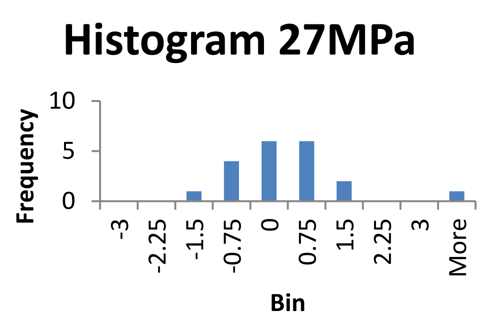

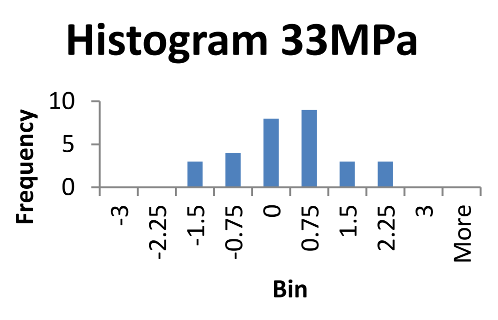

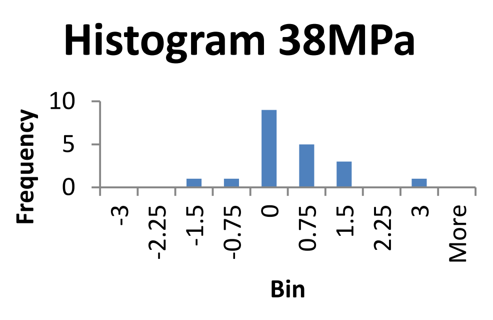

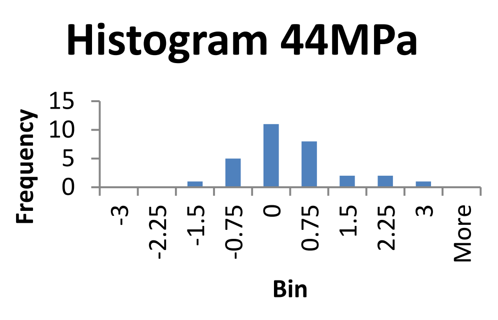

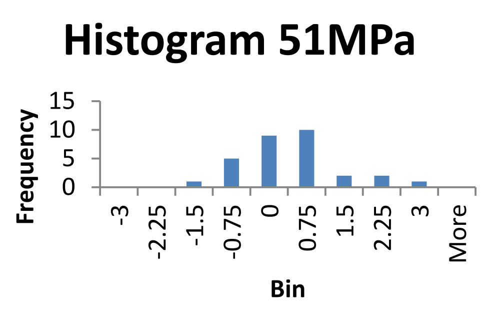

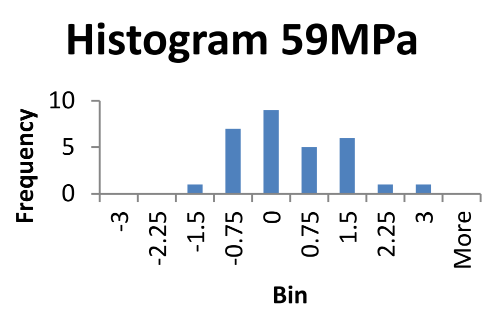

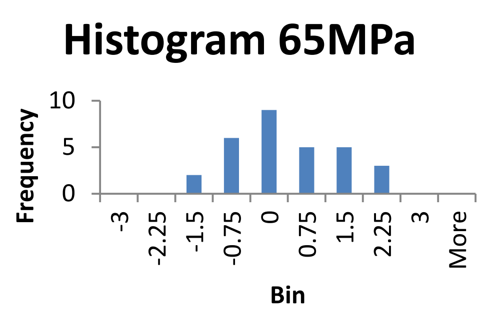

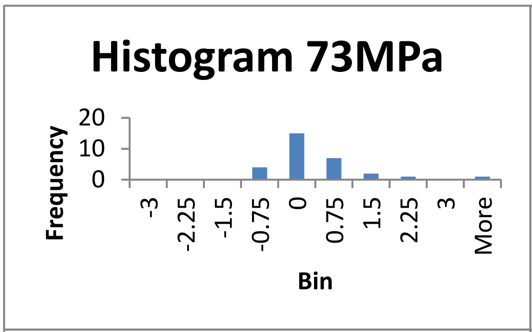
Histogram 73MPa
Frequency
20
10
0
-3
-2.25
-1.5
-0.75
0
0.75
1.5
2.25
3
More
Bin

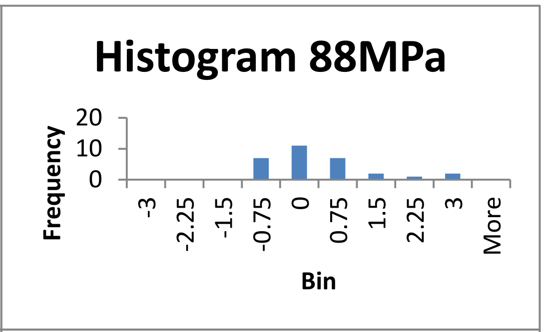
Histogram 88MPa
Frequency
20
10
0
-3
-2.25
-1.5
-0.75
0
0.75
1.5
2.25
3
More
Bin

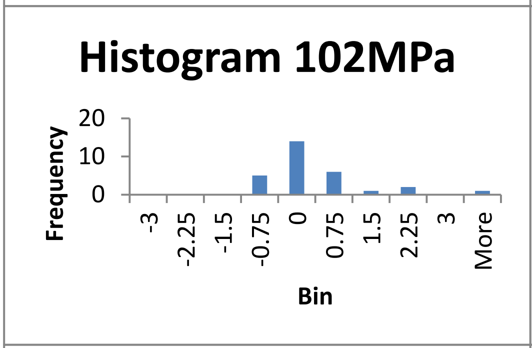
Histogram 102MPa
Frequency
20
10
0
-3
-2.25
-1.5
-0.75
0
0.75
1.5
2.25
3
More
Bin

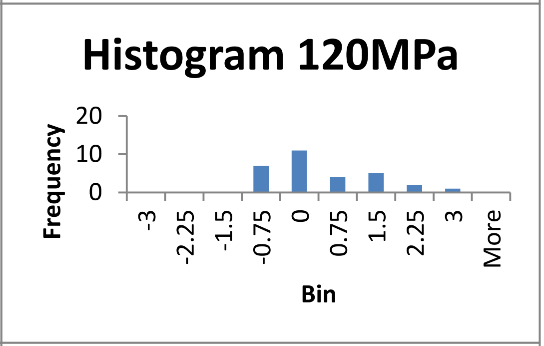
Histogram 120MPa
Frequency
20
10
0
-3
-2.25
-1.5
-0.75
0
0.75
1.5
2.25
3
More
Bin

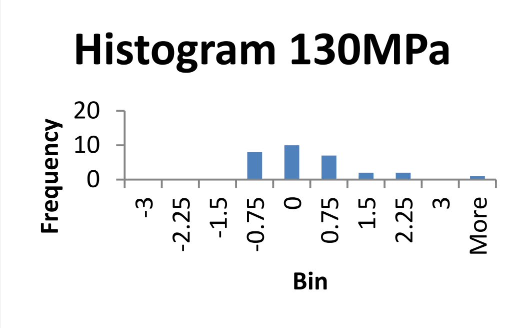
Histogram 130MPa
Frequency
20
10
0
-3
-2.25
-1.5
-0.75
0
0.75
1.5
2.25
3
More
Bin

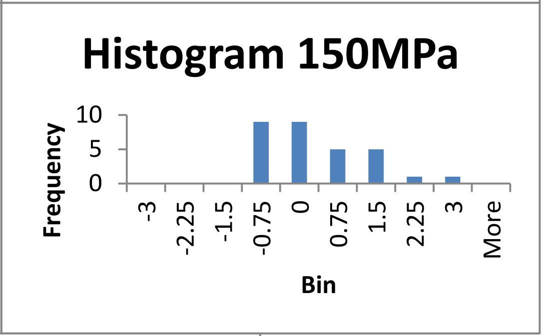
Histogram 150MPa
Frequency
10
5
0
-3
-2.25
-1.5
-0.75
0
0.75
1.5
2.25
3
More
Bin

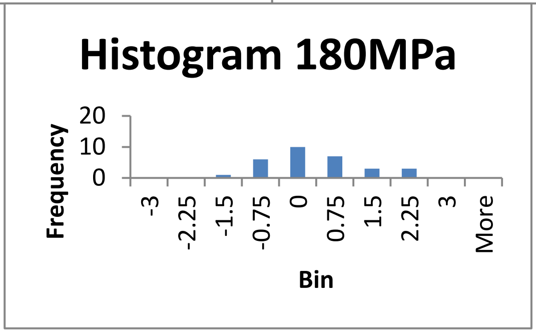
Histogram 180MPa
Frequency
20
10
0
-3
-2.25
-1.5
-0.75
0
0.75
1.5
2.25
3
More
Bin

Appendix Three: Roll-off Angle Data for 10 Second Compressed Disks

Pressure (MPa)	θ_{ro} 1st filing (Degrees)	θ_{ro} 2nd filing (Degrees)	θ_{ro} 3rd filing (Degrees)	θ_{ro} Average (Degrees)
40	4.0±0.7	4.2±1.0	4.7±0.9	4.3±0.4
45	4.9±0.8	3.9±0.6	4.0±0.8	4.3±0.4
51	4.2±0.6	4.3±0.8	5.7±0.6	4.8±0.4
56	3.9±0.8	4.4±0.6	4.3±0.6	4.2±0.3
65	3.9±1.0	4.9±1.3		4.4±0.8
73	5.1±0.8	4.2±0.6	5.0±0.8	4.8±0.4
86	5.6±1.1	5.4±1.1	5.1±1.2	5.4±0.6
100	7.2±1.7	9.4±3.3	8.3±0.9	8.3±1.2
120	10±1	9.4±2.0	11±3	10±1
130	11±2	12±2	12±2	12±1
160	17±3	14±3	22±5	17±2
190	22±6	23±4	27±8	24±3

Appendix Four: Wetting Data for Ecdysiastic Titanium Materials

Disk	θ_{ro} overall average (Degrees)	WCA average (Degrees)
1-dodecanethiol treated copper disk	3.8±0.3	159±2
1-dodecanethiol treated copper/titanium disk	3.8±0.9	157±1
HDFT treated copper disk	3.2±0.5	158±3
HDFT treated copper/titanium disk	3.4±0.5	159±3

Appendix Five: Histograms of z-scores for Mixed Titanium / Superhydrophobic Copper Disks